Converted waves in shallow marine environments: modelling and field experiments

Proefschrift

ter verkrijging van de graad van doctor
aan de Technische Universiteit Delft,
op gezag van de Rector Magnificus prof. ir. K.C.A.M. Luyben,
voorzitter van het College voor Promoties,
in het openbaar te verdedigen,
op donderdag 27 oktober om 10:00 uur

door

Nihed EL ALLOUCHE

doctorandus in de Aardwetenschappen
geboren te Eindhoven.

Dit proefschrift is goedgekeurd door de promotoren:
Prof. dr. ir. C.P.A. Wapenaar
Prof. dr. D.G. Simons

Copromotor:
Dr. Ir. G.G. Drijkoningen

Samenstelling promotiecommissie:

Rector Magnificus	Technische Universiteit Delft, voorzitter
Prof. dr. ir. C.P.A. Wapenaar	Technische Universiteit Delft, promotor
Prof. dr. D.G. Simons	Technische Universiteit Delft, promotor
Dr. ir. G.G. Drijkoningen	Technische Universiteit Delft, copromotor
Prof. dr. K. Holliger	Univeristé de Lausanne
Prof. dr. ir. J.T. Fokkema	Technische Universiteit Delft
Dr. E. Muyzert	Schlumberger Cambridge research center
Dr. P. Kruiver	Deltares
Prof. dr. ir. P.M. van den Berg	Technische Universiteit Delft, reservelid

This work is financially supported by "The Netherlands Research Centre of Integrated Solid Earth Science" (ISES).

ISBN-978-90-8891-334-1

Published by: Uitgeverij BOX Press, Oisterwijk
Printed by: Proefschriftmaken.nl
Cover designed by: Jürg Hunziker and Nihed El Allouche

Contents

Chapter 1
Introduction

The shallow marine subsurface is explored for various engineering purposes e.g. constructing platforms and wind farms, laying pipelines and dredging for sand. Knowledge of the soil properties is crucial to minimise the risks involved with these offshore activities. Energy resources in the form of gas hydrates and hydrocarbon reservoirs are often found a few hundred meters to a few kilometers below the seafloor. Accurate estimates of the soil properties at shallow depths may considerably improve the image at the target depth.

1.1 Importance of shear-wave information

The seismic method helps in solving geological and geotechnical problems by imaging and characterizing the shallow part of the earth. In this method, a wavefield is excited by a source and propagated into the subsurface. Discontinuities in seismic properties, related to layering and structures, reflect part of the wavefield back to the surface where it is recorded by receivers and processed to obtain the required image and rock properties.

The propagation of the wavefield is governed by the elastic wave equation which predicts the existence of two fundamentally different types of body waves: the compressional (P-) wave and the shear (S-) wave. The P-wave is polarized in the propagation direction and travels with a velocity (c_p) that is determined by the density of the medium (ρ), the compression modulus (K) and the shear modulus (μ), ($c_p = \sqrt{(K + (4/3)\mu)/\rho}$). The S-wave is polarized in the direction perpendicular to the propagation direction and travels with a speed (c_s) that is determined by the density and the shear modulus only ($c_s = \sqrt{\mu/\rho}$).

These fundamental differences between the P- and S-wave explain their appearances in recorded seismic data. Since the elastic constants are always positive, the P-waves propagate faster than the S-waves and hence arrive earlier in time. Depending mainly on the lithology and porosity the c_s/c_p ratio can range between 0.2 for unconsolidated sediments to 0.66 for sandstones (Sheriff & Geldart, 1995). The P-waves are dominant on the vertical component of the particle velocity and

are easily generated by explosive sources which favor their use in most seismic experiments.

However, the need for improvements in imaging and characterization of reservoirs has stimulated the interest of exploration geophysicists in obtaining S-wave information by acquiring multicomponent data (Stewart *et al.*, 2003). This type of seismic surveying became more standard over the last two decades. Problems such as imaging through shallow gas pockets (Granli *et al.*, 1999), lithology discrimination and predicting fluid content (Engelmark, 2001) were tackled by processing P to S converted waves. The insensitivity of S-waves to the gas and fluids in the pores and the analysis of c_s/c_p ratios provided additional information to solve these problems. Various lithological properties such as porosity and grain size are deduced from the c_s/c_p ratio through empirical relations (Domenico, 1984).

In high-resolution land seismics, surveying by means of shear waves proved to be successful in imaging the shallow subsurface. The development of the S-vibrator (Ghose *et al.*, 1996) enabled the excitation of horizontally polarized S-waves (SH) that are decoupled from the P-waves and hence easy to process. The low c_s values, generally encountered in these environments, resulted in short wavelengths resolving structures that were undetected by P-waves for the same bandwidths. This type of surveys finds many geotechnical applications because of the high sensitivity of c_s to the shear modulus and the strong correlation of the latter to soil properties that are of interest to civil engineering (Imai & Tonouchi, 1982; Ghose & Goudswaard, 2004). The acquisition of S-waves offers similar advantages for marine seismics.

1.2 Seismic properties of the shallow marine subsurface

Seismic parameters in the environment of interest can be measured in laboratories. The sound velocities of samples from the upper tens of centimeters of the seafloor are determined by a pulse technique (Hamilton & Bachman, 1982). These estimates are used subsequently to predict their in-situ values. These authors reported sediment P-wave velocity/water velocity ratios between 0.99 for silty clay and 1.2 for coarse sand sediment encountered in continental shelves. Researchers at Kiel University conducted deeper in-situ and core measurements of marine sediments mainly in the Barents Sea (Ayres & Theilen, 1999). They reported that c_s increased rapidly with depth whereas c_p remained nearly constant (Theilen & Pecher, 1991). The c_s values range between 10 and 40 m/s and they showed relatively strong correlation with density, porosity and water content. The P-wave velocities estimated from different cores varied between 1403 and 1685 m/s.

A more efficient technique for mapping properties of the shallow subsurface is based on acoustic remote sensing. In this technique, the scattering of a signal emitted by a tilted sonar is inverted to infer quantities such as acoustic velocity, density, grain size and attenuation factor. The obtained values are combined and used for lithological classification of the upper sediment layer (Simons *et al.*, 2007; Simons & Snellen, 2009). For greater depths, subsurface characterization relies on seismic methods.

1.3 Research motivation

Seismic surveys in marine environments are very efficient as source and receivers are commonly towed by a vessel. Figure 1.1 shows a typical marine configuration with an air-gun source generating a pressure field that is subsequently recorded by a hydrophone streamer. In contrast to land acquisition, large distances can be covered with this field set-up in a shorter amount of time. However, this configuration enables predominantly the recording of pure P-waves. Converted modes are hardly observed on streamer data because of the small conversion coefficient of the upgoing S-wave reflections at the water bottom. Densities as well as S-wave velocities can be retrieved by inverting the amplitude behavior of P-wave reflections as a function of offset. For unconsolidated sediments, this method failed to provide satisfactory results because of the large uncertainties associated with the c_s estimates (Riedel & Theilen, 2001). Consequently, retrieving S-wave information from the shallow marine subsurface requires a different approach.

For this purpose, various techniques can be adapted from land seismics, involving the acquisition of surface waves or horizontally polarized S-waves (SH). Many examples of the inversion of surface waves to obtain c_s profiles are described in the literature including the work of Ritzwoller & Levshin (2002) and Park *et al.* (2005) and more recently Kruiver *et al.* (2010) and Dong *et al.* (2010). Over the past years, major advances in the development of marine S-wave sources have been made since the work of Gehrmann *et al.* (1984). The first marine shear-wave vibrator prototype was presented by the Norwegian geotechnical institute in 2004 (Westerdahl *et al.*, 2004).

In this thesis, we aim at exploring the potentials of another type of waves generated by a P-wave source, namely the ones converted at the water bottom or a reflector to a vertically polarized S-mode (SV) and recorded at the water bottom. The main advantage provided by surveying with these waves instead of SH-waves is that c_p and c_s models can be constructed, which is essential for the characterization. The high efficiency of P-wave sources over the heavy SH-waves vibrators is another important advantage.

The use of converted waves require multicomponent recordings of the wavefield at the water bottom (Allouche *et al.*, 2008). The conventional acquisition method needs therefore to be adapted to optimally record PS-modes from shallow reflectors in shallow waters. Different modes of conversion are studied and their relevance to infer S-wave information is assessed. Finally, the separation of converted modes from P-waves, for the environment of study, is investigated.

1.4 Organization of the thesis

This thesis is composed of seven chapters. Three of these can be viewed as a stand-alone entities written in the form of a journal paper. A theoretical introduction, covering the basic equations, precedes these chapters. It includes a detailed derivation of the expressions describing the transmitted wavefield in a fluid-solid configuration. This part of the theory is relevant to understand the conversion from P to S at the water bottom. Also it lays the basis for Chapter 3, which deals with

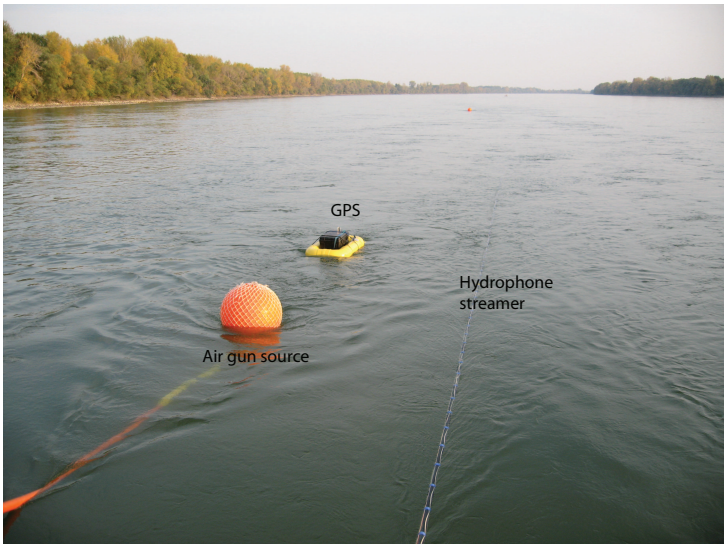

Figure 1.1: *Air gun towed to a buoy and a GPS receiver aligned with a hydrophone streamer.*

the excitation and the properties of a particular S-mode, referred to throughout this thesis as the non-geometric PS-wave (P*S).

The non-geometric PS-wave was first observed in a data set acquired in a shallow canal, using an air gun and multicomponent receivers placed on the water bottom. In Chapter 4, the data set is analyzed and the observations are validated by a modelling study. Based on the results of this data set, a new field experiment was planned and conducted in the Danube River in Hungary. The acquisition method adopted to record spatially dense multicomponent data is described in Chapter 5.

The acquired data is processed and the results are discussed in Chapter 6. The focus of the processing flow is placed on the separation of the converted waves from the P-waves. This is done by means of wavefield decomposition as well as using the Radon-transform technique.

Chapter 7 concludes the thesis, restating the main results concerning the conversion of P-waves in shallow water environments. An outlook on future applications and interests is also included.

Chapter 2
Theoretical background

2.1 Introduction

In this chapter, a brief review is given on the fundamental equations governing the wave propagation in acoustic and elastic media along with their corresponding solutions. These equations, discussed extensively in many textbooks (e.g. Aki & Richards, 2002; Brekhovskikh, 1960; Wapenaar & Berkhout, 1989), serve as a base to study the PS-conversion at a fluid-solid interface. In the first part of this chapter, the transmitted wavefield, generated by a source in the fluid, is derived using different analytical representations and methods such as the Sommerfeld integral and the Cagniard-de Hoop technique. The derived expressions are used in Chapter 3 to investigate the existence of a non-geometric PS-wave, excited when conversion occurs in the near-field. The evanescent character of this wave in the fluid is discussed here in much detail.

The second part of the theory deals with the decomposition of the wavefield into upgoing and downgoing P- and S-waves. This theory, based on the wave equation, was developed in many forms over the past decades (White, 1965; Dankbaar, 1985; Wapenaar & Berkhout, 1989) but was not often implemented in practice. This is because the decomposition schemes require the measurement of the velocity and traction components of the wavefield. For the special case of the ocean-bottom configuration, successful examples of modification and application of this method have been published (e.g. Amundsen & Reitan, 1995; Donati & Stewart, 1996; Schalkwijk *et al.*, 2003). In Chapter 6, the derived decomposition scheme is used to separate P-waves from PS-converted reflections for shallow water conditions.

2.2 Acoustic and elastic two-way wave equations

The two basic equations governing the propagation of waves in an acoustic medium are the linearized equation of motion (Fokkema & van den Berg, 1993)

$$\nabla P + \rho \partial_t \vec{v} = \vec{f}, \tag{2.1}$$

and the linearized deformation equation

$$\nabla.\vec{v} + \frac{1}{K}\partial_t P = Q, \tag{2.2}$$

where

P = acoustic pressure,
$\vec{v}$ = particle velocity,
ρ = volume density of mass,
$\vec{f}$ = volume density of force,
K = compression modulus and
Q = volume source density of injection rate.

The acoustic two-way wave equation for a homogeneous fluid is obtained by combining these two equations to

$$\nabla^2 P - \frac{\rho}{K}\partial_t^2 P = \nabla.\vec{f} - \rho\partial_t Q. \tag{2.3}$$

For the elastic case, the linearized equation of motion is (Wapenaar & Berkhout, 1989)

$$\rho\partial_t\vec{v} - \partial_j\vec{\tau}_j = \vec{f}, \tag{2.4}$$

and the deformation equation is

$$\partial_t\vec{\tau}_j - C_{jl}\partial_l\vec{v} = -\partial_t\vec{\sigma}_j, \tag{2.5}$$

where $\vec{\tau}_j$ is the traction vector in the direction j, $\vec{\sigma}_j$ is the traction vector associated with the source and C_{jl} is the stiffness subtensor with the coefficients c_{ijkl} (Woodhouse (1974) and Wapenaar & Berkhout (1989)). The Einstein summation convention is applied here. If we consider an isotropic medium, the stiffness coefficients can be reduced to the Lamé parameters λ and μ so that

$$c_{ijkl} = \lambda\delta_{ij}\delta_{kl} + \mu[\delta_{ik}\delta_{jl} + \delta_{il}\delta_{jk}], \tag{2.6}$$

where δ_{ij} is the Kronecker delta defined as

$$\delta_{ij} = \begin{cases} 0 & \text{if } i \neq j, \\ 1 & \text{if } i = j. \end{cases}$$

The coefficient μ is also known as the shear modulus. Assuming a homogeneous medium and combining the equation of motion and the equation of deformation, we obtain the following expression for the elastic wave equation

$$(\lambda + 2\mu)\nabla(\nabla.\vec{v}) - \mu\nabla\times\nabla\times\vec{v} - \rho\partial_t^2\vec{v} = -\partial_t(\vec{f} - \partial_j\vec{\sigma}_j). \tag{2.7}$$

2.3 Solutions to the two-way wave equation

In this section, the different solutions to the wave equation are presented. The plane wave solution for the source-free case is discussed first by following closely the work of Wapenaar & Berkhout (1989). A brief description of the properties of the homogeneous and inhomogeneous plane waves is included. The emphasis is placed on the latter because it determines the main characteristics of an arrival described further in the thesis in the context of a fluid-solid configuration. The general solution is subsequently extended to include the source term and is then referred to as the spherical wave solution.

2.3.1 Plane wave solutions

We consider a homogeneous acoustic space in a Cartesian coordinate system (x, y, z) with the z-axis pointing downward. For a source-free condition, the acoustic wave equation becomes

$$\nabla^2 P = \frac{1}{c^2}\partial_t^2 P, \tag{2.8}$$

where $c = \sqrt{K/\rho}$ denotes the propagation velocity. Eq. 2.8 is satisfied by a solution of the form

$$P(x, y, z, t) = P_0(t - p_x x - p_y y - qz), \tag{2.9}$$

where P_0 can be any twice differentiable function and, p_x, p_y and q are the components of the slowness vector $\vec{p}$ such that $c = 1/|\vec{p}|$. It follows that

$$p_x^2 + p_y^2 + q^2 = \frac{1}{c_x^2} + \frac{1}{c_y^2} + \frac{1}{c_z^2} = \frac{1}{c^2}, \tag{2.10}$$

where c_x, c_y and c_z are constants denoting the phase velocities along the x-, y- and z-direction. For a homogeneous propagating plane wave, it is generally known that $|c_x|$, $|c_y|$ or $|c_z|$ are higher than or equal to the propagation velocity c (Wapenaar & Berkhout, 1989). A plane wave is referred to as homogeneous when its amplitude is constant along the wavefront.

However, the plane wave is said to be inhomogeneous or evanescent when we consider for example the case that

$$\frac{1}{c_x^2} + \frac{1}{c_y^2} > \frac{1}{c^2}. \tag{2.11}$$

Consequently,

$$q^2 = \frac{1}{c^2} - p_x^2 - p_y^2 < 0, \tag{2.12}$$

implying that q, the vertical slowness, is imaginary. The wavefront propagates in the direction of $\vec{p}_0$ with the propagation velocity c_0 given by

$$c_0 = \frac{1}{|\vec{p}_0|} = \frac{1}{\sqrt{p_x^2 + p_y^2}}. \tag{2.13}$$

This means that the propagation velocity of the inhomogeneous plane wave is smaller than the homogeneous plane wave.

In homogeneous isotropic elastic media, the P-wave and the S-wave propagate independently. Therefore, the particle velocity is often separated in purely curl-free compressional waves ($\nabla \times \vec{v}^p = \vec{0}$) and divergence-free shear waves ($\nabla \cdot \vec{v}^s = 0$)

$$\vec{v} = \vec{v}^p + \vec{v}^s, \tag{2.14}$$

where

$$\begin{aligned} \vec{v}^p &= \nabla\phi, \\ \vec{v}^s &= \nabla \times \vec{\psi}, \end{aligned} \tag{2.15}$$

with ϕ being the P-wave potential and $\vec{\psi}$ being the S-wave potential vector. Substituting Eqs. 2.14 and 2.15 in the elastic two-way wave equation and omitting the source term, result in two independent wave equations for the P- and the S-wave

$$\nabla^2\phi = \frac{1}{c_p^2}\frac{\partial^2\phi}{\partial t^2}, \tag{2.16}$$

$$\nabla^2\vec{\psi} = \frac{1}{c_s^2}\frac{\partial^2\vec{\psi}}{\partial t^2}, \tag{2.17}$$

where $c_p = \sqrt{(\lambda + 2\mu)/\rho}$ and $c_s = \sqrt{\mu/\rho}$.

Similarly to the acoustic case, the particle motion in the elastic medium can be described in the following general form

$$\vec{v}^p(x, y, z, t) = \vec{v}_0^p A(t - p_x x - p_y y - q_p z), \tag{2.18}$$

$$\vec{v}^s(x, y, z, t) = \vec{v}_0^s A(t - p_x x - p_y y - q_s z), \tag{2.19}$$

where $\vec{v}_0^p$ and $\vec{v}_0^s$ are vectors denoting the polarization direction and A is a twice differentiable function. For the case of a homogeneous plane wave, we assume that the slownesses are all real and we write for the P- and S-wave respectively

$$\begin{aligned} \frac{1}{c_p^2} &= p_x^2 + p_y^2 + q_p^2, \\ \frac{1}{c_s^2} &= p_x^2 + p_y^2 + q_s^2. \end{aligned} \tag{2.20}$$

For real slownesses p_x and p_y such that

$$p_x^2 + p_y^2 > \frac{1}{c^2}, \tag{2.21}$$

it follows that

$$\begin{aligned} q_p^2 &= \frac{1}{c_p^2} - p_x^2 - p_y^2 < 0, \\ q_s^2 &= \frac{1}{c_s^2} - p_x^2 - p_y^2 < 0, \end{aligned} \tag{2.22}$$

implying that the vertical component of slowness associated with the P-wave, q_p, and with the S-wave, q_s, are imaginary. Consequently, the plane waves are inhomogeneous and propagate in the direction $\vec{p}_0$ with velocities given by

$$c_{p,0} = \frac{1}{|\vec{p}_0|} = \frac{1}{\sqrt{p_x^2 + p_y^2}},$$
$$c_{s,0} = \frac{1}{|\vec{p}_0|} = \frac{1}{\sqrt{p_x^2 + p_y^2}}. \tag{2.23}$$

It should be noted that for fixed p_x and p_y and for $p_x^2 + p_y^2 > 1/c_s^2 > 1/c_p^2$, the inhomogeneous plane P-waves and S-waves may propagate with the same velocity $c_{p,0} = c_{s,0}$.

The monochromatic homogeneous and inhomogeneous plane P-waves can be written in one expression, for a given angular frequency ω_0, by introducing the following complex notation (Wapenaar & Berkhout, 1989)

$$\vec{v}^{p\pm}(x, y, z, t) = Re[\hat{\vec{v}}^{p\pm}(x, y, z, t)], \tag{2.24}$$

with

$$\hat{\vec{v}}^{p\pm}(x, y, z, t) = \hat{\vec{v}}_0^{p\pm} e^{j\omega_0(t - p_x x - p_y y \mp q_p z)}, \tag{2.25}$$

where the P-wave vertical slowness q_p is defined as

$$q_p = +\sqrt{\frac{1}{c_p^2} - p_x^2 - p_y^2} \quad \text{for} \quad p_x^2 + p_y^2 \leq \frac{1}{c_p^2}, \tag{2.26}$$

$$q_p = -j\sqrt{p_x^2 + p_y^2 - \frac{1}{c_p^2}} \quad \text{for} \quad p_x^2 + p_y^2 > \frac{1}{c_p^2}, \tag{2.27}$$

and $\hat{\vec{v}}_0^{p\pm} = \hat{A}(p_x, p_y, \pm q_p)$ where $\hat{A}$ is a complex parameter. The signs are introduced to distinguish between plane waves propagating downward $(+)$ and others propagating upward $(-)$. The choice of the square root of the vertical slownesses ensures the decay of inhomogeneous waves in the z-direction satisfying the radiation condition.

Similarly for the monochromatic plane S-waves, we write

$$\vec{v}^{s\pm}(x, y, z, t) = Re[\hat{\vec{v}}_{s\pm}(x, y, z, t)], \tag{2.28}$$

with

$$\hat{\vec{v}}^{s\pm}(x, y, z, t) = \hat{\vec{v}}_0^{s\pm} e^{j\omega_0(t - p_x x - p_y y \mp q_s z)}, \tag{2.29}$$

where $\hat{\vec{v}}_0^{s\pm}$ denotes the complex amplitude factor. The S-wave vertical slowness, q_s, is defined as

$$q_s = +\sqrt{\frac{1}{c_s^2} - p_x^2 - p_y^2} \quad \text{for} \quad p_x^2 + p_y^2 \leq \frac{1}{c_s^2}, \tag{2.30}$$

$$q_s = -j\sqrt{p_x^2 + p_y^2 - \frac{1}{c_s^2}} \quad \text{for} \quad p_x^2 + p_y^2 > \frac{1}{c_s^2}. \tag{2.31}$$

2.3.2 Spherical wave solutions

In this section, we derive solutions to the acoustic wave equation for a monopole point source. The expressions are formulated in the wavenumber-frequency (k_x, k_y, z, ω) domain as well as in the space-time (x, y, z, t) domain. The latter can be interpreted as a superposition of homogeneous and inhomogeneous plane waves (Weyl integral) or as a summation of cylindrical waves (Sommerfeld integral). These integrals form the basis of the Reflectivity method (Fuchs & Müller, 1971; Kennett, 1980), often used in this thesis to model synthetic data. The solution to the elastic wave equation can be obtained along the same lines and is, therefore, not given explicitly in this section.

Writing the acoustic wave equation as follows

$$\nabla^2 P - \frac{1}{c^2}\partial_t^2 P = -\delta(\vec{R})S(t), \tag{2.32}$$

where we define the source term as a monopole point source of volume injection

$$\rho\partial_t Q(\vec{R}, t) = \delta(\vec{R})S(t), \tag{2.33}$$

with $S(t)$ indicating the source signature and where $\delta(\vec{R}) = \delta(x)\delta(y)\delta(z)$. The time domain solution to Eq. 2.32 is well-known and is of the form (Brekhovskikh (1960); Wapenaar & Berkhout (1989))

$$P(x, y, z, t) = \frac{1}{4\pi R}S(t - R/c), \tag{2.34}$$

where $R = \sqrt{x^2 + y^2 + z^2}$. This solution describes a spherical wave propagating with a speed c and with an amplitude term decreasing with increasing radius R.

Eq. 2.32 can also be solved in the (k_x, k_y, k_z, ω) domain. Applying a temporal and three-dimensional spatial Fourier transform, according to the sign convention indicated in Appendix A, yields a multiplication by $j\omega$ for the temporal derivative and a multiplication by $-jk_i$ for the spatial derivatives. The acoustic wave equation becomes

$$\left(\frac{\omega^2}{c^2} - k_x^2 - k_y^2 - k_z^2\right)\tilde{\tilde{P}} = -\hat{\tilde{S}}(\omega), \tag{2.35}$$

where $\hat{\tilde{S}}(\omega)$ is the source signal in the frequency domain. The solution is straightforward

$$\tilde{\tilde{P}}(k_x, k_y, k_z, \omega) = \frac{-\hat{\tilde{S}}(\omega)}{\frac{\omega^2}{c^2} - k_x^2 - k_y^2 - k_z^2}. \tag{2.36}$$

Applying the inverse Fourier transform with respect to k_z gives

$$\tilde{P}(k_x, k_y, z, \omega) = \frac{1}{2\pi}\int_{-\infty}^{\infty} \frac{-\hat{\tilde{S}}(\omega)}{\frac{\omega^2}{c^2} - k_x^2 - k_y^2 - k_z^2} e^{-jk_z z} dk_z. \tag{2.37}$$

As discussed by Aki & Richards (2002), this integral can be evaluated using Cauchy's residue theorem. The integration path is dependent on the z-value and is chosen to

ensure the suppression of the $e^{-jk_z z}$ term in Eq. 2.37 for $k_x^2 + k_y^2 > \omega^2/c^2$. Using the definition $k^2 = \omega^2/c^2$, the solution reads

$$\tilde{P}(k_x, k_y, z, \omega) = \frac{\hat{\tilde{S}}(\omega)}{2j\sqrt{k^2 - k_x^2 - k_y^2}} e^{-j\sqrt{k^2 - k_x^2 - k_y^2}|z|}. \tag{2.38}$$

The inverse Fourier transform of this solution to the (x, y, z, t) domain is equal to the monopole point source response given in Eq. 2.34. Writing the results again but in terms of slownesses instead of wavenumbers, using $\vec{k} = \omega\vec{p} = \omega(p_x, p_y, q)$, yields

$$\begin{aligned} P(x, y, z, t) &= \frac{1}{4\pi R} S(t - R/c) \\ &= \frac{1}{4\pi^3} \mathrm{Re} \int_0^\infty \omega \hat{\tilde{S}}(\omega) d\omega \iint_{-\infty}^{\infty} \frac{1}{2jq} e^{j\omega(t - p_x x - p_y y - q|z|)} dp_x dp_y, \end{aligned} \tag{2.39}$$

where $q = \sqrt{1/c^2 - p_x^2 - p_y^2}$ with $\mathrm{Im}(q) < 0$. Recalling Eq. 2.25, the solution to the source-free acoustic wave equation, it can be noticed that the above expression, known as the Weyl integral, can be interpreted as a superposition of monochromatic plane waves. Another form of this solution is obtained when we convert to cylindrical coordinates by substituting the following quantities

$$p_x = p_r \cos\phi \qquad p_y = p_r \sin\phi \qquad dp_x dp_y = p_r dp_r d\phi, \tag{2.40}$$

where ϕ is the azimuth and $p_r = \sqrt{p_x^2 + p_y^2}$ is the radial slowness. It follows that

$$P(x, y, z, t) = \frac{1}{4\pi^3} \mathrm{Re} \int_0^\infty \omega \hat{\tilde{S}}(\omega) d\omega \int_0^\infty \frac{p_r}{2jq} dp_r \int_0^{2\pi} e^{j\omega(t - p_r(x\cos\phi + y\sin\phi) - q|z|)} d\phi, \tag{2.41}$$

where $q = \sqrt{1/c^2 - p_r^2}$. The integral can be broken in two parts: $0 \leqslant p_r \leqslant 1/c$ and $p_r > 1/c$ giving

$$\begin{aligned} P(x, y, z, t) = &\frac{1}{4\pi^3} \mathrm{Re} \int_0^\infty \omega \hat{\tilde{S}}(\omega) d\omega \int_0^{1/c} \frac{p_r}{2jq} dp_r \int_0^{2\pi} e^{j\omega(t - p_r(x\cos\phi + y\sin\phi) - q|z|)} d\phi \\ &+ \frac{1}{4\pi^3} \mathrm{Re} \int_0^\infty \omega \hat{\tilde{S}}(\omega) d\omega \int_{1/c}^\infty \frac{p_r}{2|q|} dp_r \int_0^{2\pi} e^{j\omega(t - p_r(x\cos\phi + y\sin\phi) + j|q||z|)} d\phi, \end{aligned} \tag{2.42}$$

where $|q| = \sqrt{p_r^2 - 1/c^2}$ for $p_r > 1/c$. Expressing the slownesses p_r and q in terms of dip angle θ using $p_r = \sin\theta/c$ and $q = \cos\theta/c$ results for the first term of the right-hand side of Eq. 2.42 in (Tygel & Hubral, 1987)

$$\frac{1}{4\pi^3} \mathrm{Re} \int_0^\infty \frac{-j\omega \hat{\tilde{S}}(\omega)}{2c} d\omega \int_0^{\pi/2} \int_0^{2\pi} e^{j\omega(t - \frac{\sin\theta}{c}(x\cos\phi + y\sin\phi) - |z|\frac{\cos\theta}{c})} \sin\theta d\theta d\phi. \tag{2.43}$$

This expression can be interpreted as a superposition of homogeneous plane waves propagating with constant phase c and frequency ω with a constant amplitude factor $\omega\hat{\tilde{S}}(\omega)/2c$ in the direction of $\vec{p} = (1/c)(\sin\theta\cos\phi, \sin\theta\sin\phi, \cos\theta)$.

The second term of Eq. 2.42 can be interpreted as a superposition of inhomogeneous waves propagating only in the horizontal plane with a slowness direction $\vec{p} = (1/c)(\cos\phi, \sin\phi, 0)$ and with a phase velocity equal to $1/\sqrt{p_x^2 + p_y^2} < c$. As in section 2.3.1, these waves are classified as inhomogeneous waves because their amplitude is not constant along the wavefront but is decaying with a factor $\frac{\omega\hat{\tilde{S}}(\omega)p_r}{2|q|}e^{-|q||z|}$.

The representation in terms of inhomogeneous waves can also be expressed as a function of the tilt angle θ when we introduce the concept of "complex angle" (Brekhovskikh, 1960) such that $\theta = \pi/2 + j\alpha$ with $\alpha > 0$. This gives $p_x = \cosh\alpha\cos\phi/c$ and $p_y = \cosh\alpha\sin\phi/c$ and $q = j\sinh\alpha/c$. Due to these substitutions, the integrals given in Eq. 2.42 can be rewritten in a more general compact form

$$P(x,y,z,t) = \frac{1}{4\pi^3}\mathrm{Re}\int_0^\infty \frac{-j\omega\hat{\tilde{S}}(\omega)}{2c}d\omega \int_0^{\pi/2+j\alpha}\int_0^{2\pi} e^{j\omega(t-\frac{\sin\theta}{c}(x\cos\phi+y\sin\phi)-|z|\frac{\cos\theta}{c})}\sin\theta d\theta d\phi. \tag{2.44}$$

It should be noted that $q \to j\infty$ as $\alpha \to \infty$, implying that the inhomogeneous waves are indeed attenuated along the vertical direction in this expression.

The Sommerfeld integral is another concise formulation of the point source solution that is more widely used than the Weyl integral. This form is easily derived from Eq. 2.41 (Aki & Richards, 2002) by substituting the following variables

$$x = r\cos\phi' \qquad y = r\sin\phi', \tag{2.45}$$

where $r = \sqrt{x^2 + y^2}$, and with ϕ' being the azimuth angle. Using the trigonometric identity, $\cos(\phi - \phi') = \cos\phi\cos\phi' + \sin\phi\sin\phi'$, we write

$$P(x,y,z,t) = \frac{1}{4\pi^3}\mathrm{Re}\int_0^\infty \omega\hat{\tilde{S}}(\omega)d\omega \int_0^\infty \frac{p_r}{2jq}dp_r \int_0^{2\pi} e^{j\omega(t-p_r r\cos(\phi-\phi')-q|z|)}d\phi. \tag{2.46}$$

Finally, the Sommerfeld integral results from the evaluation of the integral over ϕ by means of the well-known representation of the zeroth-order Bessel function

$$\int_0^{2\pi} e^{j\omega p_r r\cos(\phi-\phi')}d\phi = 2\pi J_0(\omega p_r r). \tag{2.47}$$

It follows that

$$P(x,y,z,t) = \frac{1}{2\pi^2}\mathrm{Re}\int_0^\infty \omega\hat{\tilde{S}}(\omega)d\omega \int_0^\infty \frac{p_r}{2jq}J_0(\omega p_r r)e^{j\omega(t-q|z|)}dp_r. \tag{2.48}$$

This integral, known as the Sommerfeld integral, uses cylindrical or conical waves as a basis. Summing these waves gives the solution for a point source (Aki & Richards, 2002).

2.4 Energy partitioning of plane waves at a fluid-solid interface

The general expressions derived above are used in the remaining of this chapter to solve the wave equation for a configuration relevant to the environment of interest. From this section onward, the focus is placed on the physics involved with the propagation of waves at a fluid-solid interface. We start by investigating the interaction of an incident pressure plane wave with this type of interface. For this purpose, we consider a fluid halfspace with sound speed c_f and density ρ_f overlying a homogeneous isotropic elastic halfspace with P-wave velocity c_p, S-wave velocity c_s and density ρ_s described by a Cartesian coordinate system (x, y, z) with the z-axis pointing downward (see figure 2.1).

The energy partitioning of plane waves at a fluid-solid interface is constrained by three boundary conditions (de Hoop & van der Hijden, 1983):

1. Continuity of vertical components of particle velocity

$$\lim_{z\downarrow 0}(v_z^p + v_z^s) = \lim_{z\uparrow 0}(v_z^i + v_z^r), \tag{2.49}$$

   where v_z^p and v_z^s are the vertical components of particle velocity associated with the P- and the S-wave in the solid, respectively, and v_z^i and v_z^r are the vertical components of particle velocity of the incident wave and the reflected wave in the fluid, respectively.

2. The opposite of pressure in the fluid equals the vertical component of traction in the solid

$$\lim_{z\downarrow 0}(\tau_{z,z}^p + \tau_{z,z}^s) = \lim_{z\uparrow 0}(-P^i - P^r), \tag{2.50}$$

   where $\tau_{z,z}^p$ and $\tau_{z,z}^s$ are the traction components in the vertical direction due to the P- and S-wave, respectively and P^i and P^r are the pressure fields due to the incident wave and the reflected wave.

3. Vanishing of tangential components of traction in the solid

$$\begin{aligned} \lim_{z\downarrow 0}(\tau_{x,z}^p + \tau_{x,z}^s) &= 0, \\ \lim_{z\downarrow 0}(\tau_{y,z}^p + \tau_{y,z}^s) &= 0, \end{aligned} \tag{2.51}$$

   where $\tau_{x,z}^p$, $\tau_{x,z}^s$, $\tau_{y,z}^p$ and $\tau_{y,z}^s$ are the tangential traction components of the P- and S-wave in the solid.

We choose to quantify the energy partitioning of the incident wave, due to the interaction with the interface, in terms of particle velocity ratios. Using the plane wave solution derived in section 2.3.1 and the complex notation introduced in Eq. 2.24, we write for the vertical component of the incident wave $\hat{v}_z^i$, with amplitude $\hat{v}_0^i$, and the reflected wave $\hat{v}_z^r$, with amplitude $\hat{v}_0^r$

$$\hat{v}_z^i(x, y, z, t) = q_f \hat{v}_0^i e^{j\omega(t - p_x x - p_y y - q_f z)}, \tag{2.52}$$

$$\hat{v}_z^r(x, y, z, t) = -q_f \hat{v}_0^r e^{j\omega(t - p_x x - p_y y + q_f z)}, \tag{2.53}$$

where p_x and p_y are the horizontal slownesses and q_f is the vertical slowness defined as $q_f = \sqrt{1/c_f^2 - p_x^2 - p_y^2}$.

The vertical component of the particle velocity can be related to the pressure field using the source-free linearized equation of motion (Eq. 2.1). For the pressure field, we find

$$\hat{P}^i(x,y,z,t) = \rho_f \hat{v}_0^i e^{j\omega(t-p_x x - p_y y - q_f z)}, \tag{2.54}$$
$$\hat{P}^r(x,y,z,t) = \rho_f \hat{v}_0^r e^{j\omega(t-p_x x - p_y y + q_f z)}. \tag{2.55}$$

At the fluid-solid interface, the incident pressure field is transmitted to a P-wave and converted to an S-wave. The particle velocity in the solid, associated with the P-wave, $\vec{v}^p$, is decomposed in horizontal and vertical components

$$\hat{\vec{v}}^p(x,y,z,t) = \{\hat{v}_x^p, \hat{v}_y^p, \hat{v}_z^p\} = \{p_x, p_y, q_p\}\hat{v}_0^p e^{j\omega(t-p_x x - p_y y - q_p z)}, \tag{2.56}$$

with $q_p = \sqrt{1/c_p^2 - p_x^2 - p_y^2}$. Similarly, the particle velocity due to the S-wave, $\vec{v}^s$, is decomposed as follows

$$\hat{\vec{v}}^s(x,y,z,t) = \{\hat{v}_x^s, \hat{v}_y^s, \hat{v}_z^s\} = \{q_s\hat{v}_{0,x}^s, q_s\hat{v}_{0,y}^s, -p_x\hat{v}_{0,x}^s - p_y\hat{v}_{0,y}^s\}e^{j\omega(t-p_x x - p_y y - q_s z)}. \tag{2.57}$$

where $q_s = \sqrt{1/c_s^2 - p_x^2 - p_y^2}$. Given this, we can now derive the expressions associated with the tractions using the deformation equation for elastic media (see Eq. 2.5). The traction vector, $\vec{\tau}_z = (\tau_{x,z}, \tau_{y,z}, \tau_{z,z})$, is related to the particle velocity according to $\partial_t \vec{\tau}_z = (\mu(\partial_z v_x + \partial_x v_z), \mu(\partial_z v_y + \partial_y v_z), \lambda(\partial_x v_x + \partial_z v_z) + 2\mu\partial_z v_z)$. The vertical components of traction associated with the P-wave are

$$\begin{aligned}
\hat{\tau}_{x,z}^p(x,y,z,t) &= -2\rho_s c_s^2 p_x q_p \hat{v}_0^p e^{j\omega(t-p_x x - p_y y - q_p z)}, \\
\hat{\tau}_{y,z}^p(x,y,z,t) &= -2\rho_s c_s^2 p_y q_p \hat{v}_0^p e^{j\omega(t-p_x x - p_y y - q_p z)}, \\
\hat{\tau}_{z,z}^p(x,y,z,t) &= \rho_s[2c_s^2(p_x^2 + p_y^2) - 1]\hat{v}_0^p e^{j\omega(t-p_x x - p_y y - q_p z)},
\end{aligned} \tag{2.58}$$

and with the S-wave

$$\begin{aligned}
\hat{\tau}_{x,z}^s(x,y,z,t) &= \rho_s c_s^2[(p_x^2 - q_s^2)\hat{v}_{0,x}^s + p_y p_x \hat{v}_{0,y}^s]e^{j\omega(t-px - p_y y - q_s z)}, \\
\hat{\tau}_{y,z}^s(x,y,z,t) &= \rho_s c_s^2[(p_y^2 - q_s^2)\hat{v}_{0,y}^s + p_y p_x \hat{v}_{0,x}^s]e^{j\omega(t-px - p_y y - q_s z)}, \\
\hat{\tau}_{z,z}^s(x,y,z,t) &= 2\rho_s c_s^2 q_s[p_x \hat{v}_{0,x}^s + p_y \hat{v}_{0,y}^s]e^{j\omega(t-px - p_y y - q_s z)}.
\end{aligned} \tag{2.59}$$

To obtain the reflection, transmission and conversion coefficients in terms of particle velocity ratios, the amplitude factors are normalized by the particle velocity amplitude of the incident pressure field $\hat{v}_0^i$. The reflection coefficient is defined as $R_p = \hat{v}_0^r/\hat{v}_0^i$, the transmission coefficient as $T_p = \hat{v}_0^p/\hat{v}_0^i$ and the transmission conversion coefficients as $T_{x,s} = \hat{v}_{0,x}^s/\hat{v}_0^i$ and $T_{y,s} = \hat{v}_{0,y}^s/\hat{v}_0^i$. Substituting Eqs. 2.51 from the third boundary condition results in $p_y T_{x,s} = p_x T_{y,s}$ and hence

$$\begin{aligned}
T_{x,s} &= p_x T_s \\
T_{y,s} &= p_y T_s,
\end{aligned} \tag{2.60}$$

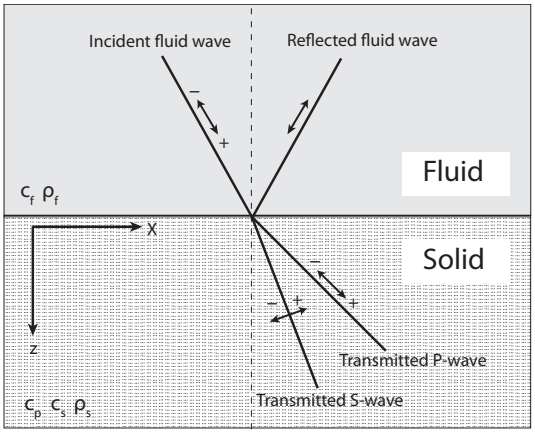

Figure 2.1: *Waves generated at a fluid-solid interface due to incident fluid wave. Displacement polarities are indicated by black arrows.*

where

$$T_s = \frac{-q_p}{(1/2c_s^2 - p_x^2 - p_y^2)} T_p. \tag{2.61}$$

The reflection and transmission coefficients T_p and R_p can be obtained from the remaining boundary conditions. The terms are rearranged and written in a similar form as de Hoop & van der Hijden (1984). It follows that

$$T_p = \frac{\rho_f (1/2c_s^2 - p_x^2 - p_y^2)}{\rho_s c_s^2 \Delta_{SCH}}, \tag{2.62}$$

$$R_p = \frac{-\rho_f q_p / 4c_s^4 \rho_s q_f + \Delta_R}{\Delta_{SCH}}, \tag{2.63}$$

where

$$\Delta_R = (p_x^2 + p_y^2 - 1/2c_s^2)^2 + (p_x^2 + p_y^2) q_p q_s, \tag{2.64}$$

is the "Rayleigh wave denominator", the term associated with the surface wave at a stress-free surface, and

$$\Delta_{SCH} = \rho_f q_p / 4c_s^4 \rho_s q_f + \Delta_R, \tag{2.65}$$

is the "Scholte wave denominator", the term associated with the surface wave along a fluid-solid interface.

2.5 Transmitted wavefield at a fluid-solid interface

Given a point source located in the fluid, at a height z_s from the interface, an analytical solution to the transmitted wavefield in the solid can be found. As explained in section 2.3.2, the solution to a point source in unbounded media is a spherical wave which can be described as a superposition of plane waves (Weyl

integral) or cylindrical waves (Sommerfeld integral). In a similar manner, we derive, in this section, the transmission response in the solid due to an incident spherical fluid wave, by means of these two representations.

2.5.1 In terms of the Weyl integral

In the solid, the particle velocity is governed by the elastic wave equation given by Eq. 2.7 and is a sum of P- and S-wave contributions

$$\vec{v}(x,y,z,t) = \vec{v}^p(x,y,z,t) + \vec{v}^s(x,y,z,t). \tag{2.66}$$

These contributions can be expressed as a plane-wave summation using Eq. 2.39. We find

$$\begin{aligned} v_x(x,y,z,t) = \frac{1}{4\pi^3}\mathrm{Re}\int_0^\infty \omega\hat{\tilde{S}}(\omega)d\omega \iint_{-\infty}^{\infty} \frac{1}{2jq_f}[A_x^p e^{j\omega(t-p_x x-p_y y-q_p z+q_f z_s)} \\ +A_x^s e^{j\omega(t-p_x x-p_y y-q_s z+q_f z_s)}]dp_x dp_y, \end{aligned} \tag{2.67}$$

$$\begin{aligned} v_y(x,y,z,t) = \frac{1}{4\pi^3}\mathrm{Re}\int_0^\infty \omega\hat{\tilde{S}}(\omega)d\omega \iint_{-\infty}^{\infty} \frac{1}{2jq_f}[A_y^p e^{j\omega(t-p_x x-p_y y-q_p z+q_f z_s)} \\ +A_y^s e^{j\omega(t-p_x x-p_y y-q_s z+q_f z_s)}]dp_x dp_y, \end{aligned} \tag{2.68}$$

$$\begin{aligned} v_z(x,y,z,t) = \frac{1}{4\pi^3}\mathrm{Re}\int_0^\infty \omega\hat{\tilde{S}}(\omega)d\omega \iint_{-\infty}^{\infty} \frac{1}{2jq_f}[A_z^p e^{j\omega(t-p_x x-p_y y-q_p z+q_f z_s)} \\ +A_z^s e^{j\omega(t-p_x x-p_y y-q_s z+q_f z_s)}]dp_x dp_y, \end{aligned} \tag{2.69}$$

where the amplitude factors A_x^p, A_x^s, A_y^p, A_y^s, A_z^p and A_z^s are determined by relating them, through the transmission coefficients T_p and T_s (see Eqs. 2.61 and 2.62), to the amplitude of the incident wavefield. We find that

$$\begin{aligned} A_x^p = \frac{p_x}{\rho_f}T_p, \qquad A_x^s = \frac{p_x q_s}{\rho_f}T_s, \\ A_y^p = \frac{p_y}{\rho_f}T_p, \qquad A_y^s = \frac{p_y q_s}{\rho_f}T_s, \\ A_z^p = \frac{q_p}{\rho_f}T_p, \qquad A_z^s = \frac{-(p_x^2+p_y^2)}{\rho_f}T_s. \end{aligned} \tag{2.70}$$

The transmitted wavefield can be computed using the expressions derived above by integrating along the horizontal slownesses. However, due to singularities associated with the slowness components, attenuation is usually introduced to enable the computation of these integrals (Aki & Richards, 2002). An alternative approach would be to use complex frequencies (Chapman, 2004).

2.5.2 In terms of the Sommerfeld integral

Formulating the transmitted wavefield as a superposition of cylindrical waves is achieved by converting the expressions, found for the particle velocity in the previous

section, from Cartesian (x, y, z) to cylindrical (r, ϕ', z) coordinate system according to

$$\begin{aligned} v_r &= v_x \cos\phi' + v_y \sin\phi', \\ v_{\phi'} &= -v_x \sin\phi' + v_y \cos\phi', \\ v_z &= v_z. \end{aligned} \tag{2.71}$$

The results follow by making the same substitutions as in section 2.3.2, (see Eqs. 2.40, 2.45 and 2.47) and using the Bessel identity $d/dx[x^m J_m(x)] = x^m J_{m-1}$. The components of particle velocity in the solid become then

$$\begin{aligned} v_r(r,\phi',z,t) = \frac{1}{4\pi^2}\mathrm{Re}\int_0^\infty \frac{-\omega\hat{\tilde{S}}(\omega)}{\rho_f c_f}\int_0^{2\pi}\frac{p^2}{q_f}J_1(\omega p r)\Big[c_p T_p e^{j\omega(t-q_p z+q_f z_s)} \\ +q_s c_s T_s e^{j\omega(t-q_s z+q_f z_s)}\Big]\,dp d\omega, \end{aligned} \tag{2.72}$$

$$v_{\phi'}(r,\phi',z,t) = 0,$$

$$\begin{aligned} v_z(r,\phi',z,t) = \frac{1}{4\pi^2}\mathrm{Re}\int_0^\infty \frac{\omega\hat{\tilde{S}}(\omega)}{\rho_f c_f}\int_0^{2\pi}\frac{p}{jq_f}J_0(\omega p r)\Big[q_p c_p T_p e^{j\omega(t-q_p z+q_f z_s)} \\ -p^2 c_s T_s e^{j\omega(t-q_s z+q_f z_s)}\Big]\,dp d\omega. \end{aligned} \tag{2.73}$$

In a cylindrical coordinate system, the P-wave and the converted SV-wave are polarized in the (r, z) plane. Consequently, the azimuthal component of the particle velocity, $v_{\phi'}$, vanishes.

2.6 Solution of the transmitted wavefield using the Cagniard-de Hoop method

With the Cagniard-de Hoop method, an explicit solution for the transmission response can be found in the (x, y, z, t) domain without actually having to perform any inverse transform (de Hoop, 1960). This method, widely discussed in the literature, aims at modifying the integral into a form that can be identified as the impulse response in the time domain. The Cagniard-de Hoop technique is developed in the slowness-Laplace domain using the one-sided Laplace transform with respect to time

$$\widehat{v}(x,y,z,s) = \int_0^\infty v(x,y,z,t)e^{-st}dt, \tag{2.74}$$

with real positive transform parameter s, and a two-dimensional Fourier transform with respect to the x and y coordinates

$$\breve{v}(\alpha,\beta,z,s) = \iint_{-\infty}^{\infty}\widehat{v}(x,y,z,s)e^{js(\alpha x+\beta y)}dxdy, \tag{2.75}$$

$$\widehat{v}(x,y,z,s) = \Big(\frac{s}{2\pi}\Big)^2\iint_{-\infty}^{\infty}\breve{v}(\alpha,\beta,z,s)e^{-js(\alpha x+\beta y)}d\alpha d\beta, \tag{2.76}$$

where $s\alpha$ and $s\beta$ are the transform parameters. Applying these transforms to the inhomogeneous acoustic wave equation gives

$$\partial_z^2 \breve{P} - s^2 \bar{q}_f \breve{P} = -s\rho_f \widehat{Q}\delta(z), \tag{2.77}$$

where $\bar{q}_f = \sqrt{1/c_f^2 + \alpha^2 + \beta^2}$ with $\mathrm{Re}(\bar{q}_f) \geq 0$, chosen such that the radiation condition is satisfied. The solution for the incident pressure wavefield reads

$$\breve{P}^i(\alpha, \beta, z, s) = \frac{\rho_f}{2\bar{q}_f} \widehat{Q} e^{-s\bar{q}_f |z - z_s|}. \tag{2.78}$$

The vertical component of particle velocity follows from the equation of motion

$$\breve{v}_z^i(\alpha, \beta, z, s) = \frac{\widehat{Q}}{2} e^{-s\bar{q}_f |z - z_s|}. \tag{2.79}$$

In the solid, the components of particle velocity associated with the transmitted P-wave are obtained by requiring the motion to be rotation-free. Expressing the amplitude of this wave in terms of the transmission coefficient T_p given in Eq. 2.62, results in

$$\breve{v}^p(\alpha, \beta, z, s) = \{j\alpha, j\beta, \bar{q}_p\} T_p \frac{\widehat{Q}}{2\bar{q}_f} e^{-s(\bar{q}_p z - \bar{q}_f z_s)}, \tag{2.80}$$

where $\bar{q}_p = \sqrt{1/c_p^2 + \alpha^2 + \beta^2}$ with $\mathrm{Re}(\bar{q}_p) \geq 0$.

Similarly, we obtain for the converted S-wave

$$\breve{v}^s(\alpha, \beta, z, s) = \{j\alpha\bar{q}_s, j\beta\bar{q}_s, -\alpha^2 - \beta^2\} T_s \frac{\widehat{Q}}{2\bar{q}_f} e^{-s(\bar{q}_s z - \bar{q}_f z_s)}, \tag{2.81}$$

where $\bar{q}_s = \sqrt{1/c_s^2 + \alpha^2 + \beta^2}$ with $\mathrm{Re}(\bar{q}_s) \geq 0$.

2.6.1 Space-time domain expressions for a line source

The following step is to transform the expressions found above to the space-time domain using the inverse transform given in Eq. 2.76. First, we discuss the solution to a line source by imposing $\beta = 0$ and substituting $\bar{p} = j\alpha$. Furthermore, the source term $s\widehat{Q}$ is omitted here, only to be convolved later with the identified impulse response. The inverse Fourier transforms to be modified are then

$$\{\widehat{G}_x^p(x, z, s), \widehat{G}_z^p(x, z, s)\} = \frac{s}{4\pi j} \int_{-j\infty}^{j\infty} \{\bar{p}, \bar{q}_p\} \frac{T_p}{s\bar{q}_f} e^{-s(\bar{p}x + \bar{q}_p z - \bar{q}_f z_s)} d\bar{p}, \tag{2.82}$$

for the Green's function due to the P-wave and

$$\{\widehat{G}_x^s(x, z, s), \widehat{G}_z^s(x, z, s)\} = \frac{s}{4\pi j} \int_{-j\infty}^{j\infty} \{\bar{q}_s, \bar{p}\} \frac{\bar{p} T_s}{s\bar{q}_f} e^{-s(\bar{p}x + \bar{q}_s z - \bar{q}_f z_s)} d\bar{p}, \tag{2.83}$$

for the Green's function due to the S-wave.

The time-domain expressions are obtained by transforming the integration along the imaginary $\bar{p}$-axis into the following real integration (de Hoop & van der Hijden, 1983)

$$\widehat{G}(x,z,s) = \int_0^T e^{-s\tau} \Gamma(x,z,\tau) d\tau, \tag{2.84}$$

where Γ is the part of the integrand with no dependence on s and T is the traveltime of the transmitted wave. With this modification, the integral is forced to take the form of the forward Laplace transform in Eq. 2.74 from which the explicit-expression in the (x,y,t) domain can be deduced. The modified Cagniard path can be found by requiring

$$\begin{aligned} \mathrm{Re}(\bar{p}x + \bar{q}_p z - \bar{q}_f z_s) &= \tau, \\ \mathrm{Im}(\bar{p}x + \bar{q}_p z - \bar{q}_f z_s) &= 0. \end{aligned} \tag{2.85}$$

Solving these equations, enables us to know how to parameterize the integration path as a function of real values of τ. In this configuration, where source and receivers are located in different media, four square-roots are obtained; but only the two complex valued contribute to the final response. Figure 2.2(a) shows the path C given by $\bar{p} = \bar{p}_s(\tau)$. Using the Cauchy's residue theory, the integrals, given in Eqs. 2.82 and 2.83 can be rewritten in terms of the path C and two large arcs C_1 and C_2 indicated in figure 2.2(a). According to Jordan's lemma (Aki & Richards, 2002), the contribution from these integrands is zero as their radius tends to ∞. If there are no singularities enclosed between the $\bar{p}$-axis and the path C, Schwarz's reflection principle can be applied and the transforms can then be simplified to the form

$$\{\widehat{G}^p_x(x,z,s), \widehat{G}^p_x(x,z,s)\} = \frac{1}{2\pi}\mathrm{Im}\int_{t_p}^{\infty} \{\bar{p}, \bar{q}_p\} \frac{T_p}{\bar{q}_f} \frac{\partial \bar{p}}{\partial \tau} e^{-s\tau} d\tau, \tag{2.86}$$

$$\{\widehat{G}^s_x(x,z,s), \widehat{G}^s_x(x,z,s)\} = \frac{1}{2\pi}\mathrm{Im}\int_{t_s}^{\infty} \{\bar{q}_s, \bar{p}\} \frac{\bar{p} T_s}{\bar{q}_f} \frac{\partial \bar{p}}{\partial \tau} e^{-s\tau} d\tau, \tag{2.87}$$

where t_p and t_s are the arrival times of the P- and S-wave, respectively.

From these expressions, we can finally identify the impulse response of the transmitted P-wave

$$\{G^p_x(x,z,\tau), G^p_z(x,z,\tau)\} = \begin{cases} 0 & \text{for } -\infty < \tau < t_p, \\ \frac{1}{2\pi}\mathrm{Im}\left[\{\bar{p}, \bar{q}_p\} \frac{T_p}{\bar{q}_f} \frac{\partial \bar{p}}{\partial \tau}\right]_{\bar{p}=\bar{p}_p(\tau)} & \text{for } t_p < \tau < \infty, \end{cases} \tag{2.88}$$

where

$$\frac{\partial \tau}{\partial \bar{p}} = x - \frac{\bar{p}}{\bar{q}_p} z + \frac{\bar{p}}{\bar{q}_f} z_s. \tag{2.89}$$

It is difficult to find an explicit expression for the mapping function $\bar{p}_p(\tau)$, therefore, Eq. 2.88 needs to be numerically evaluated at each time step.

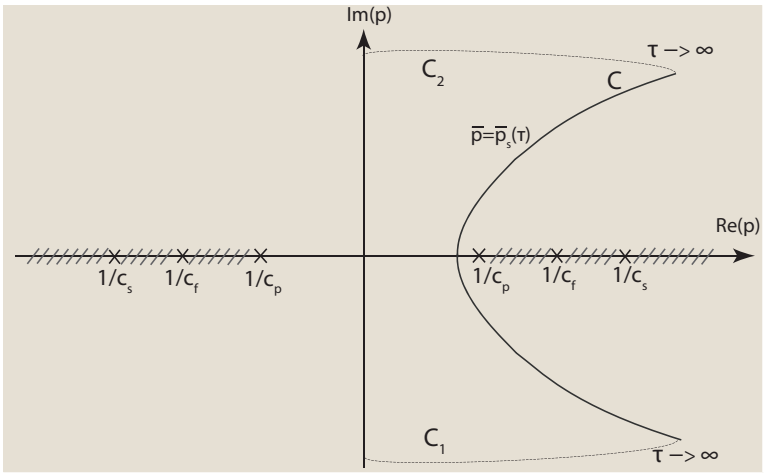

(a)

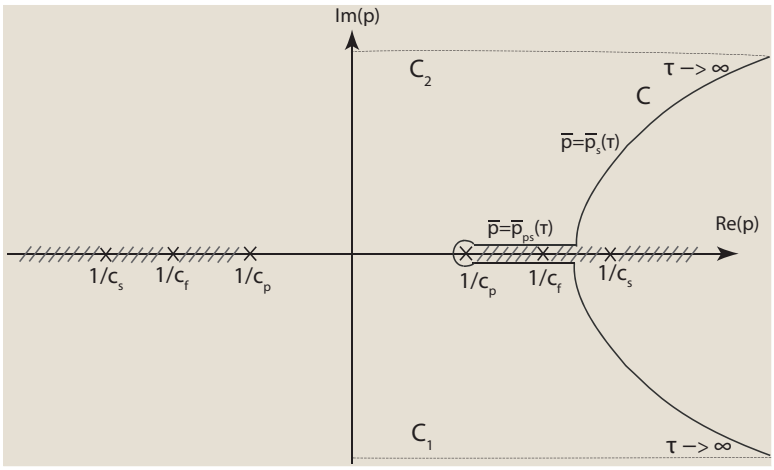

(b)

Figure 2.2: *The modified integration path and the singularities* $1/c_p$,$1/c_f$ *and* $1/c_s$ *plotted on the* $\bar{p}$*-plane.*

Similarly, for the S-wave we write

$$\{G^s_x(x,z,\tau), G^s_z(x,z,\tau)\} = \begin{cases} 0 & \text{for } -\infty < \tau < t_s, \\ \frac{1}{2\pi}\mathrm{Im}\left[\{\bar{q}_s,\bar{p}\}\frac{T_s}{\bar{q}_f}\bar{p}\frac{\partial\bar{p}}{\partial\tau}\right]_{\bar{p}=\bar{p}_s(\tau)} & \text{for } t_s < \tau < \infty. \end{cases} \tag{2.90}$$

This solution is only valid when the converted S-wave is the first arrival; however, this is not always the case. For a solid, with $c_s < c_f < c_p$, two head waves associated with the branch points $1/c_p$ and $1/c_f$ can introduce singularities that contribute to

the impulse response if they precede the converted wave. To account for this, the Cagniard path can be extended by a loop around the (smallest) branch point $1/c_p$ as shown in figure 2.2(b). The path C, contributing to the solution, consists here of the parts: $\bar{p}_s(\tau)$, $\bar{p}_{ps} + j\delta$ and $\bar{p}_{ps} - j\delta$ with $\delta \downarrow 0$. Finally, we obtain

$$\{G^s_x(x,z,\tau), G^s_z(x,z,\tau)\} = \begin{cases} 0 \text{ for } -\infty < \tau < t_{ps} \\ \frac{1}{2\pi}\mathrm{Im}\left[\{\bar{q}_s, \bar{p}\}\frac{T_s}{\bar{q}_f}\bar{p}\frac{\partial \bar{p}}{\partial \tau}\right]_{\bar{p}=\bar{p}_{ps}(\tau)} \text{ for } t_{ps} < \tau < t_s, \\ \frac{1}{2\pi}\mathrm{Im}\left[\{\bar{q}_s, \bar{p}\}\frac{T_s}{\bar{q}_f}\bar{p}\frac{\partial \bar{p}}{\partial \tau}\right]_{\bar{p}=\bar{p}_s(\tau)} \text{ for } t_s < \tau < \infty, \end{cases} \tag{2.91}$$

and where

$$t_{ps} = \frac{x}{c_p} + \sqrt{\frac{1}{c_s^2} - \frac{1}{c_p^2}}z - \sqrt{\frac{1}{c_f^2} - \frac{1}{c_p^2}}z_s, \tag{2.92}$$

is the arrival time of the PS-head-wave.

2.6.2 Space-time domain expressions for a point source

Explicit space-time domain expressions can also be derived for a point source using the Cagniard-de Hoop method (de Hoop & van der Hijden, 1984). Starting from Eqs. 2.80 and 2.81 and omitting the source term $s^2\widehat{Q}$, we write

$$\begin{aligned} &\{\widehat{G}^p_x(x,y,z,s), \widehat{G}^p_y(x,y,z,s), \widehat{G}^p_z(x,y,z,s)\} \\ &\qquad = \left(\frac{s}{2\pi}\right)^2 \iint_{-\infty}^{\infty} \{j\alpha, j\beta, \bar{q}_p\}\frac{T_p}{s^2} e^{-s(j\alpha x + j\beta y + \bar{q}_p z - \bar{q}_f z_s)} d\alpha d\beta, \end{aligned} \tag{2.93}$$

for the Green's function due to the P-wave and

$$\begin{aligned} &\{\widehat{G}^p_x(x,y,z,s), \widehat{G}^p_y(x,y,z,s), \widehat{G}^p_z(x,y,z,s)\} \\ &\qquad = \left(\frac{s}{2\pi}\right)^2 \iint_{-\infty}^{\infty} \{j\alpha\bar{q}_s, j\alpha\bar{q}_s, -\alpha^2 - \beta^2\}\frac{T_s}{s^2} e^{-s(j\alpha x + j\beta y + \bar{q}_s z - \bar{q}_f z_s)} d\alpha d\beta, \end{aligned} \tag{2.94}$$

for the Green's function due to the S-wave. The modification step is achieved by the following substitutions

$$\alpha = \kappa\cos\theta - \gamma\sin\theta, \qquad \beta = \kappa\sin\theta + \gamma\cos\theta,$$

where θ follows from the polar coordinate specification of the point of observation

$$x = r\cos\theta, \qquad y = r\sin\theta. \tag{2.95}$$

Consequently, $d\alpha d\beta = d\kappa d\gamma$. Changing the order of integrals and substituting $\bar{p}_r = j\kappa$ results in

$$\begin{aligned}
&\{\widehat{G}_x^p(x,y,z,s), \widehat{G}_y^p(x,y,z,s), \widehat{G}_z^p(x,y,z,s)\} \\
&\qquad = \frac{1}{4\pi^2}\int_{-\infty}^{\infty} -jd\gamma \int_{-j\infty}^{j\infty} \{C_x^p, C_y^p, C_z^p\} e^{-s(\bar{p}_r r + \bar{q}_p z - \bar{q}_f z_s)} d\bar{p}_r, \\
&\qquad = \frac{1}{2\pi^2}\int_{t_p(0)}^{\infty} e^{-s\tau} d\tau \int_0^{\gamma_p(\tau)} \mathrm{Im}\left[\{C_x^p, C_y^p, C_z^p\} \frac{1}{\partial\tau/\partial\bar{p}_r}\right] d\gamma, \\
&\{\widehat{G}_x^p(x,y,z,s), \widehat{G}_y^p(x,y,z,s), \widehat{G}_z^p(x,y,z,s)\} \\
&\qquad = \frac{1}{4\pi^2}\int_{-\infty}^{\infty} -jd\gamma \int_{-j\infty}^{j\infty} \{C_x^s, C_y^s, C_z^s\} e^{-s(\bar{p}_r r + \bar{q}_s z - \bar{q}_f z_s)} d\bar{p}_r, \\
&\qquad = \frac{1}{2\pi^2}\int_{t_s(0)}^{\infty} e^{-s\tau} d\tau \int_0^{\gamma_s(\tau)} \mathrm{Im}\left[\{C_x^s, C_y^s, C_z^s\} \frac{1}{\partial\tau/\partial\bar{p}_r}\right] d\gamma,
\end{aligned} \tag{2.96}$$

where

$$\begin{aligned}
C_x^p &= \frac{1}{r}(\bar{p}_r x - j\gamma y)T_p, \qquad & C_x^s &= \frac{1}{r}(\bar{p}_r x - j\gamma y)\bar{q}_s T_s, \\
C_y^p &= \frac{1}{r}(\bar{p}_r y + j\gamma x)T_p, \qquad & C_y^s &= \frac{1}{r}(\bar{p}_r y + j\gamma x)\bar{q}_s T_s, \\
C_z^p &= \bar{q}_p T_p, & C_z^s &= (\bar{p}_r^2 - \gamma^2)T_s,
\end{aligned} \tag{2.97}$$

and where $\gamma_p(\tau)$ is the solution to $\tau = t_p(\gamma)$ and $\gamma_s(\tau)$ is the solution to $\tau = t_s(\gamma)$. Modifying the inner integration contour as in the line source case yields for the P-wave Green's function

$$\begin{aligned}
&\{G_x^p(x,y,z,\tau), G_y^p(x,y,z,\tau), G_z^p(x,y,z,\tau)\} \\
&\quad = \begin{cases} 0 & \text{for} \quad -\infty < \tau < t_p(0), \\ \frac{1}{\pi^2}\int_0^{\gamma_p(\tau)} \mathrm{Im}\left[\{C_x^p, C_y^p, C_z^p\} \frac{1}{\partial\tau/\partial\bar{p}_r}\right]_{\bar{p}_r = \bar{p}_r^p(\tau)} d\gamma & \text{for} \quad t_p(0) < \tau < \infty, \end{cases}
\end{aligned} \tag{2.98}$$

with

$$t_p(0) = \bar{p}_r r + z\left(\frac{1}{c_p^2} - \bar{p}_r^2\right)^{1/2} - z_s\left(\frac{1}{c_f^2} - \bar{p}_r^2\right)^{1/2}. \tag{2.99}$$

For the S-wave Green's function we find

$$\begin{aligned}
&\{G_x^s(x,y,z,\tau), G_y^s(x,y,z,\tau), G_z^s(x,y,z,\tau)\} \\
&\quad = \begin{cases} 0 \quad \text{for} \quad -\infty < \tau < t_{ps}, \\ \frac{1}{\pi^2}\int_0^{\gamma_s(\tau)} \mathrm{Im}\left[\{C_x^p, C_y^p, C_z^p\} \frac{1}{\partial\tau/\partial\bar{p}_r}\right]_{\bar{p}_r = \bar{p}_r^{ps}(\tau)} d\gamma & \text{for} \quad t_{ps} < \tau < t_s(0), \\ \frac{1}{\pi^2}\int_0^{\gamma_s(\tau)} \mathrm{Im}\left[\{C_x^p, C_y^p, C_z^p\} \frac{1}{\partial\tau/\partial\bar{p}_r}\right]_{\bar{p}_r = \bar{p}_r^s(\tau)} d\gamma & \text{for} \quad t_s(0) < \tau < \infty, \end{cases}
\end{aligned} \tag{2.100}$$

with

$$t_s(0) = \bar{p}_r r + z\left(\frac{1}{c_s^2} - \bar{p}_r^2\right)^{1/2} - \left(\frac{1}{c_f^2} - \bar{p}_r^2\right)^{1/2} z_s. \tag{2.101}$$

2.7 P- and S-wave separation using wavefield decomposition

This section deals with the wavefield decomposition; a method based on the elastic wave-equation that enables the separation of upgoing waves from downgoing waves and S-waves from P-waves, at a certain level z. Components of particle velocity and traction, describing the two-way wavefield, are related through filters to the P- and S-wave potentials. The filters are derived in the (k_x, k_y, z, ω) domain and are dependent on the medium parameters at the decomposition level. A detailed derivation can be found in the work of Schalkwijk (2001). We follow the same steps but we restrict ourselves to the special case of $k_y = 0$.

First, the source-free linearized equation of motion and the deformation equation are transformed the (k_x, z, ω)-domain. Writing all the terms separately for the equation of motion results in

$$\begin{aligned} j\omega\rho\tilde{v}_x &= -jk_x\tilde{\tau}_{xx} + \partial_z\tilde{\tau}_{xz}, \\ j\omega\rho\tilde{v}_z &= -jk_x\tilde{\tau}_{zx} + \partial_z\tilde{\tau}_{zz}. \end{aligned} \tag{2.102}$$

Assuming an isotropic medium and substituting Eq. 2.6 in the deformation equation gives

$$\begin{aligned} j\omega\tilde{\tau}_{xx} &= -jk_x(\lambda+2\mu)\tilde{v}_x + \lambda\partial_z\tilde{v}_z, \\ j\omega\tilde{\tau}_{zz} &= -jk_x\lambda\tilde{v}_x + (\lambda+2\mu)\partial_z\tilde{v}_z, \\ j\omega\tilde{\tau}_{xz} &= j\omega\tilde{\tau}_{zx} = \mu(-jk_x\tilde{v}_z + \partial_z\tilde{v}_x). \end{aligned} \tag{2.103}$$

The two sets of equations can be arranged and written as a system of first order differential equations as follows

$$\partial_z \begin{pmatrix} \tilde{v}_x \\ -\tilde{\tau}_{zz} \\ -\tilde{\tau}_{xz} \\ \tilde{v}_z \end{pmatrix} = \begin{pmatrix} 0 & 0 & \frac{-j\omega}{\mu} & jk_x \\ 0 & 0 & jk_x & -j\omega\rho \\ -j\omega\rho - \frac{k_x^2}{j\omega}4\mu\frac{(\lambda+\mu)}{(\lambda+2\mu)} & \frac{jk_x\lambda}{(\lambda+2\mu)} & 0 & 0 \\ jk_x\frac{\lambda}{(\lambda+2\mu)} & \frac{-j\omega}{(\lambda+2\mu)} & 0 & 0 \end{pmatrix} \begin{pmatrix} \tilde{v}_x \\ -\tilde{\tau}_{zz} \\ -\tilde{\tau}_{xz} \\ \tilde{v}_z \end{pmatrix}, \tag{2.104}$$

or in a more concise matrix notation

$$\partial_z\tilde{\vec{Q}}^p(z) = \tilde{\mathbf{A}}^p(z)\tilde{\vec{Q}}^p(z), \tag{2.105}$$

where $\tilde{\vec{Q}}^p$ is a permutation of $\tilde{\vec{Q}} = (-\tilde{\tau}_{xz}, -\tilde{\tau}_{zz}, \tilde{v}_x, \tilde{v}_z)^T$. Eigenvalue decomposition of the square matrix $\tilde{\mathbf{A}}^p$ gives

$$\tilde{\mathbf{A}}^p(z) = \tilde{\mathbf{L}}^p(z)\tilde{\mathbf{\Lambda}}(z)[\tilde{\mathbf{L}}^p(z)]^{-1}. \tag{2.106}$$

The eigenvalues are found by solving the characteristic equation

$$det[\tilde{\mathbf{A}}^p - \zeta I] = 0. \tag{2.107}$$

Four eigenvalues are obtained and arranged in the diagonal matrix $\tilde{\mathbf{\Lambda}}$

$$\tilde{\mathbf{\Lambda}}(z) = \begin{pmatrix} -jk_{z,p}(z) & 0 & 0 & 0 \\ 0 & -jk_{z,s}(z) & 0 & 0 \\ 0 & 0 & jk_{z,p}(z) & 0 \\ 0 & 0 & 0 & jk_{z,s}(z) \end{pmatrix}, \tag{2.108}$$

where

$$\begin{aligned} &k_{z,p} = \sqrt{k_p^2 - k_x^2}, \quad k_{z,s} = \sqrt{k_s^2 - k_x^2}, \\ &k_p^2 = \omega^2/c_p^2 = \rho\omega^2/(\lambda + 2\mu), \quad k_s^2 = \omega^2/c_s^2 = \rho\omega^2/\mu. \end{aligned} \tag{2.109}$$

The corresponding eigenvectors are found by solving the following equation for each eigenvalue ζ

$$\tilde{\mathbf{A}}^p \begin{pmatrix} \vec{l}_1 \\ \vec{l}_2 \end{pmatrix} = \zeta \begin{pmatrix} \vec{l}_1 \\ \vec{l}_2 \end{pmatrix}. \tag{2.110}$$

To simplify the derivation, the matrix $\tilde{\mathbf{A}}^p$ is written in a compact form

$$\tilde{\mathbf{A}}^p(z) = \begin{pmatrix} 0 & \tilde{\mathbf{A}}_{12} \\ \tilde{\mathbf{A}}_{21} & 0 \end{pmatrix}, \tag{2.111}$$

and the eigenvector matrix $\tilde{\mathbf{L}}^p$ is (Schalkwijk, 2001)

$$\tilde{\mathbf{L}}^p = \begin{pmatrix} \tilde{\mathbf{L}}_1^p & \tilde{\mathbf{L}}_1^p \\ \tilde{\mathbf{L}}_2^p & -\tilde{\mathbf{L}}_2^p \end{pmatrix}, \tag{2.112}$$

with

$$\begin{aligned} \tilde{\mathbf{L}}_1^p &= (\vec{l}_{1,p} \quad \vec{l}_{1,s}), \\ \tilde{\mathbf{L}}_2^p &= (\vec{l}_{2,p} \quad \vec{l}_{2,s}). \end{aligned} \tag{2.113}$$

The subscripts refer to the eigenvalues $\zeta^2 = -k_{z,p}^2$ and $\zeta^2 = -k_{z,s}^2$. The equations to be solved become then

$$\begin{aligned} \tilde{\mathbf{A}}_{12}\tilde{\mathbf{A}}_{21}\vec{l}_1 &= \zeta^2\vec{l}_1, \\ \tilde{\mathbf{A}}_{21}\tilde{\mathbf{A}}_{12}\vec{l}_2 &= \zeta^2\vec{l}_2. \end{aligned} \tag{2.114}$$

where

$$\tilde{\mathbf{A}}_{12}\tilde{\mathbf{A}}_{21} = \begin{pmatrix} \frac{(3\lambda+4\mu)}{(\lambda+2\mu)}k_x^2 - k_s^2 & \frac{\omega k_x}{\mu}\frac{(\lambda+\mu)}{(\lambda+2\mu)} \\ \frac{2\mu(\lambda+\mu)}{\omega(\lambda+2\mu)}k_x(k_s^2 - 2k_x^2) & \frac{-\lambda k_x^2}{(\lambda+2\mu)} - k_p^2 \end{pmatrix}. \tag{2.115}$$

Since the matrices $\tilde{\mathbf{A}}_{12}$ and $\tilde{\mathbf{A}}_{21}$ are both symmetric, their product

$$\tilde{\mathbf{A}}_{21}\tilde{\mathbf{A}}_{12} = (\tilde{\mathbf{A}}_{12}\tilde{\mathbf{A}}_{21})^T. \tag{2.116}$$

The elements of the eigenvector matrix $\tilde{\mathbf{L}}^p$ are solved by substituting Eqs. 2.115 and 2.116 in Eq. 2.114. We then obtain

$$\tilde{\mathbf{L}}_1^p = \begin{pmatrix} l_{1,p} & l_{1,s} \\ \frac{\mu}{\omega k_x}(k_s^2 - 2k_x^2) l_{1,p} & \frac{-2k_x\mu}{\omega} l_{1,s} \end{pmatrix}, \tag{2.117}$$

and

$$\tilde{\mathbf{L}}_2^p = \begin{pmatrix} l_{2,p} & l_{2,s} \\ \frac{\omega}{2\mu k_x} l_{2,p} & \frac{-\omega k_x}{\mu(k_s^2 - 2k_x^2)} l_{2,s} \end{pmatrix}. \tag{2.118}$$

The normalization factors $l_{1,p}$, $l_{1,s}$, $l_{2,p}$ and $l_{2,s}$ need to be determined. It is convenient to normalize these eigenvectors in terms of P- and S-wave potentials Φ and $\vec{\Psi} = (0, \Psi_y, 0)$, respectively, defined as (Wapenaar & Berkhout, 1989)

$$\begin{aligned} -\rho \partial_t \vec{v}_p &= \nabla \Phi, \\ -\rho \partial_t \vec{v}_s &= \nabla \times \vec{\Psi}. \end{aligned} \tag{2.119}$$

Transforming these expressions to the (k_x, ω)-domain yields for the total wavefield

$$\tilde{\vec{v}} = \frac{-1}{j\omega\rho} \begin{pmatrix} -jk_x \tilde{\Phi} - \partial_z \tilde{\Psi}_y \\ \partial_z \tilde{\Phi} - jk_x \tilde{\Psi}_y \end{pmatrix}, \tag{2.120}$$

where Ψ_y is the y-component of $\vec{\Psi}$. Substituting the following equations into Eq. 2.120:

$$\begin{aligned} \tilde{\Phi} &= \tilde{\Phi}^+ + \tilde{\Phi}^-, \\ \tilde{\Psi}_y &= \tilde{\Psi}_y^+ + \tilde{\Psi}_y^-, \end{aligned} \tag{2.121}$$

and

$$\begin{aligned} \partial_z \tilde{\Phi}^\pm &= \mp jk_{z,p} \tilde{\Phi}^\pm, \\ \partial_z \tilde{\Psi}_y^\pm &= \mp jk_{z,s} \tilde{\Psi}_y^\pm, \end{aligned} \tag{2.122}$$

gives

$$\begin{pmatrix} \tilde{v}_x \\ \tilde{v}_z \end{pmatrix} = \frac{1}{\omega\rho} \begin{pmatrix} k_x & -k_{z,s} \\ k_{z,p} & k_x \end{pmatrix} \begin{pmatrix} \tilde{\Phi}^+ \\ \tilde{\Psi}_y^+ \end{pmatrix} + \frac{1}{\omega\rho} \begin{pmatrix} k_x & k_{z,s} \\ -k_{z,p} & k_x \end{pmatrix} \begin{pmatrix} \tilde{\Phi}^- \\ \tilde{\Psi}_y^- \end{pmatrix}. \tag{2.123}$$

It should be reminded that the positive z-direction is chosen downward and therefore the downgoing potential wavefields are denoted by a $(+)$ sign and the upgoing potential wavefields by a $(-)$ sign. This result is used below for the normalization of the eigenvectors.

We consider again Eq. 2.105 and combine it with Eq. 2.106. It follows that

$$\partial_z \tilde{\vec{Q}}^p(z) = \tilde{\mathbf{L}}^p(z) \tilde{\mathbf{\Lambda}}(z) [\tilde{\mathbf{L}}^p(z)]^{-1} \tilde{\vec{Q}}^p(z). \tag{2.124}$$

Using the definition

$$\tilde{\vec{Q}}^p = \tilde{\mathbf{L}}^p \tilde{\vec{D}}^p, \tag{2.125}$$

we write

$$\partial_z \tilde{\vec{D}}^p(z) = \left[\tilde{\mathbf{\Lambda}}(z) - [\tilde{\mathbf{L}}^p(z)]^{-1} \partial_z \tilde{\mathbf{L}}^p(z)\right] \tilde{\vec{D}}^p(z), \tag{2.126}$$

where $\tilde{\vec{D}}^p$ is a permutation of the vector $\tilde{\vec{D}}(z)$ containing the down- and upgoing wavefields with respect to the z-direction. It can be noticed that when the medium is homogeneous, the down- and upgoing wavefields decouple as the partial derivative of $\tilde{\mathbf{L}}^p$ becomes zero. Consequently, the matrix $\tilde{\mathbf{L}}^p$ can be seen as a composition matrix relating the two-way wavefields described by the components of traction and particle velocity in $\tilde{\vec{Q}}$ to the one-way wavefields in $\tilde{\vec{D}}$. The one-way wavefields can be expressed in terms of the P- and SV-wave potentials, $\tilde{\Phi}$ and $\tilde{\Psi}_y$ so that

$$\tilde{\vec{D}} = (\tilde{\Phi}^+, \tilde{\Psi}_y^+, \tilde{\Phi}^-, \tilde{\Psi}_y^-)^T. \tag{2.127}$$

Comparing Eq. 2.125 or more explicitly,

$$\begin{pmatrix} \tilde{v}_x \\ -\tilde{\tau}_{zz} \\ -\tilde{\tau}_{xz} \\ \tilde{v}_z \end{pmatrix} = \begin{pmatrix} \tilde{\mathbf{L}}_1^p & \tilde{\mathbf{L}}_1^p \\ \tilde{\mathbf{L}}_2^p & -\tilde{\mathbf{L}}_2^p \end{pmatrix} \begin{pmatrix} \tilde{\Phi}^+ \\ \tilde{\Psi}_y^+ \\ \tilde{\Phi}^- \\ -\tilde{\Psi}_y^- \end{pmatrix}, \tag{2.128}$$

to Eq. 2.123, it can be seen that

$$l_{1,p} = \frac{k_x}{\omega\rho}, \qquad l_{1,s} = -\frac{k_{z,s}}{\omega\rho}, \tag{2.129}$$

and

$$l_{2,p} = \frac{2\mu k_{z,p} k_x}{\omega^2\rho}, \qquad l_{2,s} = \frac{-\mu(k_s^2 - 2k_x^2)}{\omega^2\rho}. \tag{2.130}$$

We then obtain

$$\tilde{\mathbf{L}}_1^p = \begin{pmatrix} \frac{k_x}{\omega\rho} & -\frac{k_{z,s}}{\omega\rho} \\ \frac{\mu}{\omega^2\rho}(k_s^2 - 2k_x^2) & \frac{2\mu k_x k_{z,s}}{\omega^2\rho} \end{pmatrix}, \tag{2.131}$$

and

$$\tilde{\mathbf{L}}_2^p = \begin{pmatrix} \frac{2\mu k_x k_{z,p}}{\omega^2\rho} & \frac{-\mu(k_s^2 - 2k_x^2)}{\omega^2\rho} \\ \frac{k_{z,p}}{\omega\rho} & \frac{k_x}{\omega\rho} \end{pmatrix}. \tag{2.132}$$

The set of equations in Eq. 2.125 can be rearranged to $\tilde{\vec{Q}} = \tilde{\mathbf{L}}\tilde{\vec{D}}$, or

$$\begin{pmatrix} -\tilde{\tau}_{xz} \\ -\tilde{\tau}_{zz} \\ \tilde{v}_x \\ \tilde{v}_z \end{pmatrix} = \begin{pmatrix} \tilde{\mathbf{L}}_1^+ & \tilde{\mathbf{L}}_1^- \\ \tilde{\mathbf{L}}_2^+ & \tilde{\mathbf{L}}_2^- \end{pmatrix} \begin{pmatrix} \tilde{\Phi}^+ \\ \tilde{\Psi}_y^+ \\ \tilde{\Phi}^- \\ \tilde{\Psi}_y^- \end{pmatrix}, \tag{2.133}$$

with

$$\tilde{\mathbf{L}}_1^{\pm} = \frac{\mu}{\omega^2\rho}\begin{pmatrix} \pm 2k_x k_{z,p} & -(k_s^2 - 2k_x^2) \\ k_s^2 - 2k_x^2 & \pm 2k_x k_{z,s} \end{pmatrix}, \tag{2.134}$$

$$\tilde{\mathbf{L}}_2^{\pm} = \frac{1}{\omega\rho}\begin{pmatrix} k_x & \mp k_{z,s} \\ \pm k_{z,p} & k_x \end{pmatrix}, \tag{2.135}$$

where $\tilde{\mathbf{L}}_1^+$ and $\tilde{\mathbf{L}}_2^+$ are the composition sub-matrices for the downgoing part of the wavefields, and $\tilde{\mathbf{L}}_1^-$ and $\tilde{\mathbf{L}}_2^-$ are the composition sub-matrices for the upgoing part of the wavefields.

The decomposition operator $\tilde{\mathbf{N}}$ is the inverse of the composition operator $\tilde{\mathbf{L}}$ such that

$$\tilde{\vec{D}} = \tilde{\mathbf{L}}^{-1}\tilde{\vec{Q}} = \tilde{\mathbf{N}}\tilde{\vec{Q}}, \tag{2.136}$$

where

$$\tilde{\mathbf{N}} = \begin{pmatrix} \tilde{\mathbf{N}}_1^+ & \tilde{\mathbf{N}}_2^+ \\ \tilde{\mathbf{N}}_1^- & \tilde{\mathbf{N}}_2^- \end{pmatrix}, \tag{2.137}$$

with

$$\tilde{\mathbf{N}}_1^{\pm} = \frac{1}{2}\begin{pmatrix} \pm\frac{k_x}{k_{z,p}} & 1 \\ -1 & \pm\frac{k_x}{k_{z,s}} \end{pmatrix}, \tag{2.138}$$

$$\tilde{\mathbf{N}}_2^{\pm} = \frac{\mu}{2\omega}\begin{pmatrix} 2k_x & \pm\frac{(k_s^2 - 2k_x^2)}{k_{z_p}} \\ \mp\frac{k_s^2 - 2k_x^2}{k_{z,s}} & 2k_x \end{pmatrix}. \tag{2.139}$$

Eq. 2.136 enables then the separation of the down- and upgoing wavefields in terms of P- and S-wave potentials at a given level z provided that the medium parameters at this level are known. In practice, the components of traction needed for the decomposition are not measured. However, in the environment of interest, this wave-equation based method has been successfully applied to multicomponent ocean-bottom (OBC) data (Schalkwijk *et al.*, 2003) by rewriting Eq. 2.136 and imposing the boundary conditions associated with a fluid-solid interface. As described in section 2.4, these boundary conditions require the equality of the opposite of pressure in the fluid to the normal component of traction and the vanishing of the tangential component of traction.

In Chapter 6 of this thesis, we discuss how this theory is implemented to separate P- and S-waves in the case of a multicomponent data set recorded in shallow water-bottom.

2.8 Appendix A: Fourier-transform conventions and definitions

The forward temporal Fourier transform $\hat{\tilde{v}}(x, y, \omega)$ of function $v(x, y, t)$ is defined as

$$\hat{\tilde{v}}(x, y, \omega) = \int_{-\infty}^{\infty} v(x, y, t)e^{-j\omega t}dt, \tag{2.140}$$

and the inverse temporal Fourier transform as

$$v(x,y,t) = \frac{1}{2\pi}\int_{-\infty}^{\infty} \hat{\tilde{v}}(x,y,\omega)e^{j\omega t}d\omega, \tag{2.141}$$

where ω is the angular frequency. Since the time-domain response $v(x,y,t)$ is real-valued, we can write

$$\hat{\tilde{v}}(x,y,-\omega) = \hat{\tilde{v}}^*(x,y,\omega), \tag{2.142}$$

where the asterisk denotes complex conjugation. Consequently, the negative frequencies are not required for the inverse transform, which can then be written as

$$v(x,y,t) = \frac{1}{\pi}\mathrm{Re}\int_{0}^{\infty} \hat{\tilde{v}}(x,y,\omega)e^{j\omega t}d\omega. \tag{2.143}$$

The two-dimensional spatial Fourier transform with respect to the horizontal Cartesian coordinate x and y is defined as

$$\tilde{v}(k_x,k_y,\omega) = \iint_{-\infty}^{\infty} \hat{\tilde{v}}(x,y,\omega)e^{j(k_x x+k_y y)}dxdy, \tag{2.144}$$

and the inverse spatial Fourier transform as

$$\hat{\tilde{v}}(x,y,\omega) = \frac{1}{4\pi^2}\iint_{-\infty}^{\infty} \tilde{v}(k_x,k_y,\omega)e^{-j(k_x x+k_y y)}dk_x dk_y, \tag{2.145}$$

where k_x and k_y denote the horizontal wavenumbers in the x and y direction respectively.

In this thesis, the wavefields are expressed in various domains. A list of the symbols corresponding to each domain is provided below

$v(x,y,z,t)$	space-time domain,
$\hat{\tilde{v}}(x,y,z,\omega)$	space-frequency domain,
$\tilde{v}(k_x,k_y,z,\omega)$	horizontal wavenumbers-frequency domain,
$\tilde{\tilde{v}}(k_x,k_y,k_z,\omega)$	wavenumber-frequency domain.

Chapter 3

Non-geometric PS-converted wave in a fluid-solid configuration: characteristics and potential use

3.1 Introduction

Non-geometric S-waves are excited when the dominant wavelength of a point source exceeds the distance between the source and a plane interface separating two media with different elastic properties (Hron & Mikhailenko, 1981). The excited S-waves appear to be originating from the projection point of the source on the interface, therefore, their kinematic behavior is considered to be non-geometric. The existence of this type of arrivals was predicted in theory by Brekhovskikh (1960) and categorized along with the head waves as lateral waves. Hron & Mikhailenko (1980) were the first to report the existence of a specific type of non-geometric S-wave in their synthetic seismogram. This arrival, referred to in seismology as the S*-arrival, was generated by a P-wave source buried close to the free surface. In the past decades, other non-geometric S-modes, including the SH*-arrival (Daley & Hron, 1988) and more recently the $\bar{P}S$ phase (Roth & Holliger, 2000), have been identified in synthetic and real data.

The S*-arrivals are physically interpreted as evanescent P-waves that tunnel to the free-surface interface where they convert to a propagating shear mode (Daley & Hron, 1983b). Evanescent waves are often neglected because of their exponentially decaying amplitude as a function of depth. However, when the source is moved closer to the interface, the conversion of the tunneling P-waves to a propagating S-mode becomes more significant (Gutowski *et al.*, 1984), thereby increasing by that their detectability in synthetic seismograms.

Recently, field data evidence of non-geometric PS-converted waves renewed our interest in this particular type of arrivals. Unlike the S*-arrivals, these waves were observed in a data set acquired in a shallow water environment (Allouche *et al.*, 2011). They were generated by a source with a low frequency content towed in the water and recorded by 3-C geophones and hydrophones placed on the water bottom. Due to the low apparent velocity of these waves and the linear horizontal polarization, the hyperbolically shaped arrivals were interpreted as S-wave reflections. A modelling study revealed that these S-waves are not traveling according

to Snell's law and were consequently classified as non-geometric.

In this chapter, we show that the recently discovered non-geometric PS-wave features the same properties as the S*-wave. We verify the existence of this specific mode in a fluid-solid configuration by deriving and computing the transmitted wavefield in the solid. Using the Cagniard-de Hoop technique, the main properties of the PS-conversion in the near-field are studied and their relevance to shallow marine seismics is discussed. Finally, we propose a method to separate the modes converted at the water bottom from the data using the Radon transform.

3.2 Transmitted wavefield in a fluid-solid configuration

3.2.1 Theory

To understand the nature of the non-geometric PS-waves, we derive the transmitted wavefield for the fluid-solid configuration shown in figure 3.1. The source is located at height z_s in the upper halfspace ($z < 0$), consisting of an ideal fluid and the receivers are buried in the homogeneous, isotropic and elastic solid ($z > 0$). The generated pressure field $P(x, z, t)$, propagating in the fluid with a speed c_f, satisfies the inhomogeneous wave equation

$$\nabla^2 P - \frac{1}{c_f^2}\frac{\partial^2 P}{\partial t^2} = -\delta(x, z)S(t), \tag{3.1}$$

where $S(t)$ denotes the source signature. When we consider a Cartesian coordinate system and assume a line source along the y-direction, the well-known solution of this equation, for a given angular frequency ω, can be written in terms of the Weyl's integral, representing a superposition of plane waves (Aki & Richards, 2002)

$$P^i(x, z, t) = \frac{1}{4\pi r}S(t - r/c_f) = \frac{1}{2\pi^2}\mathrm{Re}\int_0^\infty \hat{S}(\omega)d\omega \int_{-\infty}^{\infty} \frac{1}{2jq_f}e^{j\omega(t-px-q_f|z-z_s|)}dp, \tag{3.2}$$

in which

$$r = \sqrt{x^2 + z^2}, \tag{3.3}$$

and where P^i denotes the incident pressure field, $\hat{S}(\omega)$ is the source spectrum and p is the horizontal slowness. To satisfy the radiation condition, we define the vertical slowness in the fluid as $q_f = \sqrt{1/c_f^2 - p^2}$ with $\mathrm{Im}(q_f) < 0$.

In the solid, the particle velocity $\vec{v}(x, z, t)$ is governed by the elastic wave equation:

$$(\lambda + \mu)\nabla(\nabla \cdot \vec{v}) - \mu\nabla \times \nabla \times \vec{v} - \rho_s\frac{\partial^2 \vec{v}}{\partial t^2} = 0, \tag{3.4}$$

where λ and μ are the Lamé parameters and ρ_s is the density in the solid. The particle velocity can be decomposed into curl-free P-wave and divergence-free S-wave contributions:

$$\vec{v}(x, z, t) = \vec{v}^p(x, z, t) + \vec{v}^s(x, z, t). \tag{3.5}$$

Similarly to the pressure in the fluid, these contributions are expressed in terms of plane waves superposition

$$\begin{aligned} v_x(x,z,t) &= \frac{1}{2\pi^2}\mathrm{Re}\int_0^\infty d\omega \int_{-\infty}^{\infty} \frac{\hat{S}(\omega)}{2jq_f}\Big[A_x^p e^{j\omega(t-px-q_p z+q_f z_s)} \\ &\qquad +A_x^s e^{j\omega(t-px-q_s z+q_f z_s)}\Big]\, dp, \\ v_z(x,z,t) &= \frac{1}{2\pi^2}\mathrm{Re}\int_0^\infty d\omega \int_{-\infty}^{\infty} \frac{\hat{S}(\omega)}{2jq_f}\Big[A_z^p e^{j\omega(t-px-q_p z+q_f z_s)} \\ &\qquad +A_z^s e^{j\omega(t-px-q_s z+q_f z_s)}\Big]\, dp, \end{aligned} \tag{3.6}$$

where v_x and v_z are the particle velocity components in the x and z-direction, respectively. The vertical slownesses q_p and q_s, associated with the P- and S-wave, satisfy the radiation condition such that

$$\begin{aligned} q_p &= \sqrt{1/c_p^2 - p^2} \quad \text{with} \quad \mathrm{Im}(q_p) < 0, \\ q_s &= \sqrt{1/c_s^2 - p^2} \quad \text{with} \quad \mathrm{Im}(q_s) < 0. \end{aligned} \tag{3.7}$$

The amplitude factors of the transmitted P- and S-wave in the x-direction, A_x^p and A_x^s, and in the z-direction, A_z^p and A_z^s, are related to the amplitude of the source spectrum $\hat{S}(\omega)$ according to

$$\begin{aligned} A_x^p &= \frac{p}{\rho_f}T_p, \qquad A_x^s = \frac{q_s}{\rho_f}T_s, \\ A_z^p &= \frac{q_p}{\rho_f}T_p, \qquad A_z^s = \frac{-p}{\rho_f}T_s, \end{aligned} \tag{3.8}$$

where T_p is the transmission coefficient and T_s is the conversion coefficient. These coefficients are derived by satisfying the boundary conditions associated with a fluid-solid interface. Writing the coefficients as particle velocity ratios and in similar form as de Hoop & van der Hijden (1983), gives

$$T_p = (\rho_f/\rho_s)(1/2c_s^2 - p^2)/c_s^2\Delta_{SCH}, \tag{3.9}$$

$$T_s = -(\rho_f/\rho_s)pq_p/c_s^2\Delta_{SCH}, \tag{3.10}$$

with

$$\Delta_{SCH} = \rho_f q_p/4c_s^4\rho_s q_f + (p^2 - 1/2c_s^2)^2 + p^2 q_p q_s, \tag{3.11}$$

a term known as the Scholte-wave denominator, which is associated with surface waves propagating along the fluid-solid interface (de Hoop & van der Hijden, 1983).

Substituting the expressions found for the amplitude factors in Eq. 3.6 results in

$$v_x(x,z,t) = \frac{1}{2\pi^2}\mathrm{Re}\int_0^\infty \hat{S}(\omega)d\omega \int_{-\infty}^{\infty} \frac{1}{2jq_f\rho_f}\Big[pT_p e^{j\omega(t-px-q_p z+q_f z_s)} + q_s T_s e^{j\omega(t-px-q_s z+q_f z_s)}\Big]\, dp,$$

$$v_z(x,z,t) = \frac{1}{2\pi^2}\mathrm{Re}\int_0^\infty \hat{S}(\omega)d\omega \int_{-\infty}^{\infty} \frac{1}{2jq_f\rho_f}\Big[q_p T_p e^{j\omega(t-px-q_p z+q_f z_s)} - pT_s e^{j\omega(t-px-q_s z+q_f z_s)}\Big]\, dp. \quad (3.12)$$

The total wavefield in the solid for a given frequency, composed of the transmitted P-wave and the converted S-wave, is obtained by integrating over the horizontal slowness p. The amplitude contribution to the PS-wave is determined by the conversion coefficient T_s and their propagation is dependent on the vertical slownesses q_f and q_s. From the definition of these slownesses, it can be deduced that when $c_s < c_f$, the vertical slowness associated with the pressure wave in the fluid, q_f, becomes imaginary for p-values exceeding $1/c_f$ whereas q_s, the vertical slowness related to the S-mode in the solid is still real in the range $1/c_f < p < 1/c_s$. In this particular case, the incident fluid wave with an amplitude decaying exponentially ($\sim e^{-\omega\sqrt{p^2-1/c_f^2}|z_s|}$) with depth is converted at the interface to a propagating S-mode giving rise to the non-geometric PS-wave (P*S). However, if $c_s > c_f$, the converted S-wave becomes imaginary for p-values larger than $1/c_s$ while the incident fluid wave is real in the p-value range $1/c_s < p < 1/c_f$. In this case, the S-wave is propagating only along the interface giving rise to the FS-head wave.

3.2.2 Synthetic example

To illustrate the difference between the geometric and non-geometric PS-conversion at the fluid-solid interface, we adopted two simple models consisting of a fluid halfspace, with $c_f = 1500$ m/s and $\rho_s = 1000$ kg/m^3, overlying an elastic layer with seismic properties representative of: 1) a slow formation with $c_p = 1650$ m/s, $c_s = 200$ m/s and $\rho_s = 1200$ kg/m^3 and 2) a fast formation with $c_p = 4500$ m/s, $c_s = 2100$ m/s and $\rho_s = 2500$ kg/m^3. We make also a distinction between two types of conversions. One conversion occuring due to a source placed at height $h = 2\lambda$, and the second occurring due to a source placed at height $h = \lambda/8$ with respect to the interface, with λ being the dominant wavelength of the source in the fluid. Figure 3.2 shows the horizontal component of the transmitted wavefields computed for receivers located 50 m below the fluid-solid interface.

For the soft formation, the transmitted wavefield is composed of two events, namely the transmitted P-wave and the converted S-wave. However, when the source is situated closer to the interface, a third distinctive event with a lower dominant frequency appears (compare figures 3.2(a) and 3.2(b)). The low apparent velocity is indicative of this event identified as the non-geometric PS-wave (P*S). For the stiff solid, there is no difference between the two cases as shown in figures 3.2(c) and 3.2(d). In both cases, the response consists of the transmitted P-wave, the converted S-wave and the PS-head-wave.

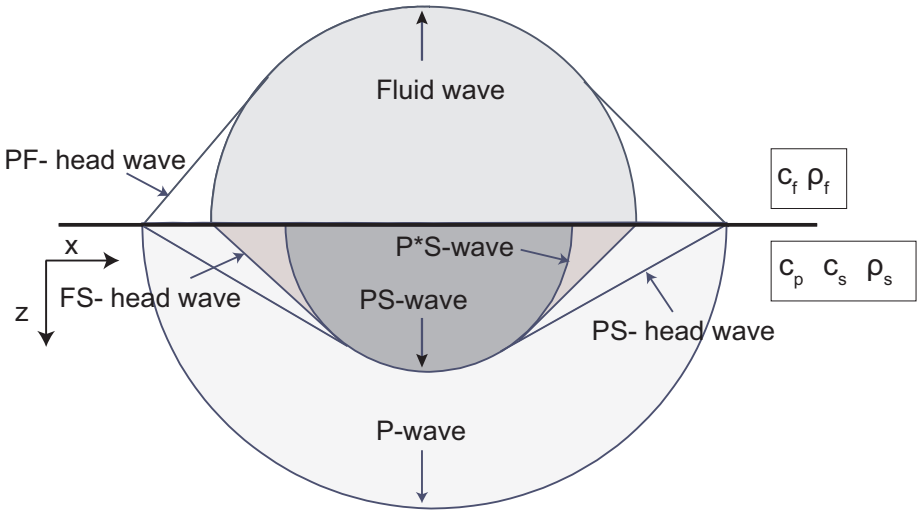

Figure 3.1: *Schematic of the wavefield generated by a source located in a fluid halfspace, overlying a solid halfspace, for the case* $c_s < c_f$.

3.2.3 Mapping the response in the linear Radon domain

As explained in the theory, the non-geometric arrivals are confined to a specific range of horizontal slownesses p between $1/c_f$ and $1/c_s$. A convenient way to illustrate this is to map the wavefield into the linear Radon domain (Deans, 1983) by merely summing the traces along lines with constant p-values according to

$$\widetilde{\vec{v}}(p,\tau) = \int_{-\infty}^{+\infty} \vec{v}(x, \tau + px)dx, \tag{3.13}$$

where τ is the intercept time defined as $\tau = t - px$. Because the horizontal slowness can also be defined as $p = \Delta t/\Delta x$, the transformed data can be interpreted as a representation of all the dip components present in the response. The steepest part of the slowest event, the asymptote of its hyperbola, is the maximum p-value at which the data are mapped in the (τ, p) domain.

For the soft formation example, with $h = 2\lambda$, the maximum p-value corresponds to the asymptote of the converted wave which equals the inverse speed of the fluid wave, as demonstrated in figure 3.3(a). However, if the source is placed at $h = \lambda/8$ and the non-geometric PS-wave is excited, it can be observed in figure 3.3(b) that the maximum p-value in this case becomes the inverse of the S-wave velocity. The non-geometric PS-wave is stacked along slopes ranging between $[-1/c_s, -1/c_f]$ and $[1/c_f, 1/c_s]$ and is not overlapping with the transmitted P-wave, making it easier to separate in this domain. No notable differences, caused by changing the source height, are observed in the Radon-transformed responses of the stiff formation (compare figures 3.3(c) and 3.3(d)), confirming the fact that non-geometric PS-waves are not excited in this case.

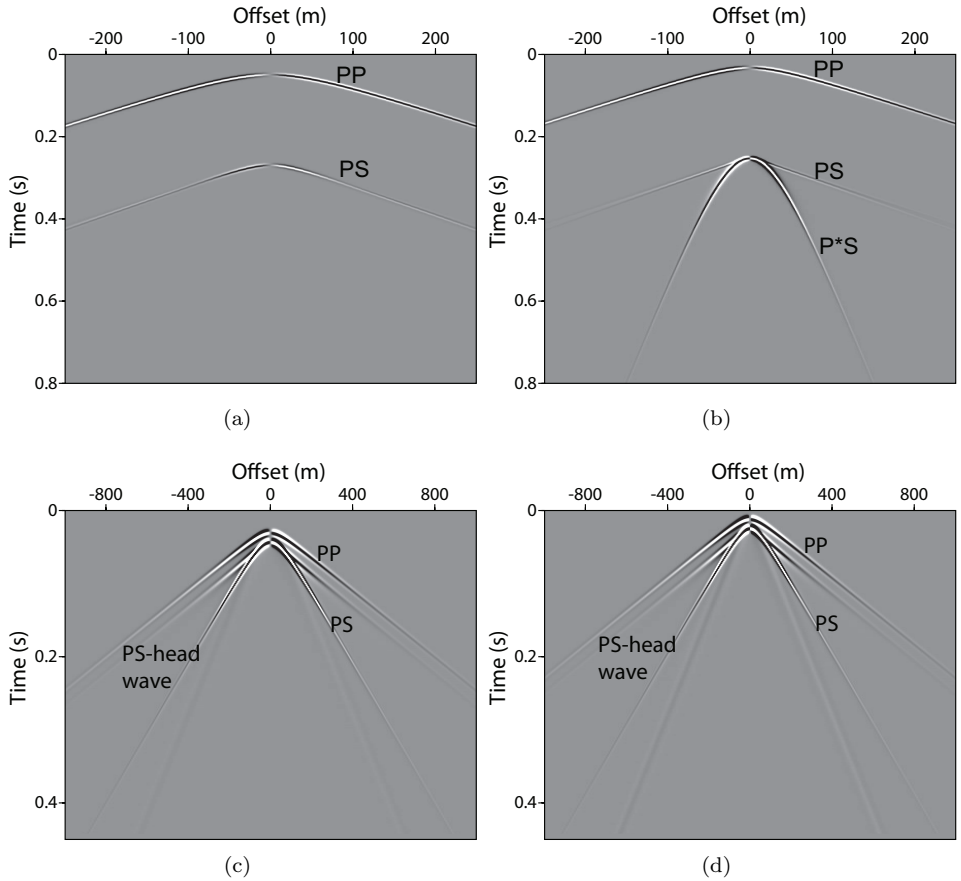

Figure 3.2: *The horizontal component of the transmitted wavefields computed for: soft formation model with the source located at height $h = 2\lambda$ (a) and $h = \lambda/8$ above the interface (b), and the stiff formation model with the source located at height $h = 2\lambda$ (c) and $h = \lambda/8$ (d) above the interface.*

3.3 Properties of the non-geometric PS-wave using the Cagniard-de Hoop method

Non-geometric arrivals have specific properties which distinguish them from other types of events. These properties are discussed in the literature mainly with reference to the S*-wave. In this section, we verify whether the identified non-geometric PS-mode, associated with a fluid-solid configuration, features the same properties. The Cagniard-de Hoop method is suitable for this purpose because it provides an exact solution for the PS-converted wave, expressed explicitly in the space-time domain. This is done by modifying the integration path along p into a form that can be recognized as the impulse response or the Green's function. The basics about

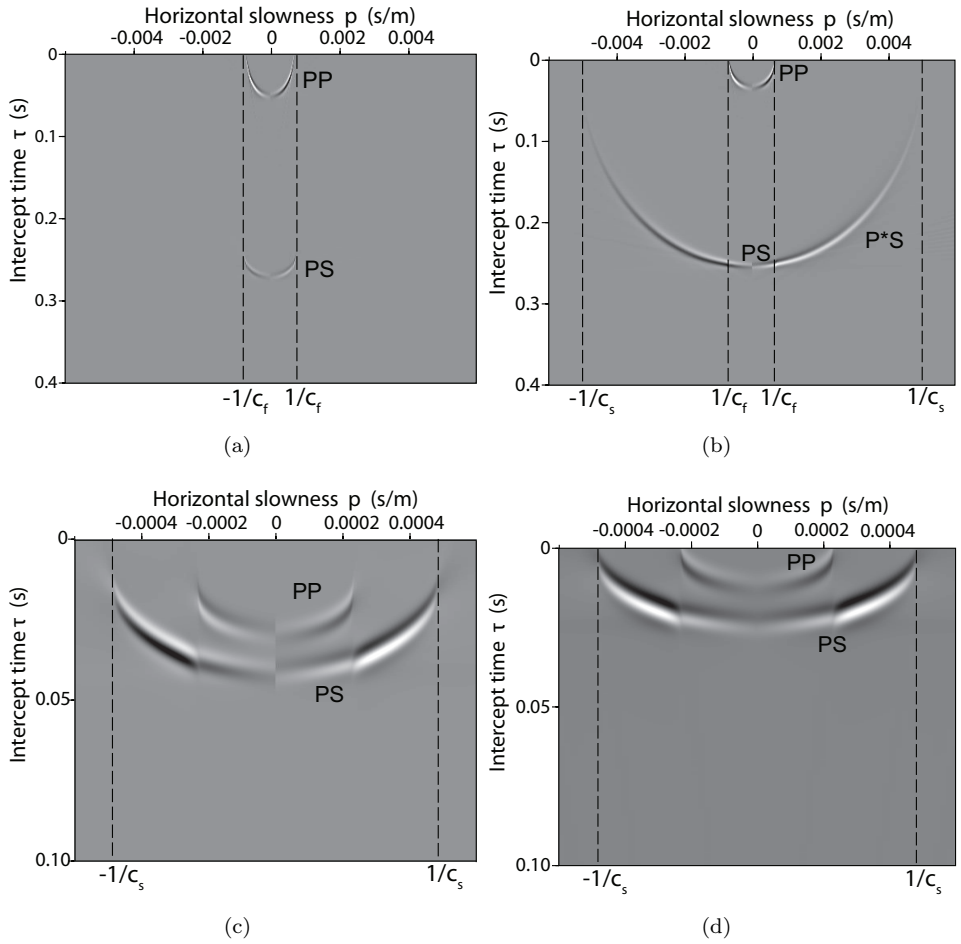

Figure 3.3: *The horizontal component of the transmitted wavefield mapped in the linear Radon domain: soft formation model with the source located at height $h = 2\lambda$ (a) and $h = \lambda/8$ above the interface (b), and the stiff formation model with the source located at height $h = 2\lambda$ (c) and $h = \lambda/8$ (d) above the interface. The dashed lines denote the maximum p-value of the geometric $(1/c_f)$ and non-geometric waves $(1/c_s)$.*

this method are treated by several authors (de Hoop & van der Hijden, 1983; Drijkoningen & Chapman, 1988; Chapman, 2004) and will not be discussed with many details in this chapter.

We start by omitting the factor $\hat{S}(\omega)$, associated with the source, from Eq. 3.12 and introduce it later to the time domain expression by convolution. The PS-

response in the space-frequency domain is then

$$\{\hat{v}_x^s(x,z,\omega),\hat{v}_z^s(x,z,\omega)\} = \frac{j}{2\pi}\int_{-\infty}^{\infty}\{C_x(p),C_z(p)\}T_s e^{-j\omega(px+q_s z-q_f z_s)}dp, \quad (3.14)$$

where $\{C_x(p),C_z(p)\} = \{-q_s/(2q_f\rho_f), p/(2q_f\rho_f)\}$. The p-contour of integration can be distorted from the real axis to the Cagniard contour by solving for $\mathrm{Im}(\tau)=0$ where $\tau = px + q_s z - q_f z_s$.

Since the function τ is quartic for p, the square roots are seeked numerically. We are considering $c_s < c_f < c_p$, the case in which the non-geometric PS-waves are excited. It is therefore possible that p_s, the p-value corresponding to the transmitted S-wave, crosses the branch cuts $1/c_p$ and $1/c_f$ giving rise to head waves. We find the following expressions for the Green's function $G^s(x,z,\tau)$

$$\{G_x^s(x,z,\tau),G_z^s(x,z,\tau)\} = \begin{cases} 0 & \text{for } -\infty < \tau < t_{hw} \\ \frac{1}{\pi}\mathrm{Im}\left[\{C_x,C_z\}\frac{T_s}{\partial\tau/\partial p}\right]_{p=p_{hw}(\tau)} & \text{for } t_{hw} < \tau < t_s \\ \frac{1}{\pi}\mathrm{Im}\left[\{C_x,C_z\}\frac{T_s}{\partial\tau/\partial p}\right]_{p=p_s(\tau)} & \text{for } t_s < \tau < \infty \end{cases}$$

where

$$\partial\tau/\partial p = x - \frac{p}{\gamma_s}z + \frac{p}{\gamma_f}z_s, \quad (3.15)$$

t_s is the travel time of the S-wave and

$$t_{hw} = \frac{x}{c_p} + \sqrt{\frac{1}{c_s^2}-\frac{1}{c_p^2}}z - \sqrt{\frac{1}{c_f^2}-\frac{1}{c_p^2}}z_s, \quad (3.16)$$

is the travel time of the head wave.

It should be noted that, for the studied case, two head waves are generated: a PS head-wave related to the P-wavefront in the solid and another one related to the pressure wave in the fluid (see figure 3.1). The Cagniard-de Hoop method does not make a distinction between these two events. Since $c_p > c_f$, the head wave denoted in the derived response is the one associated with the P-wave in the solid.

In the synthetic example, we have shown that the non-geometric PS-wave is observed when the ratio between the dominant wavelength and the source height is fractional ($h/\lambda = 1/8$). As explained in the theory, this is caused by the evanescent nature of this wave in the fluid and its amplitude is, therefore, exponentially dependent on the source height. Figure 3.4 illustrates the amplitude and phase behavior of the PS-wave as a function of h/λ, computed with the Cagniard-de Hoop solution for two receiver positions. At the first receiver, located 5 m from the source, the PS-wave is geometric and decays less rapidly than the non-geometric one, visible on the second receiver, as the source is moved away from the interface (compare figures 3.4(a) and 3.4(c)). The latter even disappears as the ratio h/λ exceeds one. A clear trend in the associated Cagniard path is also observed when the ratio h/λ is increased. For the second receiver, where the non-geometric PS-wave is diverged from the head-wave, the curve gets closer to the real axis and at a certain point

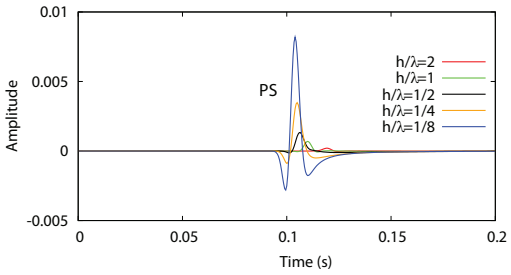

(a)

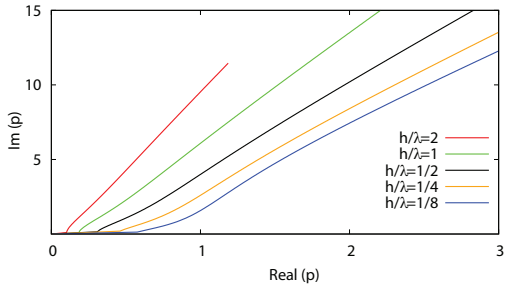

(b)

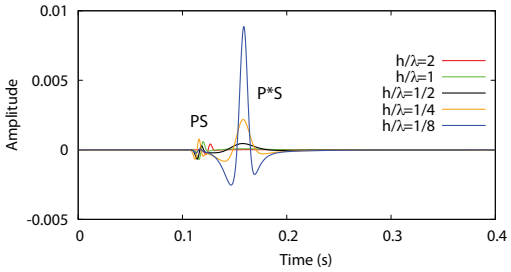

(c)

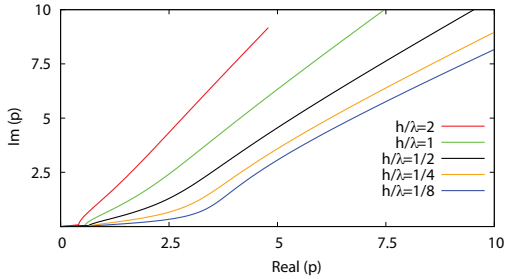

(d)

Figure 3.4: *a) The horizontal component of the PS-wave response computed for different h/λ ratios at a receiver located 5 m away from the source and b) the corresponding modified Cagniard paths. c) The PS-wave response computed for different h/λ ratios at a receiver located 50 m away from the source and d) the corresponding modified Cagniard paths.*

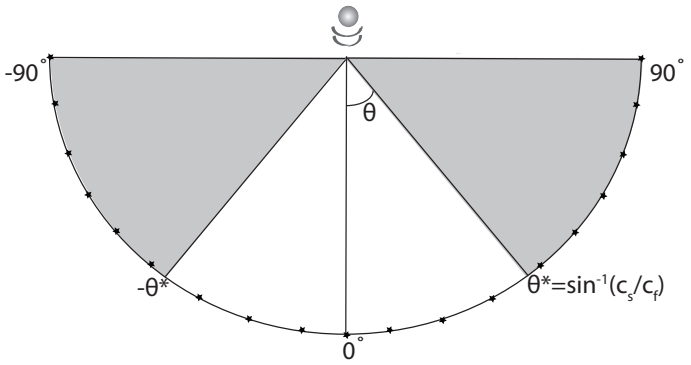

(a)

Figure 3.5: *Sketch of the existence region of the P*S-wave. The shaded area indicates the angles at which the P*S-wave appears.*

it bends away rapidly (see figure 3.4(d)). If the source was actually placed on the interface, the contour would intersect with the real axis at this specific point and this ray would correspond to the geometric S-wave arrival (Drijkoningen & Chapman, 1988; Hong & Helmberger, 1977). The bend in the Cagniard path is due to the ray $p = \sin\theta/c_s$ where θ is the angle shown in figure 3.5. Approximations of non-geometric arrivals can be deduced by expanding around this specific ray (Drijkoningen & Chapman, 1988). The range of existence of the non-geometric PS-wave is restricted at one side by $p = 1/c_f$ and therefore it appears first at the angle $\theta^* = \sin^{-1}(c_s/c_f)$. This implies that the angle of appearance θ^* is dependent on the ratio between the S-wave velocity in the solid and the sound speed in the fluid (c_s/c_f). We can easily verify this by computing the response for the configuration drawn in figure 3.5. The results modeled for two c_s/c_f ratios are displayed in figure 3.6. For a high c_s/c_f ratio of 1000/1500, the non-geometric PS-wave appears at $\theta^* = 41.8°$, where it diverges from the two head waves. However, when c_s/c_f is low, such as 200/1500 in figure 3.6(b), the angle of appearance is rather small $(\theta^* = 7.7°)$.

3.4 Separation of non-geometric PS-waves using linear and parabolic Radon transforms

Based on the discussed properties of the non-geometric PS-wave, it can be stated that this mode has the potential to be useful to infer S-wave information and image the shallow marine subsurface using such S-waves. Particularly, the kinematic behavior of this wave is beneficial. The non-geometric wave behaves as if it was generated at the water bottom without actually having to put the source there. This may considerably increase the efficiency of collecting S-wave data in the field. As shown in the synthetic example, a convenient method to identify these arrivals

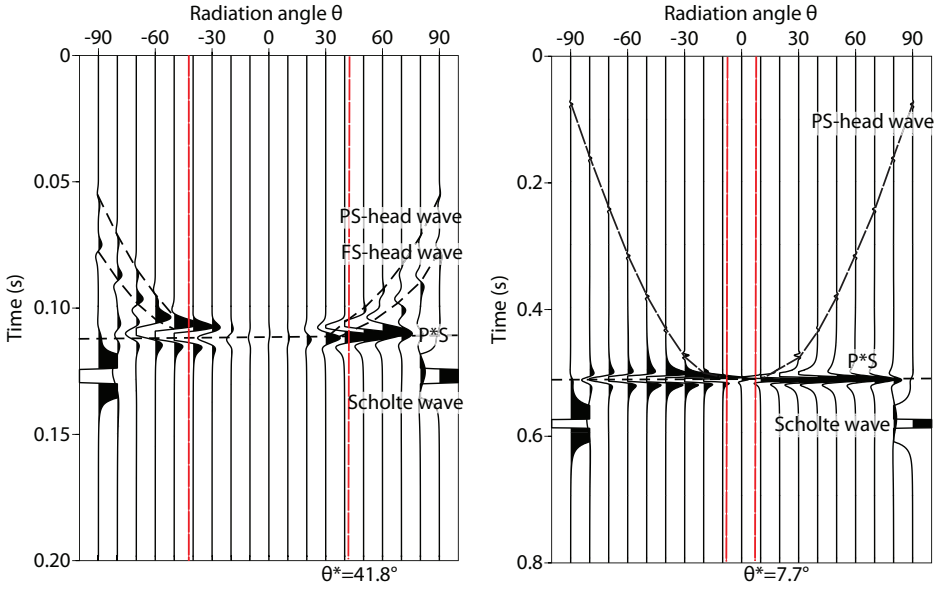

Figure 3.6: *The PS-wave response computed for different angles (see figure 3.5 for the configuration): a) solid with* $c_s/c_f = 1000/1500$ *and a corresponding angle of appearance* $\theta^* = 41.8°$ *and b) solid with* $c_s/c_f = 200/1500$ *and a corresponding angle of appearance* $\theta^* = 7.7°$.

is to transform the wavefield to the Radon domain. This domain is also appropriate to separate the geometric arrivals from the non-geometric ones as we will show in this section. For this purpose, we define a simple horizontally layered model with the seismic properties shown in figure 3.7 and compute its full response using reflectivity modelling (Fuchs & Müller, 1971; Schmidt, 1988). The source is located in the water at height $h = \lambda/8$, with $\lambda = 15$ m for the peak frequency of 100 Hz. The receivers are placed on the water bottom.

In figure 3.8(a), various types of events are identified and labeled in the computed horizontal component of the wavefield. After performing a linear Radon transform, it can be noticed that the events are quite well separated in this domain. All the P-waves and geometric PS-reflections are mapped within the two lines, representing the horizontal slownesses $-1/c_f$ and $1/c_f$. Outside the denoted region, the non-geometric PS-waves and the Scholte waves are recognized. Practically, we can transform the two regions separately back to the space-time domain, thereby filtering either the geometric or the non-geometric waves. In figure 3.9, the filtered outcomes are compared. In addition to the P-waves and the PS-waves converted at reflectors in the sediments, the apex of the reflection hyperbola, belonging to the PS-modes converted at the water bottom, are confined to the geometric part as well. However, since we aim to process these specific PS-modes, behaving kinematically

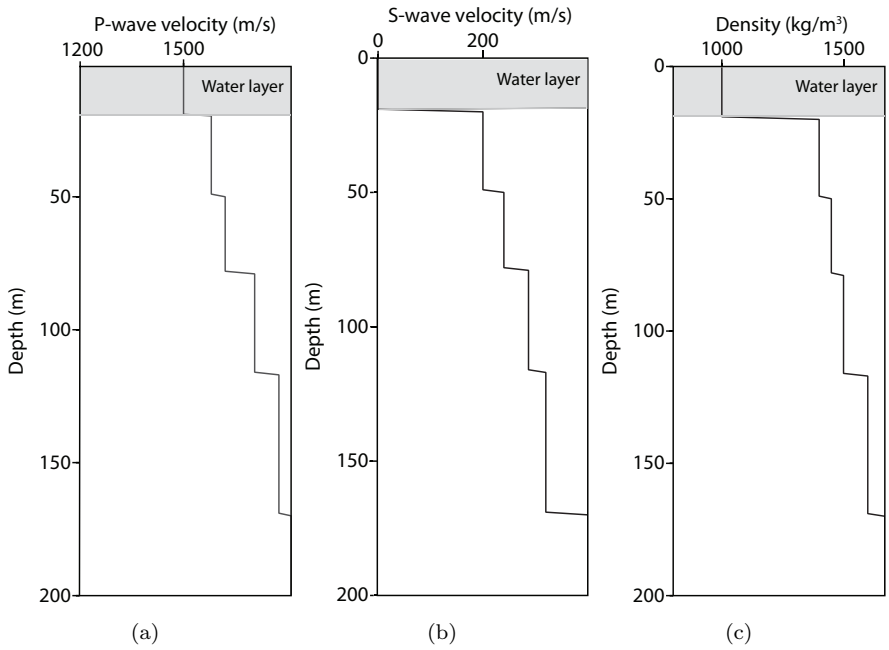

Figure 3.7: *a) P-wave velocity profile, b) S-wave velocity profile and c) density used for modelling.*

as pure S-waves, separately, such a filter is not desirable.

To preserve the geometric and non-geometric part of the PS-waves converted at the water bottom, it is better to filter these in the parabolic Radon domain, defined as follows

$$\widetilde{\vec{v}}(q,\tau) = \int_{-\infty}^{+\infty} \vec{v}(x, \tau + qx^2)dx, \tag{3.17}$$

where q is the curvature and τ is the intercept time. Figure 3.10(a) shows the result of transforming the wavefield using Eq. 3.17. The reflections of interest, denoted by black arrows, are identified by their intercept time and their strong curvature. We separate these converted modes by muting the remaining arrivals and transforming the filtered part of the wavefield back to the space-time domain. The final result, displayed in figure 3.10(b), consists only of modes converted at the water bottom and kinematically behaving as if they were generated by a shear source.

3.5 Conclusions

In this chapter, we have shown the existence of the non-geometric PS-wave in a fluid-solid configuration by analyzing the transmitted wavefield. This particular mode of conversion is excited only when the S-wave velocity in the solid is lower than the sound speed in the fluid and becomes detectable on synthetic seismograms

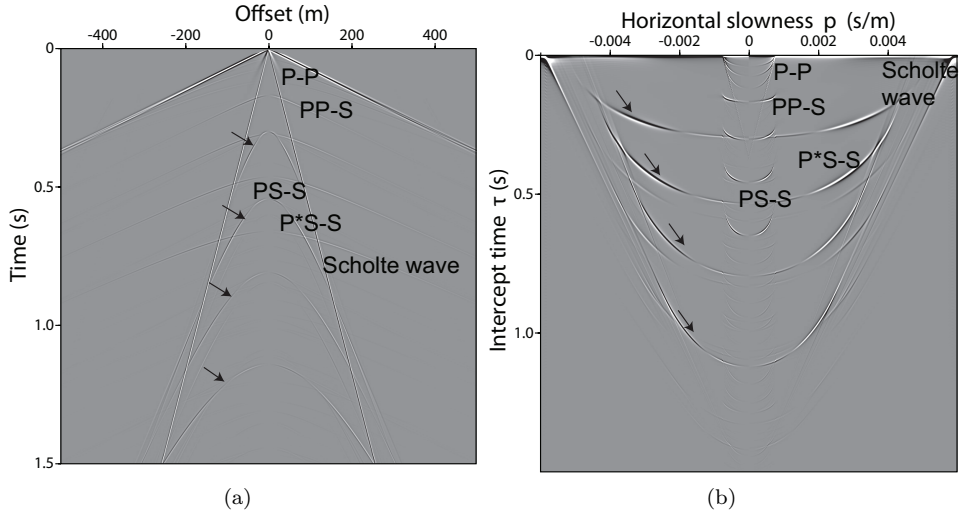

Figure 3.8: *The horizontal component of the computed wavefield in the space-time domain (a) and in the linear Radon domain (b).*

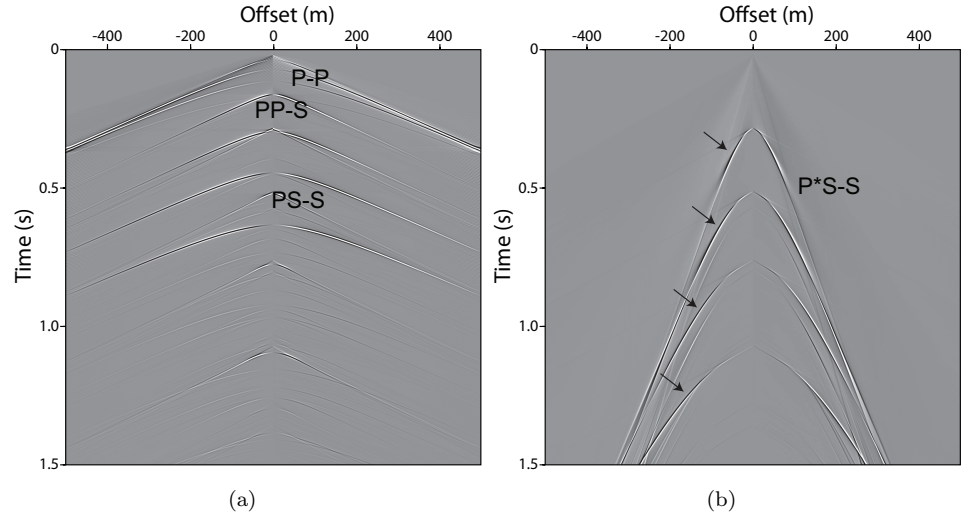

Figure 3.9: *a) The filtered geometric events and b) the filtered non-geometric events.*

if the dominant wavelength of the emitted signal exceeds the source height.

The existence of the non-geometric PS-wave is restricted to a range of horizontal slownesses varying between $[-1/c_s, -1/c_f]$ and $[1/c_f, 1/c_s]$, whereas the P-wave is confined to the range $[-1/c_p, 1/c_p]$. In the solid, this wave appears at a specific angle measured from the projection point of the source on the interface, where it

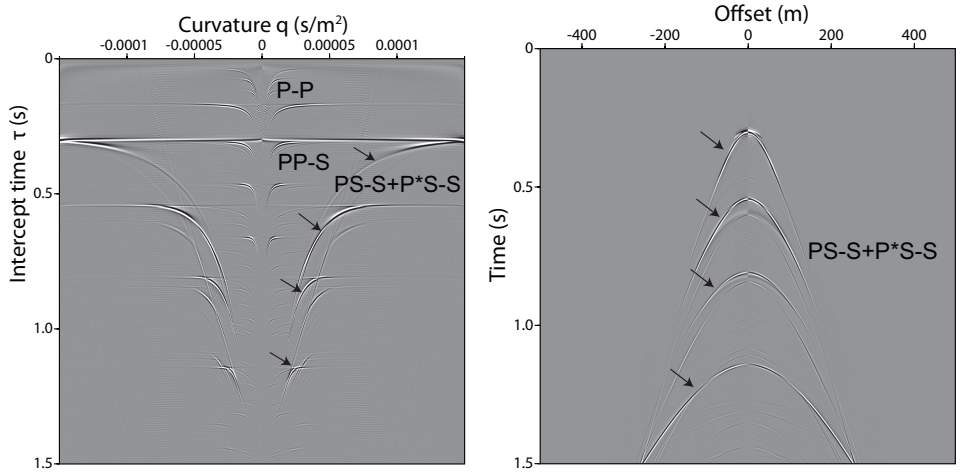

(a) (b)

Figure 3.10: *a) The transformed wavefield in the parabolic Radon domain and b) the filtered PS-S modes.*

diverges from the head waves. This angle of appearance is dependent on the ratio between the S-wave velocity and the sound speed of the fluid. Higher ratios result in lower angle of appearance. This is mainly the case in soft unconsolidated sediments.

The non-geometric behavior of the P*S is potentially interesting for the seismic method in shallow marine environments because these specific modes can be treated as shear-source generated S-waves and their apparent velocity is directly related to the S-wave velocity in the subsurface. Mapping the wavefield in the parabolic Radon domain enables the separation of these waves from the remaining arrivals.

Chapter 4

Converted waves in a shallow marine environment: Experimental and modelling studies[2]

4.1 Introduction

Shear-wave velocity (c_s) provides important information for the characterization of the shallow marine subsurface. c_s differs from P-wave velocity (c_p) because of the insensitivity of c_s to the pore fluids and hence strong correlation with lithology variations (Gregory, 1976; Hamilton, 1976). From in-situ and core measurements of the upper tens of meters of marine sediments, many authors (e.g., Ewing *et al.*, 1992; Theilen & Pecher, 1991; Ayres & Theilen, 1999) reported that c_s increases rapidly with depth whereas c_p remains nearly constant. The availability of both P- and S-wave information allows the estimation of lithological properties such as porosity and grain size through empirical relations (Domenico, 1984).

Geotechnical studies benefit also from the retrieval of c_s in marine sediments. This is because physical properties, such as shear strength, can be correlated to c_s and used for estimation of seafloor stability, geohazard assessment and many other engineering purposes (Kugler *et al.*, 2007). Furthermore, obtaining accurate c_s models of the shallow subsurface is advantageous for the processing of multi-component seismic data (e.g., wavefield decomposition, static correction) and the imaging of targets below shallow gas pockets (Granli *et al.*, 1999).

Various seismic methods can be employed to infer c_s models of shallow marine sediments. These methods differ primarily in the type of waves acquired. In 1984, Kiel University developed a seabed air-gun source which is capable of generating horizontal shear stress (Gehrmann *et al.*, 1984). This source was used for refraction surveys and enabled the recording of SH-waves using horizontal geophones. Another similar shear-wave source with dual air-gun drive was presented by Chmela (2003). This air-gun-type shear-wave source generates large amount of P and P-SV energy and a considerably limited amount of SH-wave energy. More recently the Norwegian Geotechnical Institute has developed a sea-bed coupled vibratory source which appears to generate pure SH-waves (Westerdahl *et al.*, 2004). This electro-hydraulic

[2]This chapter has been published as a journal paper in *Geophysics* (Allouche *et al.*, 2011), with minor changes made.

marine vibrator weighs 9 tons and the source frequency band is restricted to 2-45 Hz. One of the reasons that the sea-bed coupled shear-wave sources have not yet seen wide application is due to the fact that they do not allow a fast acquisition, since both source and receiver are placed at the water bottom.

To estimate the seismic properties of shallow marine sediments, Riedel & Theilen (2001) inverted the amplitude information of P-waves as a function of offset (AVO). The authors obtained good results for the P-wave velocity and density but concluded that the S-wave velocity is difficult to estimate. The uncertainties in the derived c_s values were attributed to the insensitivity of the P-wave reflection amplitude to the shear wave velocity in the environment of interest.

Another popular approach is to invert the dispersion curves of the Scholte wave (e.g., Caiti *et al.*, 1994; Ritzwoller & Levshin, 2002; Park *et al.*, 2005). These P-SV polarized waves, traveling along the water-bottom interface, are highly sensitive to the shear-wave velocity. The Scholte waves are generated by an air-gun source and recorded using a receiver array placed in the water or at the water bottom. The recorded modes are resolved and inverted to obtain c_s profiles.

The shear-wave velocity can also be determined from the converted waves i.e., waves converted from compressional to shear mode at the water bottom or at a subsurface reflector. In hydrocarbon exploration, these waves have been successfully used for many years (e.g., Stewart *et al.*, 2003). Our research has focused on this mode of shear-wave generation, but for shallow marine environments. Recent modelling studies have shown that the conversion coefficients of incident plane waves at the water bottom are very small. Furthermore, it became clear that waves converted once at a shallow reflector and recorded in the horizontal component are most likely to be observed only at the large offsets (Allouche *et al.*, 2008). In the present study, we investigate whether converted waves are observable in field data in a shallow marine environment. We shall present here the results of a multi-component seismic survey conducted by deploying a four-component (4-C) receiver array in a shallow water canal. The results of field data analyses and new modelling studies will then be discussed to establish the presence of two types of converted shear-waves in such a shallow water environment. Further, we shall present, for the first time, evidence of non-geometric events in the shallow marine data, which we interpret as shear waves. Finally, the excitation criteria for such waves at the proximity of the water-sediment interface will be discussed.

4.2 Field experiment

A high-resolution seismic survey was conducted in 2004 in a shallow water canal near the town of Ghent, Belgium. Two seismic lines were shot using various types of sources including an air gun, a water gun and a sparker. The source was towed at 1 m water depth and fired at a spacing of 10 m. The data were acquired using a 4-C water-bottom cable spread at a water depth of 2 m. The cable consisted of 12 receivers at 5 m spacing. A schematic of the field configuration is given in figure 4.1. The air-gun data were sampled at 0.25 ms and recorded for 2 seconds.

Due to the limited number of receivers, the processing and analysis of the

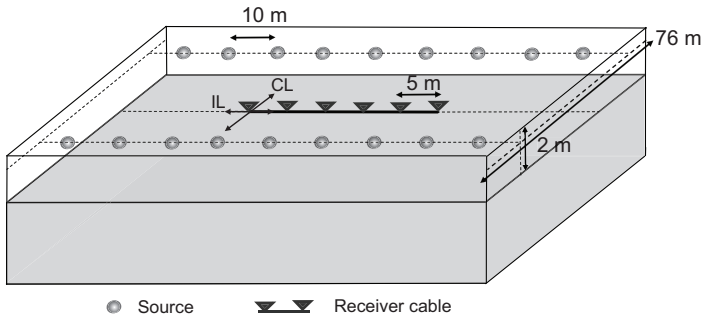

Figure 4.1: *Sketch of the field setting in the survey area. The arrows at the receiver denote the direction of the in-line component (IL) and cross-line component (CL).*

multi-component air-gun data were performed in the common-receiver domain. For each component, we have 12 receivers containing 107 traces each. The data redundancy and quality can be improved if we assume that the subsurface below the cable is laterally invariant. This assumption is quite acceptable for this well-known area. By sorting every two adjacent receiver gathers according to offset and then merging them, we obtained 6 new gathers each with a double number of sources and half the original shot spacing. To increase the signal-to-noise ratio, the obtained receiver gathers were normalized per trace and summed together, resulting finally in one gather. A bandpass-filter of 12-120 Hz was subsequently applied to the data. Figure 4.2 shows the enhancement of event coherency achieved for the hydrophone component after applying these processing steps.

4.3 Multi-component analysis

Although the absence of sonic logs and multi-component vertical seismic profiling (VSP) data prevent conclusive interpretations, the nature of the seismic events can still be revealed, based on their fundamental differences. Since S-waves are polarized in the direction perpendicular to the propagation, they are expected to be dominant at a different component than the P-waves. Depending on their raypath, S-waves have a relatively strong amplitude in data recorded on the horizontal components whereas P-waves are mainly observed on the vertical component. Due to the low velocity, S-waves appear at later times than the P waves, i.e. they have a low moveout velocity. Specifically for shallow unconsolidated sediments encountered in the study area, the c_p/c_s ratio was expected to be very high resulting in a drastic effect on the moveout velocity of the converted waves. In this analysis, we used the particle motion and the difference in moveout velocity as "attributes" to identify the recorded seismic events.

The processed common-receiver gathers corresponding to each component are shown in figure 4.3. A few distinctive features consistently observed in the data, are marked in these common-receiver gathers. The high-frequency early arrivals,

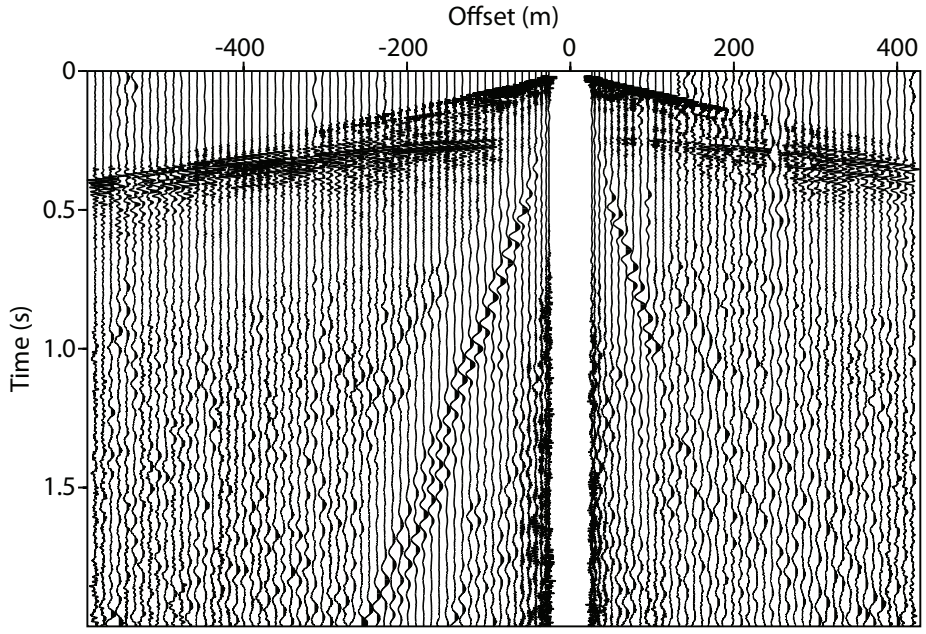

(a)

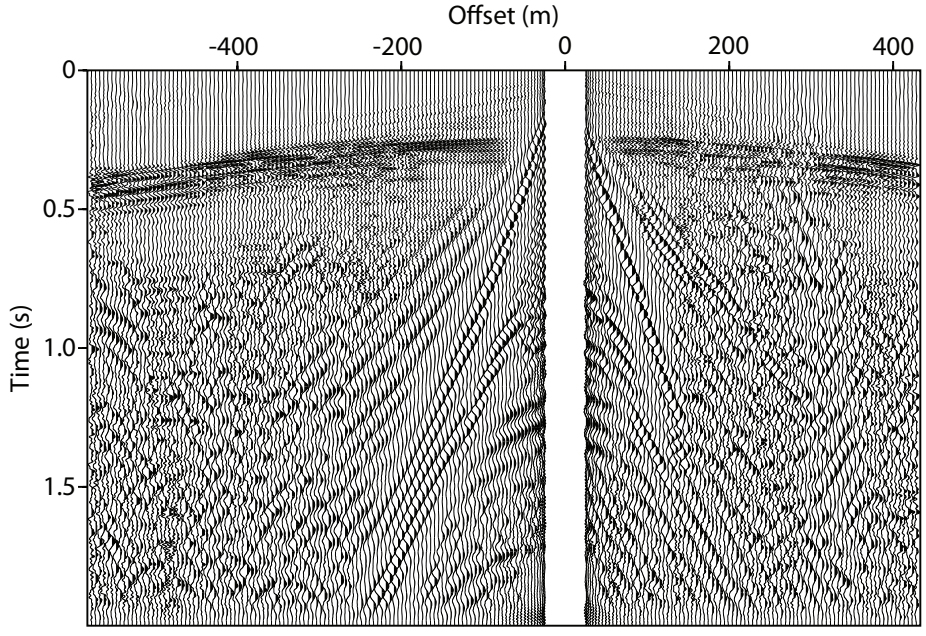

(b)

Figure 4.2: *Common-receiver gather acquired using an air gun and recorded on the pressure component.(a) Raw data, and (b) the data obtained after doubling the spatial sampling and applying automatic gain control (AGC) with a time window of 0.4 s.*

present in all components but significantly strong on the pressure measurement (hydrophone), are P-wave reflections. The dispersive events, also dominating in all components, are interface waves traveling along the water-sediment boundary. In addition to these arrivals, three other types of events draw our attention. These are highlighted by frames of three different colors in figure 4.3, and are analyzed in the following paragraphs taking into account their particle motion and moveout velocity.

4.3.1 Particle motion

The polarization direction is indicative of the types of event involved, therefore it is often used as a tool for event discrimination. Before computing the particle motion of the selected events in the data, we first had to correct for the cross-line offset between the shot line and the receiver array. Knowing the orientation of the geophone cable from the field geometry (see figure 4.1), we rotated the horizontal components through a given angle for each shot point so that the new axes lie along the radial and transverse directions. Figure 4.4 shows an enlarged part of the rotated components and the pressure component containing the distinctive arrivals with their particle motion. These arrivals are highlighted with the same color as their corresponding frames in figure 4.3. Evaluation of the particle motion using the radial and vertical components shows that all the highlighted events are polarized in the horizontal plane. We notice also that the events enclosed in the blue frame in figure 4.3 still have energy present in the transverse component after the rotation.

4.3.2 Moveout velocity

In-situ measurement of shallow marine sediments has shown that c_p/c_s ratios can be very high in the upper few tens of meters. The values can range from 6 for water-saturated sands to 13 or even higher for silty clays (Hamilton, 1979). This is expected to have a strong effect on the appearance of the converted events in the data. In figure 4.4, we indicate the moveout velocities of the highlighted events. The hyperbolic event with the red dashed line has a moveout velocity of 145 m/s (figure 4.4(c)). This value is unrealistically low for a wave converting geometrically from P to S at any interface, which suggests that this event has solely traveled as a shear wave in the sediment. The event marked by the blue dashed line has a velocity of 1380 m/s and a relatively small delay in time compared to the P-waves (figure 4.4(a)). This implies that they have traveled mainly as a P-wave before converting at a reflector to an S-wave. The last reflection shown by the green dashed line arrives later and has a lower moveout velocity (figure 4.4(a)) which may indicate that they have traveled an important part of their path as an S-wave. Therefore, this arrival can be interpreted as a P-wave converted at the water bottom to an S-mode. It is also possible that this arrival includes other refracted events which may coincide with the interpreted converted wave at small range.

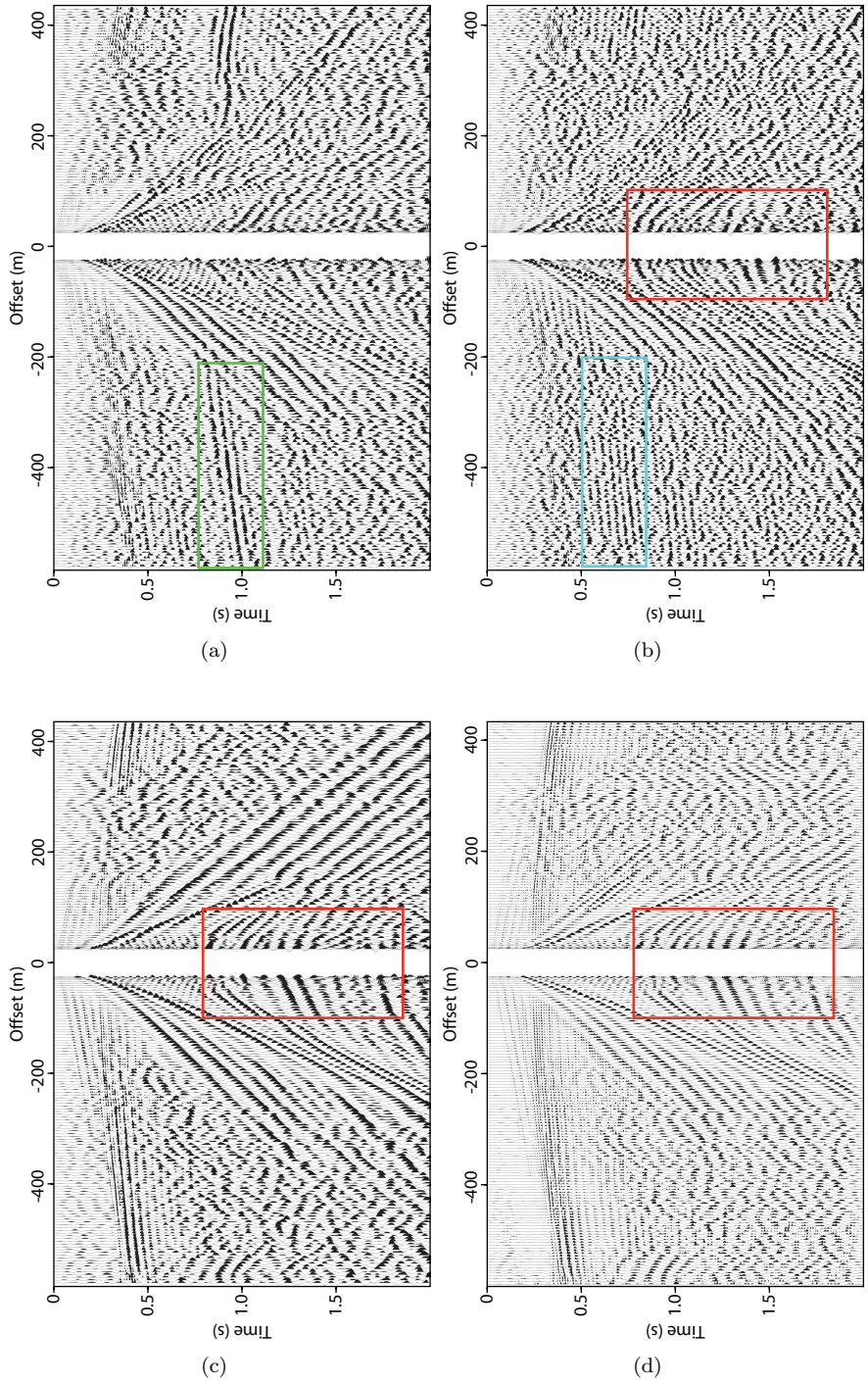

Figure 4.3: *Common-receiver gathers recorded on: (a) in-line component, (b) cross-line component, (c) vertical component and (d) pressure component. Frames in three different colors are used to highlight the distinctive events.*

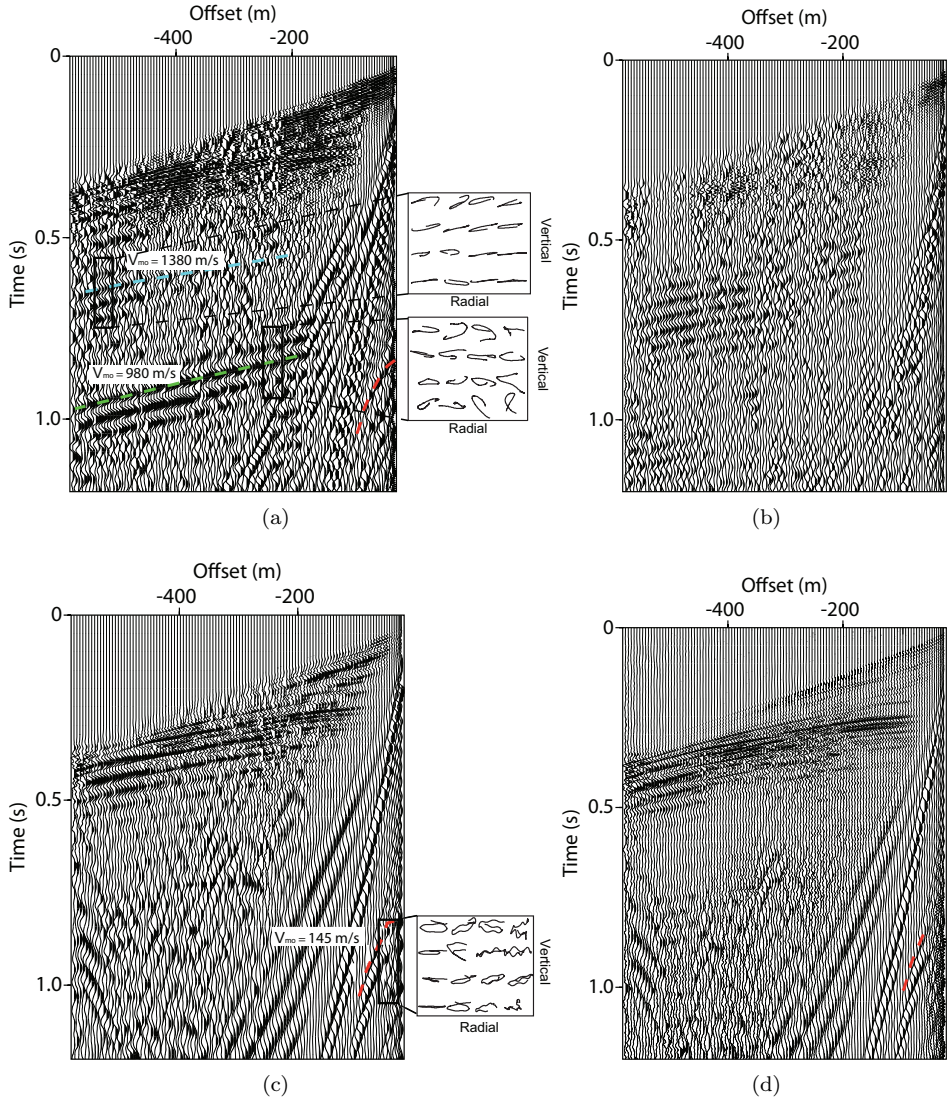

Figure 4.4: *Common-receiver gathers after rotation.(a) Radial component, (b) transverse component, (c) vertical component and (d) pressure component. The moveout velocity and the particle motion of the marked events are included. The black frames indicate the size of the window used to compute the particle motion.*

4.4 Modelling study

To better understand the nature of the distinctive events observed in the field data and to investigate whether shear waves have been excited directly by an air gun or not, we conducted a modelling study. We have chosen a simple 3-layer model to

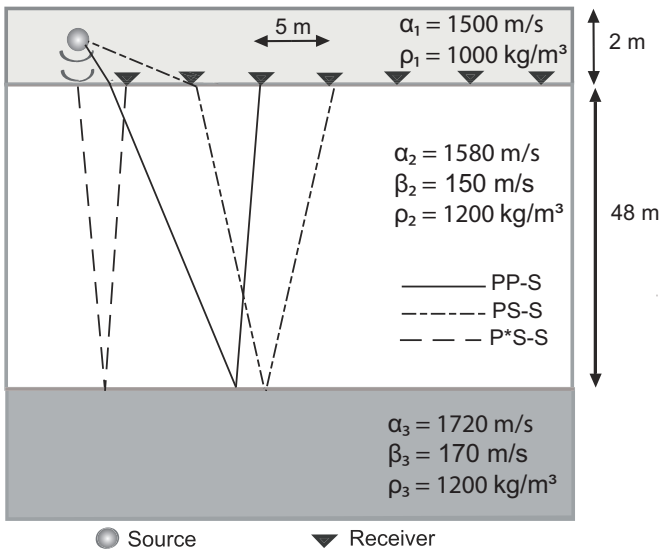

Figure 4.5: *Sketch of the model used to generate the synthetic data. The travelpaths of the converted modes (PP-S, PS-S and P*S-S) are depicted.*

avoid unnecessary complicated responses which may obstruct our understanding. The model consists of a water layer overlying two sediment layers with P-wave velocities equal to 1580 m/s and 1720 m/s, respectively (figure 4.5). The thickness of the layers and the velocity values are obtained from a velocity analysis performed on the hydrophone component of the field data. Furthermore, we assumed a change of density from 1000 kg/m^3 in the water to 1200 kg/m^3 in the sediments. Since we do not have any constraints on the S-wave velocity, we assumed a c_p/c_s ratio of 10 which is realistic for the shallow, unconsolidated sediments encountered in the survey area. The dominant frequency of the source wavelet is 80 Hz, as was estimated from the direct wave in the field data. The acquisition parameters in our modelling are kept similar to the field experiment. To compute the seismic response, we used a semi-analytical algorithm developed to solve the wave equation for horizontally stratified, laterally homogeneous media (Schmidt & Tango, 1986). This software package is known as Oases (Schmidt, 1988).

Our modeled response is compared with the field data in figure 4.6. We notice some distinct similarities. For instance, the synthetic data show that the reflection marked with the blue dashed line is a P-wave converted to S at a reflector (PP-S), whereas the one indicated by the green dashed line is converted at the water bottom (PS-S). The PP-S arrival is the mode of conversion typically used at the exploration scale. Note that the PP-S mode has the same traveltime as the PS-P, but only in the case of horizontally layered media. At small offsets, the arrival identified as PS-S is interfering with two other refracted modes. The travelpaths and traveltimes of these refracted waves are discussed in Appendix B.

The low-frequency hyperbolic event arriving at time 0.65 s can be correlated

with the reflection, marked by the red dashed line in the field data in figures 4.4 and 4.6. This event is asymptotic to the Scholte wave and has the traveltime of an S-wave reflection as if it has been generated at the water bottom. The longer traveltime of this reflection in the field data suggests in reality a lower average S-wave velocity than the assumed 150 m/s in the upper marine sediment. As explained in Appendix B, the observed reflection clearly has a different moveout from what is expected for the S-wave converted at the water bottom according to Snell's law. The excitation of this non-geometric shear-wave reflection (P*S-S, we use '*' to denote the non-geometric travelpath in water) is source-coupled as it was not observed in the water-gun data nor in the sparker data. At near offsets, the P*S-S reflection has the same traveltime as the PS-S arrival. As offset increases, the moveout of the non-geometric shear-wave reflection diverges from that of the PS-S arrival. The excitation of this particular shear wave will be discussed in more detail in the following section.

Another remarkable observation is the presence of these slow non-geometric waves in the pressure component of the field and synthetic data. This shows that these shear waves are converted to P modes at the water-bottom interface. In contrast with the other converted modes (PS-S, PP-S and PS-P), this S-P conversion is significant since these waves are well visible in the hydrophone recording (see figures 4.6(e) and 4.6(f)).

4.5 Excitation of shear waves by source water-bottom coupled system

The low-frequency reflected events propagating with an S-wave velocity were only visible in the air-gun data. In figure 4.7, a common-receiver gather acquired using an air gun is compared with one generated by a water gun. The two sources differ primarily in frequency content, with the air gun having a lower dominant frequency. Since the field configuration was kept the same during the survey, the excitation of the non-geometric shear-wave seems to be related to near-field effects.

In order to understand this excitation, it is sufficient to consider the transmission across a fluid-solid contact with the same seismic properties as the studied area. The interaction of the incident fluid wave with the water-bottom interface is determined by the ratio between the source height (h) and the dominant wavelength (λ). A large ratio h/λ implies a far-field condition. The incident wave can then be assumed to be planar and the energy partitioning to be governed by the Zoeppritz equations (Zoeppritz, 1919). However, the situation becomes different when the ratio is less than 1 with the wavelength exceeding the height of the source from the water-sediment interface. The incident spherical wave will then interact with the water bottom and will give rise to shear waves, Scholte waves and head waves, as discussed in Chapter 3. The snapshot images (cross-sections) of particle velocity, computed for both situations using a finite-difference algorithm, are illustrated in figure 4.8. The horizontal particle velocity computed for receivers at depth is shown in the same figure. The non-geometric PS-wave is observed only in the near-field case. It is the arrival diverging from the geometric PS-wave at a certain offset.

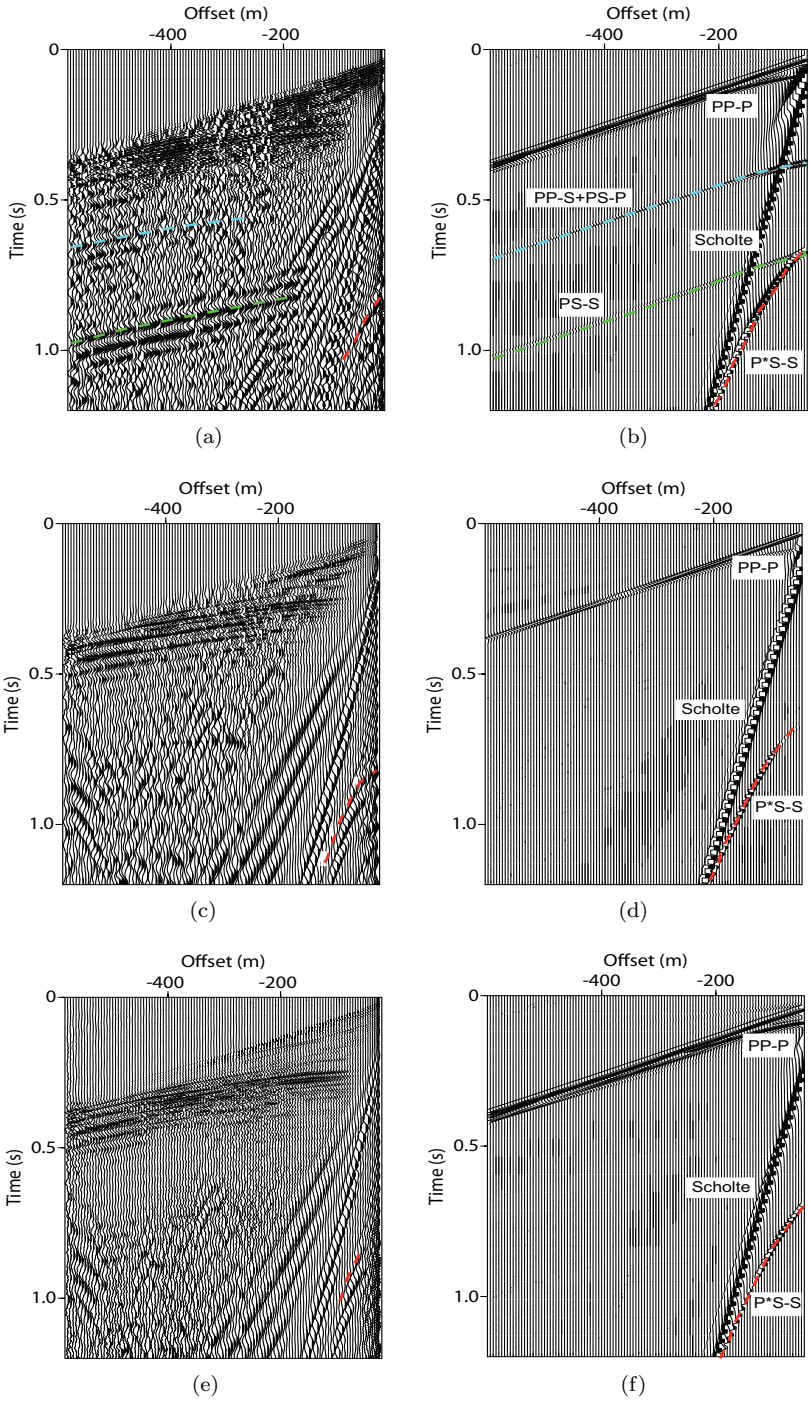

Figure 4.6: *Comparison between field and synthetic data. Radial component of the field data (a) and synthetic data (b). Vertical component of the field data (c) and the synthetic data (d). The pressure component of the field data (e) and synthetic data (f). The seismic arrivals are identified and labeled on the synthetic data.*

The near-field condition is met in case of our air gun which has a h/λ ratio of nearly 1/20. To investigate the dependence of the non-geometric shear-wave (P*S) amplitude on the distance of the source from the water bottom, we have modeled the transmission response for different h/λ ratios. To facilitate the comparison between the different transmission responses, we have used the same input wavelet with a dominant frequency of 100 Hz and varied the h/λ ratio by changing only the source height with respect to the fluid-solid interface. The results are shown in figure 4.9 for two receiver positions at a horizontal offset of 5 and 50 m and at 20 m depth below the interface. At the near-offset receiver position, the geometric and non-geometric PS-waves are interfering and their amplitude is significant in the horizontal component when the ratio is at least 1/4 (see figures 4.9(a) and 4.9(b)). However, the vertical component becomes more important at larger offsets but only if the wavelength is 8 times larger than the source height (see figures 4.9(c) and 4.9(d)). In the presented field data (see figure 4.6), the non-geometric PS-waves are well visible in the vertical component but they showed a horizontal particle motion in the selected near-offset traces. At far offsets, these waves are interfering with the interface waves.

As it was shown in Chapter 3, an interesting property of these waves is that they appear to be originating at a point on the interface directly below the source. This point acts as a generator from which the waves propagate with the S-wave speed of the sediments. At small offsets, the non-geometric S-wave is not visible. However, as the distance from the source becomes larger, the relatively fast PS-waves, because of their increasing travelpath through water, arrive separately from the P*S-waves. This phenomenon is illustrated further in figure 4.10. Here we have computed the transmission response at a vertically placed receiver array for $h/\lambda = 1/8$ and $h/\lambda = 2$. The receivers are located 50 m away from the source and at depths between 5 and 100 m. For $h/\lambda = 1/8$, the P*S-wave, dominant in both the horizontal and vertical component, is slightly delayed compared to the PS-wave at the deepest receiver. This delay in traveltime grows with decreasing receiver depth.

Furthermore, it can be noticed from figure 4.11 that the dominant frequency of the PS-wave is higher than that of the transmitted P-wave for a h/λ ratio of 1/8 and is similar to it for a h/λ ratio of 2. However, the dominant frequency of the non-geometric shear-wave is much smaller compared to the P-wave. This can be explained by the fact that a source wavelet is composed of a broad range of frequencies. The high frequencies are in the far-field when they approach the water-bottom contact giving rise to the PS-wave, whereas the low frequencies interact in the near-field generating two additional types of converted waves, namely the P*S-wave and the PS head-wave (a wavefront propagating with the S-wave velocity in the solid and with the P-wave velocity along the water bottom, see figure 4.8). For that, we can conclude that the interaction with the water bottom has a frequency filtering effect. As a consequence, the arrival identified as a PS-wave on the synthetic data is in fact a superposition of a geometrically converted wave and a head wave.

In global seismology, non-geometric shear-wave arrivals have been extensively studied in theory (e.g., Hron & Mikhailenko, 1980; Daley & Hron, 1983a,b, 1988) but hardly observed in field data (Gutowski *et al.*, 1984). These non-geometric

events are interpreted to be the result of interaction of evanescent waves with a plane interface (Hron & Mikhailenko, 1981). These evanescent waves with the real part of the horizontal slowness p lying in the range $1/c_p < p < 1/c_s$ are taken into account in the Sommerfeld integral representation of the spherical wavefront radiated by a point source (Aki & Richards, 2002).

4.6 Discussion

In the presented field data, two types of P to S mode conversion have been identified, namely, waves converted at the water bottom and waves converted at a reflector. The waves converted at a reflector are poorly visible and less continuous. Large offsets appear to be more favorable to acquire these waves. However, the waves converted at the water bottom are clearly observable over a wide offset range. The interpretation of these two types of conversion is simplified by their low moveout velocity and linear horizontal particle motion.

The most interesting aspect of our field data is the observation of non-geometric PS-waves in the vertical and horizontal components as well as in the pressure component. These waves have only been identified in the low-frequency air-gun data, implying that this type of conversion occurs when the incident wavefield interacts with the water bottom in the near-field. The existence of these converted modes is successfully verified by a modelling study where we considered the coupling effect between the source and water bottom for an elastic, isotropic, homogeneous half-space. Effects such as interaction of the source with the free surface, non-linear deformation in the sediments and attenuation on the excitation of P*S-waves, still need to be studied.

The non-geometric waves behave as if they were generated by a shear source located on the water bottom. Therefore, they can be suitable for the determination of c_s in the sediments. In practice, acquiring this type of waves will require placing a source, with low frequency content, close to the water bottom. This seems contradicting to what is common in shallow seismics where the focus is usually on the increase of resolution by including high frequencies. However, due to the effect of high c_p/c_s ratio of the sediments on the wavelength, the resolution is not deteriorated when non-geometric converted waves are used. The resolution can even be better if the c_p/c_s ratio is very high as in the case of shallow unconsolidated marine sediments.

However, the acquisition of the P*S-waves will be challenging due to several reasons: 1) these waves are generated only when the wavelength is at least 4 times larger than the source height; 2) they have a narrow optimum offset window since they are observable at small offsets and are asymptotic to the strong interface waves; and 3) much denser spatial sampling is needed due to their low velocity. Hence, proper tuning of field parameters is essential to detect these waves.

4.7 Conclusions

The data set presented in this study demonstrates the feasibility of acquiring P to S converted waves in a shallow marine environment characterized by a high c_p/c_s ratio. The specific field setting at our survey area provided us new insights on how to improve the poor P to S conversion at the water bottom and helped us discover a new non-geometric S-wave arrival.

By comparing field data with modelling results, we have shown the presence of waves converted at the water bottom as well as at a subsurface reflector. The large delays in traveltimes and the linear horizontal motion associated with these waves simplify their interpretation in field data.

Furthermore, we discovered that non-geometric shear-waves are excited when the dominant wavelength of the source is much larger than the source height with respect to the water bottom. The amplitude of these waves decreases as the distance between source and water bottom is increased. Kinematically, these waves behave as if they are excited by a shear source located at the water bottom. These waves can be useful for determination of c_s profiles in shallow marine sediments.

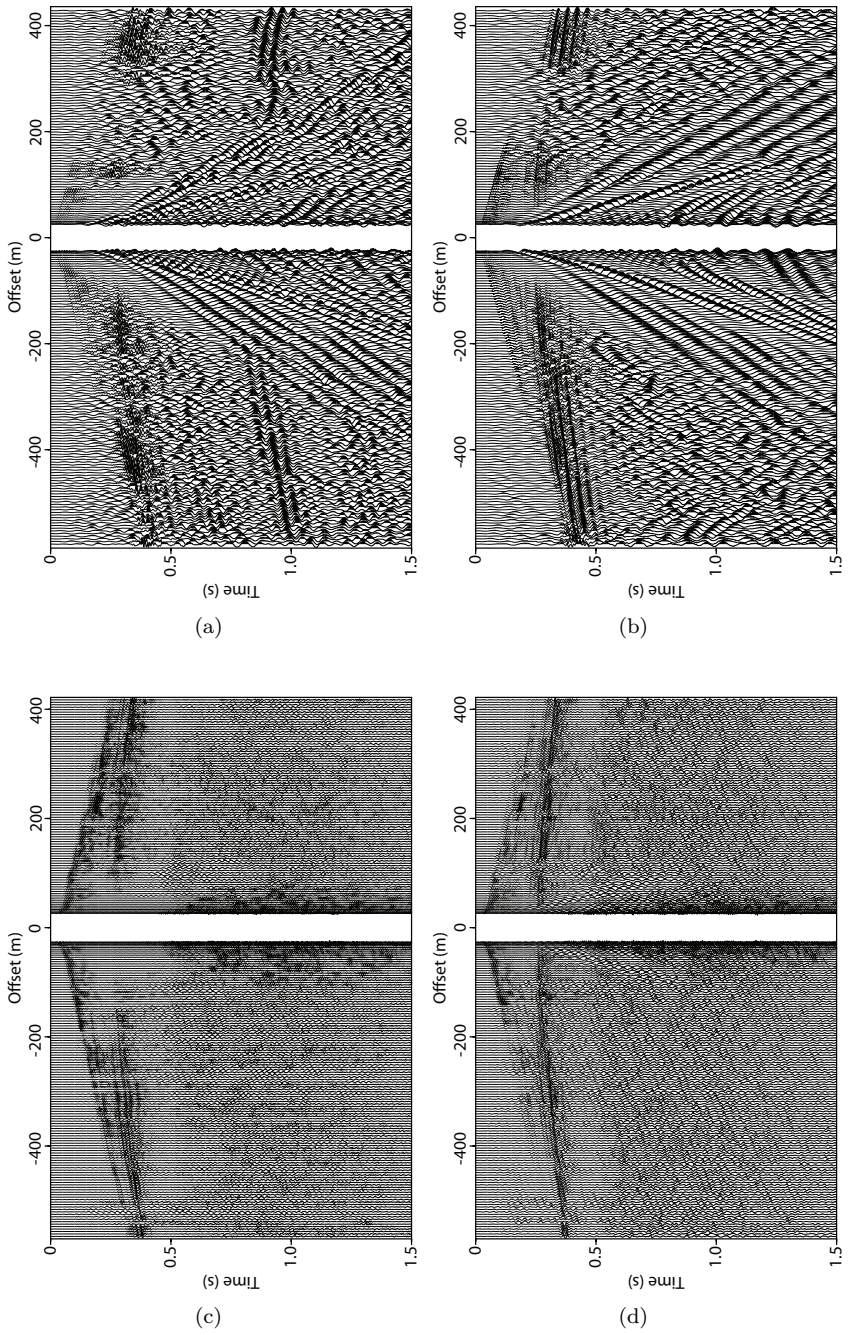

Figure 4.7: *Comparison between common-receiver gathers recorded with an air-gun source and a water-gun source. Horizontal component (a) and vertical component (b) of the air-gun data. Horizontal component (c) and vertical component (d) of the water-gun data.*

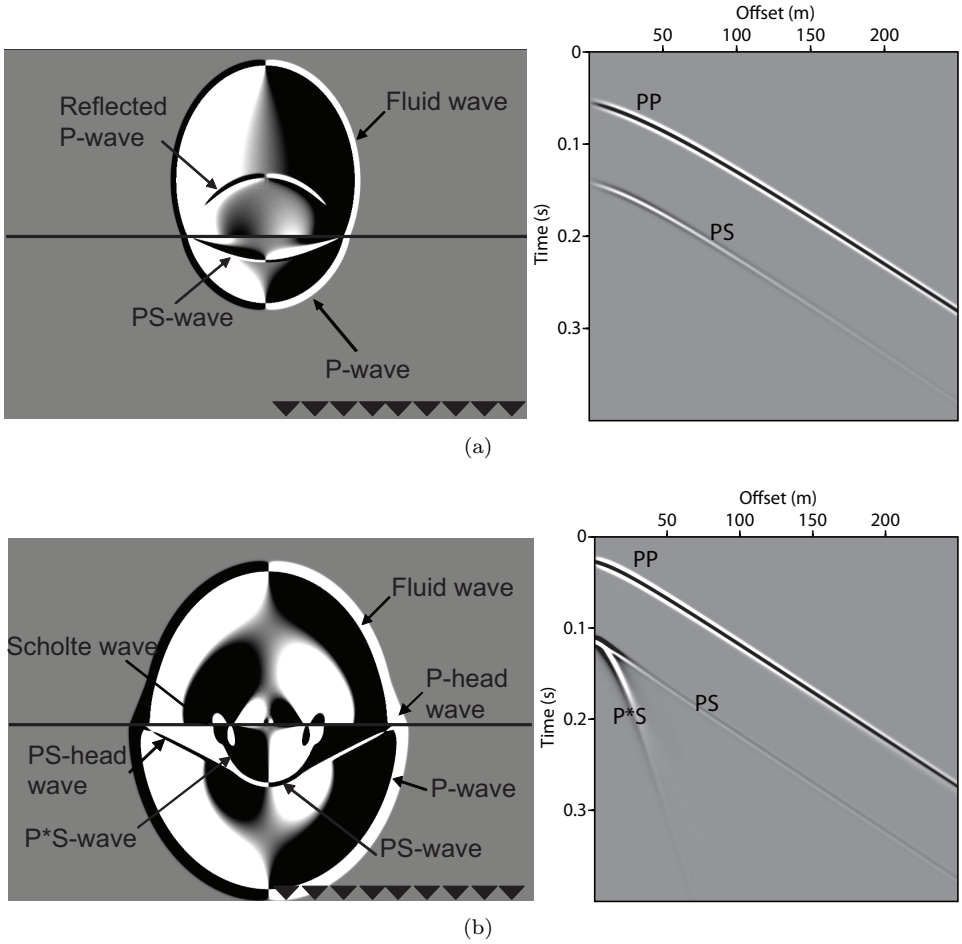

Figure 4.8: *The horizontal particle velocity generated by a source in the fluid and computed for a fluid-solid configuration in (a) far-field condition ($\lambda << h$) and (b) near-field condition ($\lambda >> h$). The response is computed for receivers buried in the solid, denoted by black triangles in the snapshot (left).*

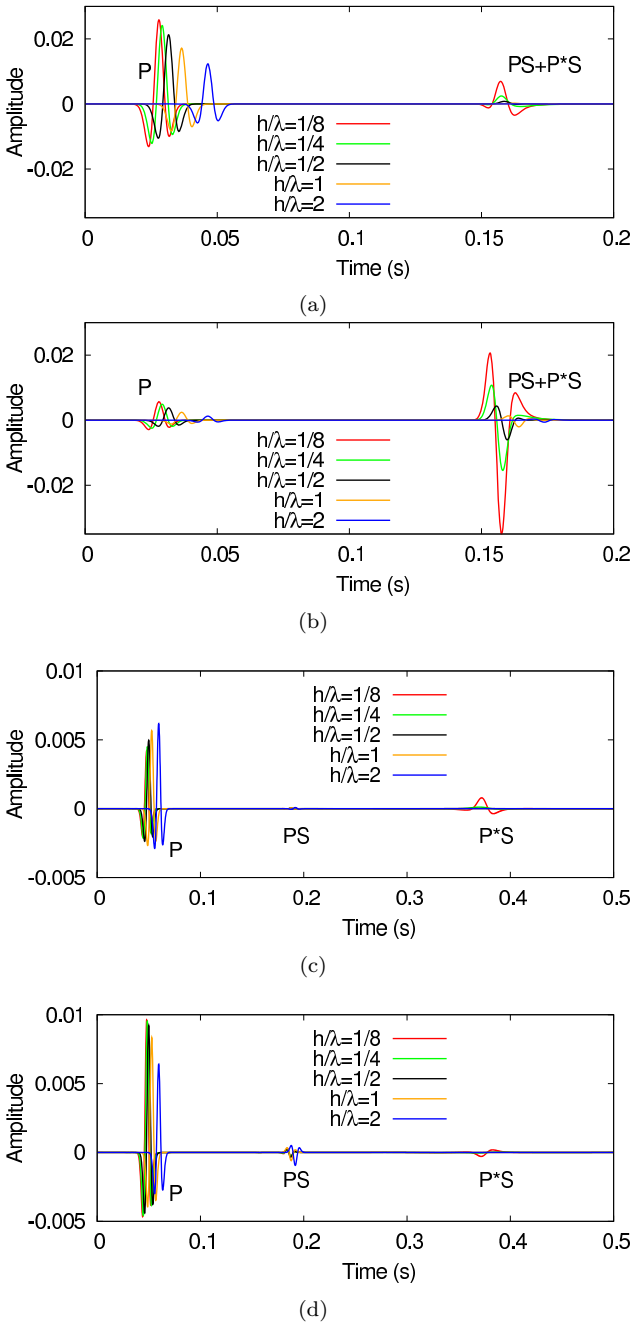

Figure 4.9: *Excitability of the non-geometric S-wave for different h/λ ratios. The horizontal (a) and vertical (b) particle velocity recorded at a receiver located 5 m away from the source and 20 m below the water-bottom interface. The horizontal (c) and vertical (d) particle velocity recorded at a receiver located 50 m away from the source and 20 m below the water-bottom interface.*

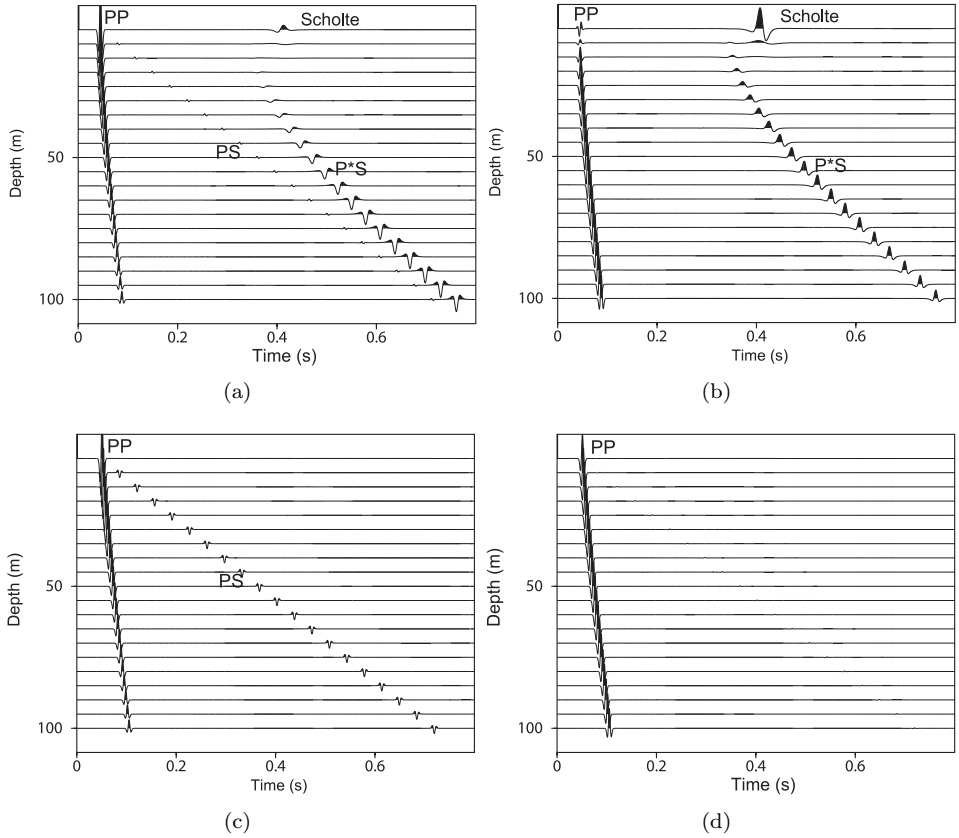

Figure 4.10: *The particle velocity computed for two h/λ ratios. The receivers have an offset of 50 m and are located at depths between 5 and 100 m below the interface. Particle velocity for $h/\lambda = 1/8$ in (a) horizontal and (b) vertical direction. Particle velocity for $h/\lambda = 2$ in (c) horizontal and (d) vertical direction.*

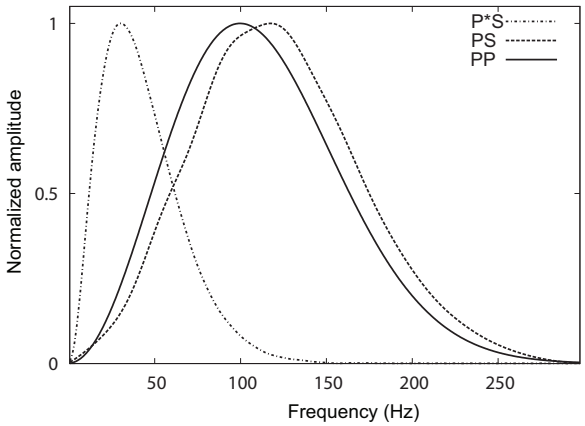

(a)

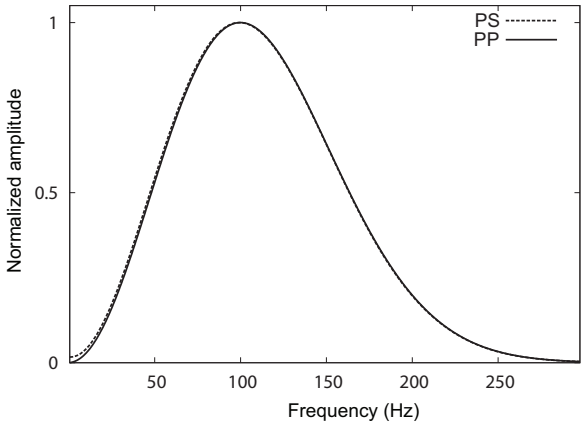

(b)

Figure 4.11: *Frequency spectrum of the separate events shown in figure 4.10. (a) Frequency spectrum of PP, PS and P*S recorded in the horizontal component at 50 m depth for $h/\lambda = 1/8$, and (b) frequency spectrum of PP and PS recorded in the horizontal component at 50 m depth for $h/\lambda = 2$. The amplitude of the frequency spectrum is normalized.*

Appendix B: Kinematics of geometric and non-geometric PS-S reflections

The geometric PS-S reflection is converted at the water bottom according to Snell's law and is therefore explained by the classical ray theory. However, the non-geometric PS-S is evanescent in water and is converted to a propagating mode at the water-bottom interface. Therefore, they appear to be originating at the projection point of the source on this interface. In this appendix, we demonstrate the difference in the kinematic behavior of the geometric and non-geometric PS-S-waves by deriving their traveltime expressions. Figure 4.12 displays the travelpaths of the reflections and the geometric variables used for the derivation. Furthermore, we show that the geometric PS-S is interfering with two refracted modes in the offset range discussed in this chapter.

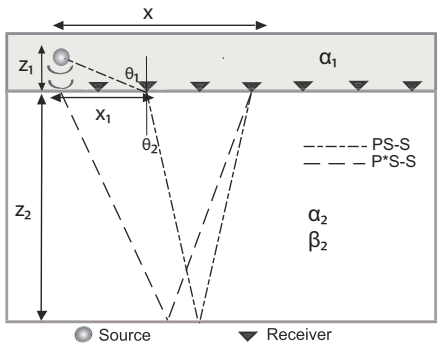

Figure 4.12: *Sketch of PS-S and P*S-S travelpaths. Definitions of the geometric variables used in the equations are also included.*

The traveltime t_{pss} for the geometric converted mode PS-S as a function of offset x is:

$$t_{pss} = \frac{\sqrt{x_1^2 + z_1^2}}{\alpha_1} + \frac{\sqrt{(x - x_1)^2 + 4z_2^2}}{\beta_2}. \tag{4.1}$$

The conversion point x_1 can be determined by rewriting Snell's law in terms of the geometric variables defined in figure 4.12:

$$\begin{aligned} \frac{\sin\theta_1}{\alpha_1} &= \frac{\sin\theta_2}{\beta_2}, \\ \frac{x_1}{\alpha_1\sqrt{x_1^2 + z_1^2}} &= \frac{x - x_1}{\beta_2\sqrt{(x - x_1)^2 + 4z_2^2}}. \end{aligned} \tag{4.2}$$

To solve for x_1, Eq. 4.2 is rearranged into the quartic equation of the form

$$x_1^4 + ax_1^3 + bx_1^2 + cx_1 + d = 0, \tag{4.3}$$

where

$$a = \frac{2x(\alpha_1^2 - \beta_2^2)}{\beta_2^2 - \alpha_1^2}, \tag{4.4}$$
$$b = \frac{\beta_1^2(x^2 + 4z_2^2) - \alpha_1^2(z_1^2 + x^2)}{\beta_2^2 - \alpha_1^2},$$
$$c = \frac{2\alpha_1^2 z_1^2 x}{\beta_2^2 - \alpha_1^2},$$
$$d = \frac{\alpha_1^2 z_1^2 x^2}{\beta_2^2 - \alpha_1^2}.$$

Four possible solutions to this fourth-order polynomial exist: two real and two complex. The general form of these solutions is given in details by Taylor (1989). The exact solution for x_1 is the real number ranging between $0 < x_1 < x$. This number can in turn be substituted into Eq. 4.1 to compute the traveltime of the PS-S mode.

The P*S-S wave appears to be originating at the fluid-solid interface, from where it propagates as a pure S-wave. Therefore, the traveltime of this arrival is simply

$$t_{p*ss} \approx \frac{\sqrt{(x^2 + 4z_2^2)}}{\beta_2}. \tag{4.5}$$

We computed the traveltimes of the two PS-S reflections for the model parameters used in the modelling study and compared these to the horizontal component of the synthetic data in figure 4.13. The difference in moveout between PS-S and P*S-S is caused by the conversion at the water bottom. For the PS-S, the moveout is determined by the sound speed in water and the shear-wave velocity in the sediments given by the two terms in Eq. 4.1. However, the moveout of the P*S-S is solely determined by the shear-wave velocity resulting in a very low apparent velocity.

In figure 4.13, it can also be noticed that the PS-S arrival is interfering with two other events at the offset range ($\sim$500 m) discussed in this chapter. These two events appeared to be refractions traveling along the paths indicated in figure 4.14. For completeness, we also derived their traveltime expressions.

The traveltime of the refraction propagating as a P-wave along the boundary separating the two sediment layers is given by

$$t_{psps} = \frac{x}{\alpha_3} + \frac{z_1 \cos\theta_{13}}{\alpha_1} + \frac{2z_2 \cos\theta_{23}}{\beta_2}, \tag{4.6}$$

where

$$\theta_{13} = \sin^{-1}(\alpha_1/\alpha_3) \tag{4.7}$$
$$\theta_{23} = \sin^{-1}(\beta_2/\alpha_3).$$

The non-geometric P*S-S is also refracted at the water-bottom interface. The traveltime of this refraction can be expressed by:

$$t_{p*ssp} = \frac{x}{\alpha_2} + \frac{2z_2 \cos\theta_{22}}{\beta_2}, \tag{4.8}$$

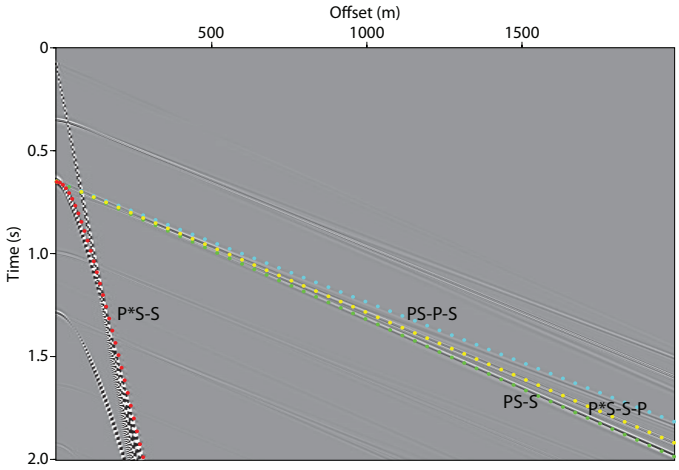

Figure 4.13: *The synthetic response is overlain by the traveltime curves of the reflected modes PS-S (green) and P*S-S (red) and the refracted modes PS-P-S (blue) and P*S-S-P (yellow). The direct arrival is muted.*

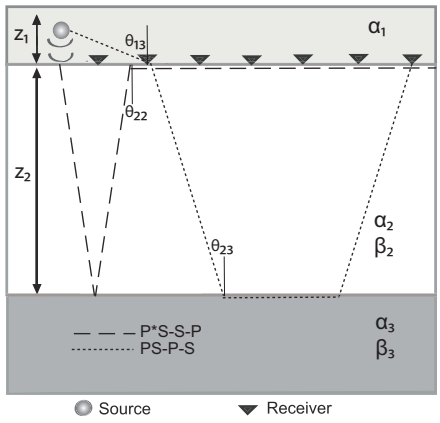

Figure 4.14: *Sketch of PS-S and P*S-S travelpaths. Definitions of the geometric variables used in the equations are also included.*

where

$$\theta_{22} = \sin^{-1}(\beta_2/\alpha_2). \tag{4.9}$$

The traveltime curves of the refracted waves are also included in figure 4.13. These arrivals are visible in the synthetic data, however, the PS-S reflection is considered more significant because only one mode of conversion is involved.

Chapter 5

Methodology for dense spatial sampling of multicomponent recording of converted waves[3]

5.1 Introduction

In shallow marine environment, high-resolution seismic surveys are conducted to solve various geological and engineering problems (e.g., Pulliam *et al.*, 1996; Marsset *et al.*, 1998; Pinson *et al.*, 2008). Although S-wave information is often necessary to solve these problems, the vast majority of the surveys are designed to acquire P-waves only. This is because S-wave information is generally retrieved from converted waves (Stewart *et al.*, 2003) and these are more difficult to record since they often require deploying the receivers on the seabed. Consequently, the acquisition of this type of waves becomes less efficient and hence more expensive and time consuming in comparison to the acquisition of P-waves.

Another major obstacle impeding a widespread use of converted waves is the dense spatial sampling required for the data analysis and processing. Depending on the depth of the target and the velocities encountered in the subsurface, the receiver intervals for P-waves are typically 2.0 to 10 m (e.g., Lucas, 1974; Chapman, 2004; Müller *et al.*, 2002) for dominant frequencies between 200 and 650 Hz. The high c_p/c_s ratio in shallow marine sediments imposes a decrease of the spatial interval for S-waves by about the same order. The c_p/c_s ratio near the seafloor varies between 2 in limestones and 13 in water saturated silts (Hamilton, 1979). Ayres & Theilen (1999) reported on c_p/c_s values larger than 30 for unconsolidated sediments found in the Barents Sea. Adequate spatial sampling of S-waves in these sediments requires a receiver interval of less than half a meter.

In marine settings, achieving an adequate spatial sampling is limited in practice by available equipment on the receiver side. Therefore, as in exploration seismology, most effort is made to reduce the shot spacing by minimizing the recording time length and the boat speed. However, to record the slow converted modes, the recording length needs rather to be increased. A further decrease of the boat speed is not sufficient to obtain the aimed shot spacing of less than half a meter. Then,

[3]This chapter has been published as a journal paper in *Geophysics* (Allouche *et al.*, 2010), with minor changes.

seismic surveying for S-wave information becomes practically not feasible.

In this chapter, we present a novel methodology developed to achieve properly sampled multicomponent data, suitable for converted-wave analysis and processing. In this method, we propose to obtain the required sampling interval on the shot side. This is done by shooting the same track multiple times and combining the different shot lines together. Inherent to this acquisition approach, the source and receiver positioning has to be very accurate for a successful combination of the different shot lines to a densely sampled one. Since the positioning errors involved in a typical survey are generally larger than the aimed sampling interval of a few tens of centimeters, we introduce an additional processing step to merge the lines together. For this purpose, we use a method based on crosscorrelation to correct for the positioning errors of the different shot lines with respect to one reference shot line. The effectiveness and the sensitivity of the crosscorrelation step will first be demonstrated using a synthetic data example before being applied to field data.

As in the case of P-wave surveys, the spacing in the combined shot line is variable and needs to be regularized to ensure adequate handling by processing algorithms. Many techniques related to particular transforms such as the Fourier transform and the parabolic Radon transform (e.g., Kabir & Verschuur, 1995; Duijndam *et al.*, 1999) were developed over the last decades to reconstruct missing traces. One of these techniques can be applied to the combined shot line to obtain dense and regular sampled data along the spatial direction. In the field example described in this chapter, we simply used the non-uniform Fourier transform for this purpose because large gaps present in the shot line resulted in numerical instability of the other methods and deteriorated the quality of the data.

5.2 Methodology for dense spatial sampling

5.2.1 Shooting multiple lines for the same track

To avoid spatial aliasing, the smallest apparent wavelength of interest in the horizontal direction, λ_{min} needs to be sampled at least twice. In turn, the smallest wavelength is determinded by the maximum source frequency of interest, f_{max}, and the smallest apparent velocity in the subsurface, c_{min}, as indicated in the relation

$$\Delta x \leqq \frac{\lambda_{min}}{2} = \frac{c_{min}}{2f_{max}}. \tag{5.1}$$

Typically in high-resolution seismics, sources with a frequency content above 100 Hz are used. In general for P-waves, the smallest velocity encountered in a marine environment is the velocity of sound in water. To record P-waves with a maximum frequency of 250 Hz and thus a minimum apparent wavelength of 6 m, the data have to be acquired with a spatial interval of at most 3 m. However, for an adequate spatial sampling of S-waves in unconsolidated sediments with a c_p/c_s ratio of at least 10, the spatial sampling needs to be in the order of 0.3 m. This value is very small and not feasible with the standard recording equipment for marine settings.

Consequently, the aimed spatial sampling has to be achieved in a different manner. Since the shots in marine acquisition can be fired much faster and are cheaper compared to land seismics, repeating a shot line multiple times is a logical step to obtain a better spatial coverage.

5.2.2 Combining multiple shot lines using crosscorrelation

The simple idea of acquiring multiple shot lines and combining them based on their relative positions is complicated by the measurement errors introduced during the survey. These errors are caused by uncertainties in the positioning system and variation of field conditions over time. After combining the shot lines, these errors may even exceed the distance between two adjacent shot points and result in discontinuities of events and degradation in the resolution of the data. This type of problem is often encountered in high-resolution seismics and is solved by inverting for more accurate source and receiver positions (He *et al.*, 2009). An inversion-based approach is not preferred in our case because the shot redundancy of the data requires repeating the computationally-intensive inversion for each shot position. Alternatively, we can correct for the errors using a crosscorrelation-based method.

Crosscorrelation-type of techniques have been used to estimate static shifts (Taner *et al.*, 1974), to quantify time-lapse effects (Hale, 2009) and to redatum wavefields (Schuster & Zhou, 2006). Here, we use crosscorrelation to fit the different shot lines within one reference shot line. Each trace from the remaining shot lines is crosscorrelated with a panel of traces from the reference line to estimate its new relative position. The basic idea and the sensitivity of the method are discussed below using a synthetic data example.

Synthetic data example

To explain the idea, we use a synthetic data set computed using a finite-difference algorithm for the model depicted in figure 5.1. The velocities in this model are typical for a shallow sea subsurface composed of soft sediment overlying dipping consolidated rocks. The water bottom is modeled as a rough interface at 20 m depth from the free surface. We computed the pressure for one receiver located on the water bottom and multiple sources located in the water, the shot spacing being 3.5 m. We generated another data set with shot positions shifted half the shot spacing and assigned erroneous random offset values to them. The crosscorrelation procedure is used to correct the offsets and merge these two data sets.

The procedure is explained in figure 5.2 for one trace. The erroneous offset value of this trace x_{er} is used initially to select a panel of traces from the reference data set which includes all the traces with offset values between $x_{er} - e_{max}$ and $x_{er} + e_{max}$, where e_{max} is the largest spatial error expected in the measurement. Subsequently, the erroneous trace is crosscorrelated with the panel and the result is shown on the right part of figure 5.2(a). The traces that have their maximum amplitude at the smallest positive and negative time lags are basically located adjacent to the erroneous trace. The new offset value of the erroneous trace x_{tr} can

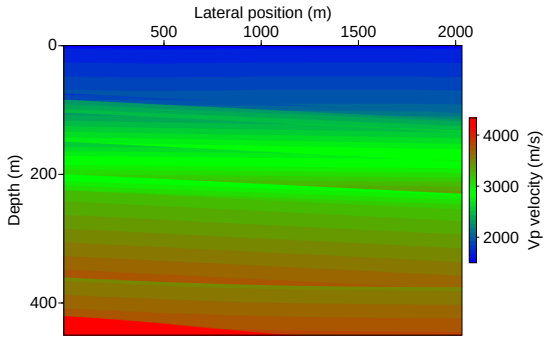

(a)

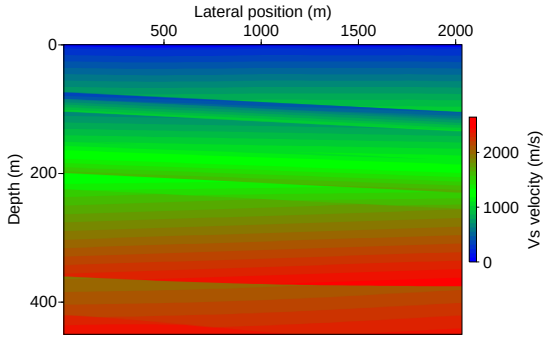

(b)

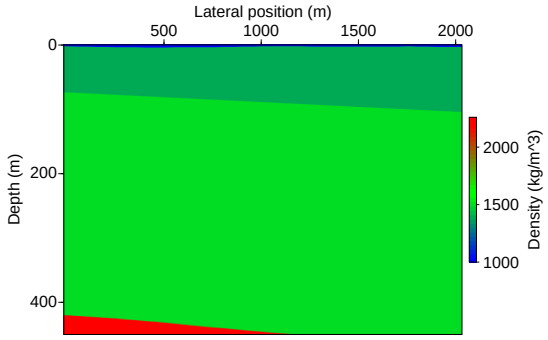

(c)

Figure 5.1: *Model used to compute synthetic data: a) P-wave velocities, b) S-wave velocities and c) densities.*

then be linearly interpolated from the values of its neighboring traces:

$$x_{tr} = x_1 + \frac{\Delta t_1}{\Delta t_1 + \Delta t_2}(x_2 - x_1), \tag{5.2}$$

where x_1 and x_2 are the offset values of the adjacent traces and Δt_1 and Δt_2 are their corresponding time lags from the output correlation panels. The newly computed offset value x_{tr} is then used to merge the trace into the panel. As shown in figure 5.2(b), this procedure is very effective since the trace is placed at the right position. We implemented the idea further by repeating the procedure for the remaining traces. When the crosscorrelation fails to correct for the offset, the trace is not merged in the reference line. The successfully combined result is compared to the reference data set in figure 5.3. It can be noticed that the combined data set is interpolated because it is composed of twice the number of shots compared to the reference data. The small differences between the two data sets, indicated by the black arrows, are the result of excluding the traces that were corrected by a value exceeding e_{max}.

Sensitivity of the method

The aim of the crosscorrelation step is to reduce the relative uncertainties in offsets introduced during the field acquisition by different factors. These errors are difficult to quantify and can vary from one shot position to another. The linear interpolation of offsets is correct for linear events like the direct wave, refracted waves and interface waves and is an approximation for hyperbolic-shaped reflections. This approximation may break down when the initial gap between the adjacent sources in the reference line is too large.

To test the sensitivity of the method to the initial source spacing, we generated four data sets with their corresponding reference common-receiver gathers. The source spacings of the reference data sets are 3, 4.5, 6 and 9 m. The offset values of the data are set to different values, by assigning random values to the traces with a maximum deviation of 4 m. The data sets are subsequently crosscorrelated with their corresponding reference shot gather and the offset values are corrected. The absolute errors in offset between the data set before and after the correction step for each source spacing are shown in figure 5.4.

The green lines in figure 5.4 indicate the initial errors which are comparable to the positioning errors introduced during the measurement whereas the solid red lines are the final errors after applying the crosscorrelation step. It can be noticed that the correction method using crosscorrelation effectively minimized the absolute errors independently from their initial values. Moreover, the method showed to be insensitive to the shot spacing of the reference line. This implies that the effectiveness of the crosscorrelation is mainly determined by the strong linear direct or refracted events.

Another factor which may affect the result of the crosscorrelation step is noise. Real data can be very noisy, particularly at far offsets, and the noise may have the same bandwidth as the data. We added incoherent Gaussian-distributed noise in the frequency range of 20-250 Hz to the generated reference data shown in figure 5.3(a)

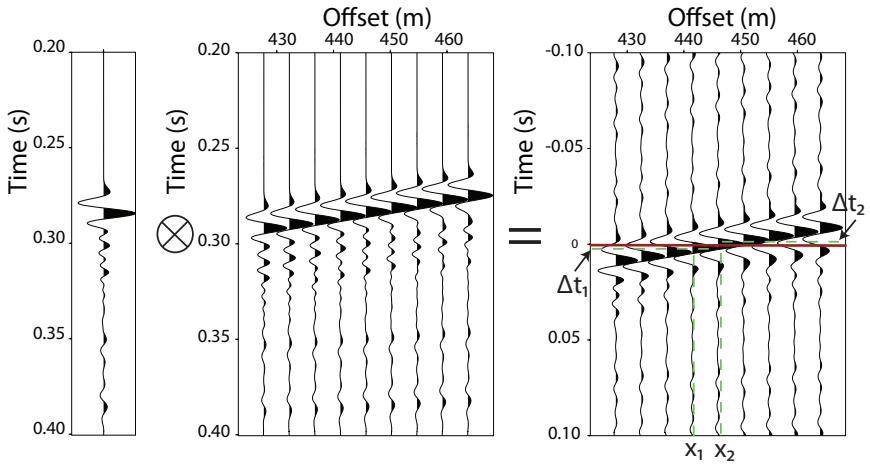

(a)

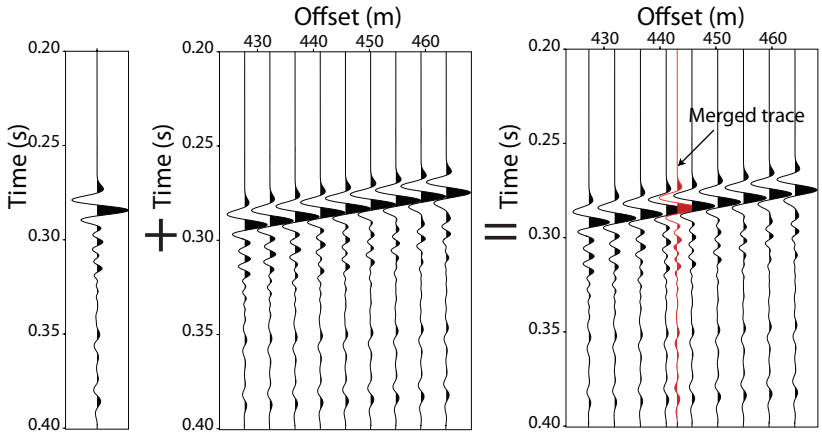

(b)

Figure 5.2: *Illustration of the offset-correction procedure for one trace using crosscorrelation. a) An arbitrary trace with an erroneous offset is crosscorrelated with a panel of traces from the reference line. b) The trace with the newly computed offset value (in red) is merged into the panel.*

and applied the crosscorrelation step again. Due to the presence of noise in the data, the number of the successfully merged traces is drastically reduced as can be noticed when figure 5.5(a) is compared to the noise-free data in figure 5.3(b). For many traces, the maximum crosscorrelation amplitude was affected by noise resulting in a wrong offset interpolation. Omitting these traces from the merged data set resulted in an irregular shot spacing and a ragged appearance of arrivals. In this condition, time gating the direct arrival and applying a bandpass filter

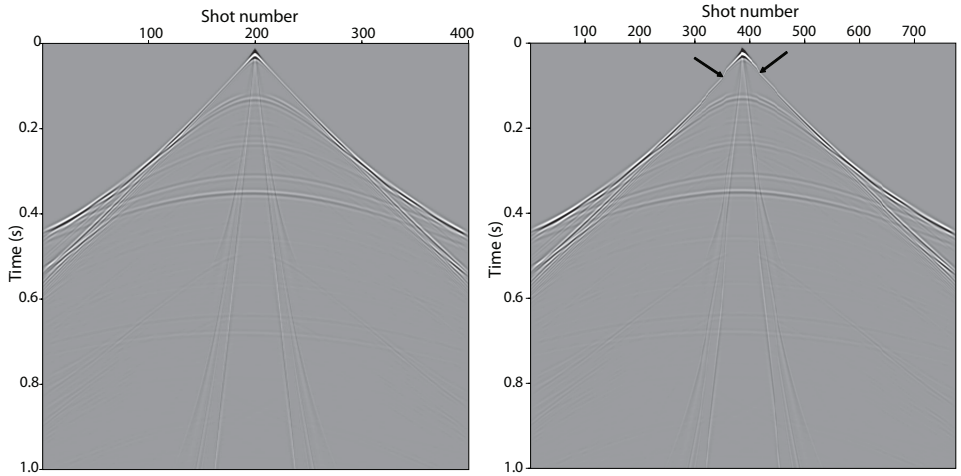

(a) (b)

Figure 5.3: *a) The reference common-receiver gather and b) the common-receiver gather combined using crosscorrelation. Note that the spatial sampling is doubled with hardly any degradation except for the locations indicated by the black arrows.*

before the crosscorrelation procedure are helpful tools to increase the number of the successfully merged traces as shown in figure 5.5(b).

5.3 Field experiment in the Danube River

5.3.1 Data acquisition

A high-resolution seismic survey was conducted on the Danube River in 2008 near the village of Kulcs, Hungary. The aim of the survey was to acquire properly sampled seismic data suitable for converted-wave processing. For this purpose, we adopted the methodology proposed above.

The survey area is located in a seismically active region south of Budapest. The shallow subsurface is composed of Miocene unconsolidated sand and shale sequences underlying young river sediments. Figure 5.6 shows the study area and the approximately 1-km-long seismic track shot using an air gun.

The data were recorded using a 4-C water-bottom cable consisting of 12 receivers with a spacing of 5 m. The cable was deployed on the riverbed at a depth of 3.5 m. A 20-cubic inch air gun was towed at a depth of 2 m and fired every 4 s. The data were digitized at a time-sampling interval of 0.250 ms with a recording length of 2 s. By firing the air gun only in the upstream direction, the boat speed was minimized to $\sim$1 m/s resulting in a shot spacing of $\sim$4 m. Given the frequency content of the source and the S-wave velocities expected in river sediments, we aimed at a spatial sampling interval of 0.3 m. To achieve this, we shot 14 times along the

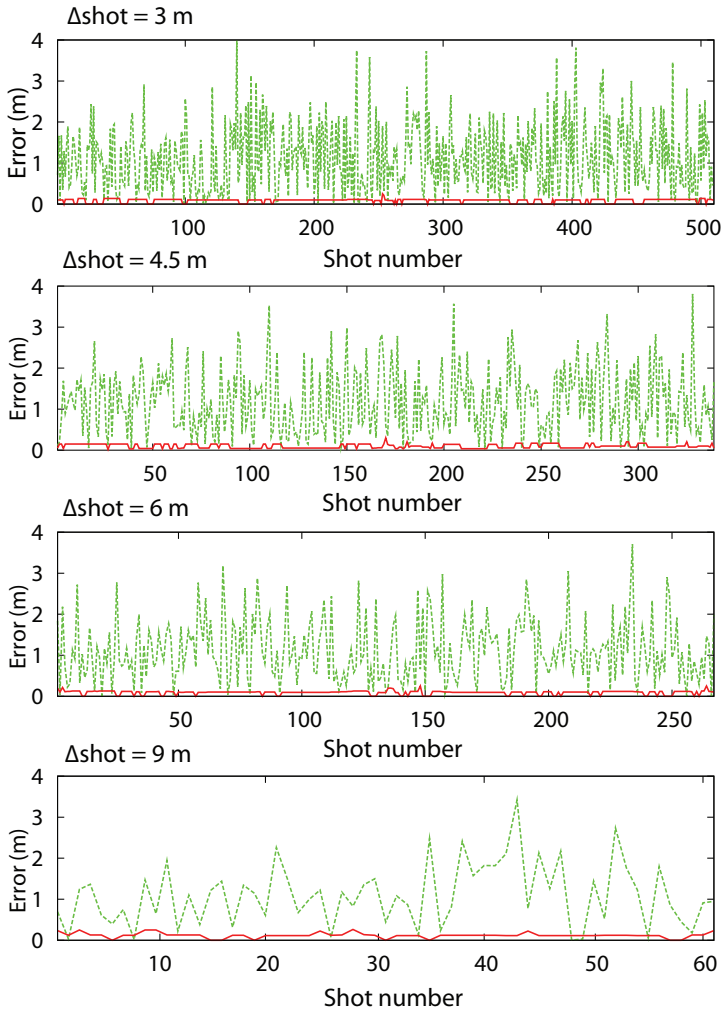

Figure 5.4: *Absolute errors in offset before (green dashed lines) and after (red solid lines) applying the correction step using crosscorrelation. Errors are computed for source spacings of 3, 4.5, 6 and 9 m.*

same track.

During the survey, positioning errors were introduced by different causes: (1) the positions of the receivers on the river bottom are not exactly known, (2) possible variation of the receiver positions with time because of the strong currents in the water, (3) the GPS system was towed 3 m behind the source for protection; also due to the currents in the water it was difficult to align them and (4) the inaccuracy of the used positioning systems. These errors impede a combination of the different shot lines without deteriorating the lateral resolution of the data.

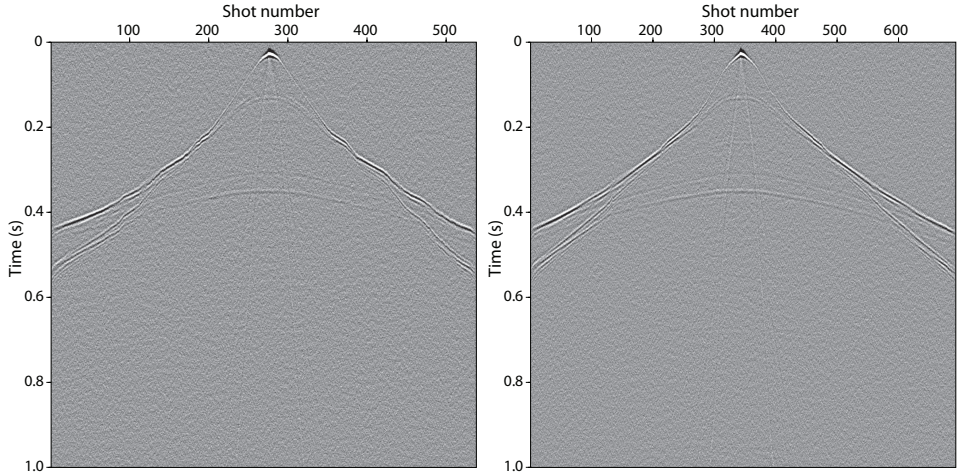

Figure 5.5: *Combined data sets after addition of Gaussian-distributed noise in the frequency range from 20 to 250 Hz. a) Only crosscorrelation is applied and b) crosscorrelation is preceded by time gating the direct arrival and bandpass filtering (30-120 Hz).*

In the methodology discussed above, the crosscorrelation step is applied to account for the variation of positioning errors between the shot lines by correcting their offset values with respect to one reference shot line. The offset values of the reference shot line are assumed to be correct since they are used for the offset interpolation. However, to be able to apply the crosscorrelation step to the field data, the positioning errors introduced during the field survey need to be corrected for one single shot line that we will use as a reference line.

While the error related to the source position is easily corrected, the uncertainty involved with the underwater receiver positions required a separate procedure to minimize it. In the processing flow, we first estimate the receiver positions using the direct arrival, before we use crosscorrelation to merge the shot lines together. The combined result will then be regularized using the non-uniform discrete Fourier transform and filtered to remove the low frequency interface waves strongly present in the data. All the processing steps are applied in the common-receiver gather domain.

5.3.2 Estimation of receiver positions using direct arrival

In the field, the first and last position of the receiver array were measured before its release into the water. However, from the near-offset traces, the uncertainties in receiver positions appeared to be unacceptably large and required correction before further processing could be applied. Assuming that the shot positions are correct, we make use of the direct wave, recorded as first arrival in the nearest offsets

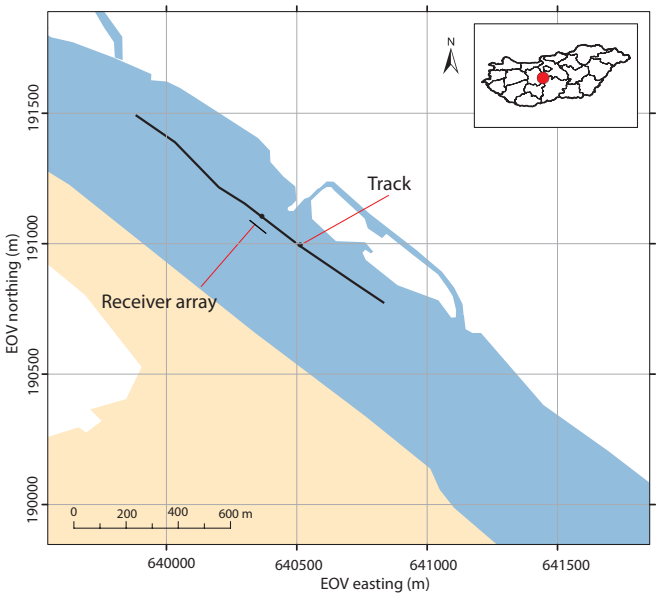

Figure 5.6: *Map of the survey area showing the track of the shot lines in Hungarian state plane-coordinates (EOV).*

to estimate the correct coordinates of each receiver. We account for the depth difference between source and receiver measured in the field and we apply normal-moveout (NMO) correction to the near-offset traces using the water velocity of 1500 m/s. The alignment of the direct wave in each common-receiver gather after NMO is an indication of the accuracy of the coordinate. The NMO-corrected traces are stacked and the first arrival is time gated to determine the mean stacking amplitude. The procedure is depicted in figure 5.7.

This procedure is repeated for receiver coordinates varied over a grid of 20 by 20 m around the measured position. The mean stacking amplitude computed for each grid point is mapped in figure 5.8. The elliptic red area corresponds to the coordinates with the highest stacking amplitude. The new receiver position is determined by picking the grid point with the maximum amplitude. The elongated shape of the red area indicates that the position is not well-constrained in the direction perpendicular to the shot lines. Figure 5.9 shows the measured and corrected receiver positions with respect to the shot lines.

The receiver position is estimated separately for all the shot lines where the positioning-related errors (trigger delays, navigation problems, instrumentation defects etc.) other than the ones discussed above are discarded. The shot line that provided the best constrained receiver coordinates is selected as a reference shot line.

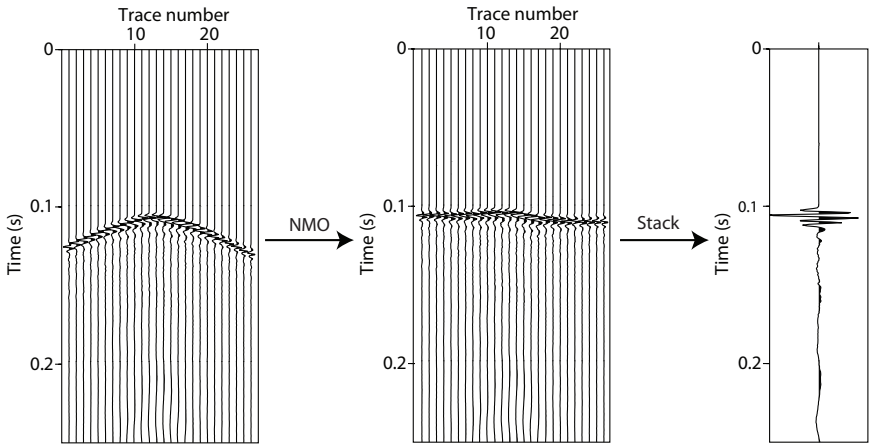

Figure 5.7: *Procedure of estimating the receiver positions: common-receiver gather containing near-offset traces only (left), normal-moveout correction applied (middle) and the stacked trace (right). The first arrival of the stacked trace is time gated and the mean amplitude is determined.*

5.3.3 Merging shot lines using crosscorrelation

The necessity of the crosscorrelation step is demonstrated in figure 5.10. The combination of only three shot lines according to their offset resulted in jittering and discontinuities in the recorded events and degradation of the lateral resolution. Although we reduced the errors related to the source and receiver positions before computing the offset, it is clear that this is not sufficient because of the variations of these errors between the shot lines.

The different shot lines are merged by crosscorrelating each of their traces with a panel of traces from the reference line, selected according to their offsets within 20 m range from the erroneous offset of the trace. In the crosscorrelated panel, the minimum positive and negative time lags and the offsets of their corresponding traces are picked and used as given in Eq. 5.2 to estimate the new offset value of the trace. The data are also interpolated in time (by a factor of 5) in order to pick time lags more accurately.

Difficulties arise at noisy traces and far offsets where the signal-to-noise ratio is relatively low. Consequently, picking the right maximum amplitude becomes hard and traces can end up at the wrong position. Bandpass filtering is applied to minimize the low-frequency noise that was mainly present in the two horizontal components Vx and Vy. Given the fact that the 3-C geophones were located at the same position in the field, the crosscorrelation results of the three receiver gathers are compared and combined to increase the number of successfully merged traces. This approach was particularly beneficial for the Vy component as many of the traces were initially not properly corrected due to the relatively weak signal recorded in this direction. The procedure, finally, combined almost 4000 traces (slightly more for the pressure component), together covering a distance of 1 km to

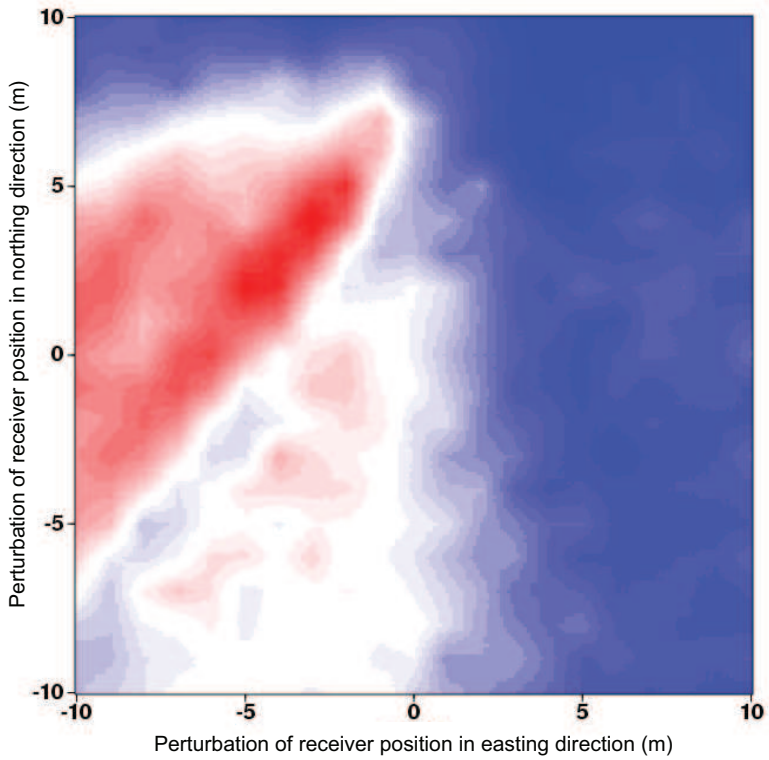

Figure 5.8: *Mean stacking amplitude mapped on the receiver-perturbation grid.*

one spatially dense common-receiver gather as shown for the four components in figure 5.11.

Although the effects due to the crossline offset in the data were not accounted for, it can be observed that the continuity of all the events is well preserved in the four components after the merging procedure. This implies that these effects are negligible in this case. However, in general, strong lateral variation in the crossline direction is expected to degrade the resolution of the data.

5.3.4 Regularization

The crosscorrelation step resulted in densely sampled receiver gathers with shot spacing varying between 0.1 and 3 m. Since most processing algorithms require a constant spatial interval, the obtained data are regularized. Various regularization techniques exist but we used the non-uniform discrete Fourier transform and the discrete inverse Fourier transform to achieve a regular shot spacing. The data in

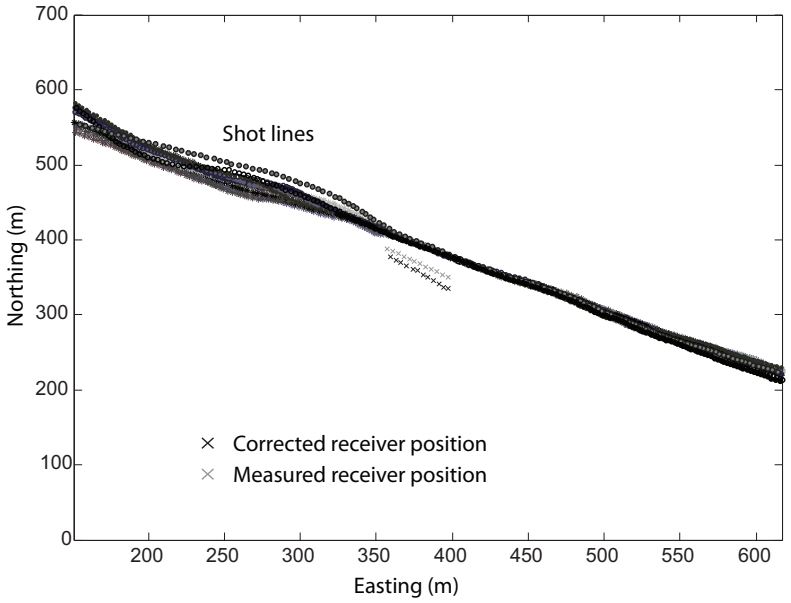

Figure 5.9: *Map showing measured and corrected receiver positions with respect to the 14 sailed shot lines.*

the spatial Fourier domain are obtained using the Riemann sum

$$\tilde{P}(k_x, \omega) = \sum_{n=0}^{N-1} P(x_n, \omega) e^{jk_x x_n} \Delta x_n, \tag{5.3}$$

with a variable spatial interval Δx_n defined as

$$\Delta x_n = \frac{x_{n+1} - x_{n-1}}{2}, \tag{5.4}$$

where x_n is the sample location, k_x is the wavenumber and ω is the temporal frequency.

Figure 5.12 shows the fk-spectra of common-receiver gathers recorded with the hydrophone and the horizontal component of the geophone. The amplitude spectrum obtained from transforming a common-receiver gather from one shot line with an average spacing of 4 m is compared to that of the combined line. The spatial aliasing of reflections and interface waves so obviously visible in figures 5.12(a) and 5.12(c) is no longer present after combining all the shot lines (figures 5.12(b) and 5.12(d)).

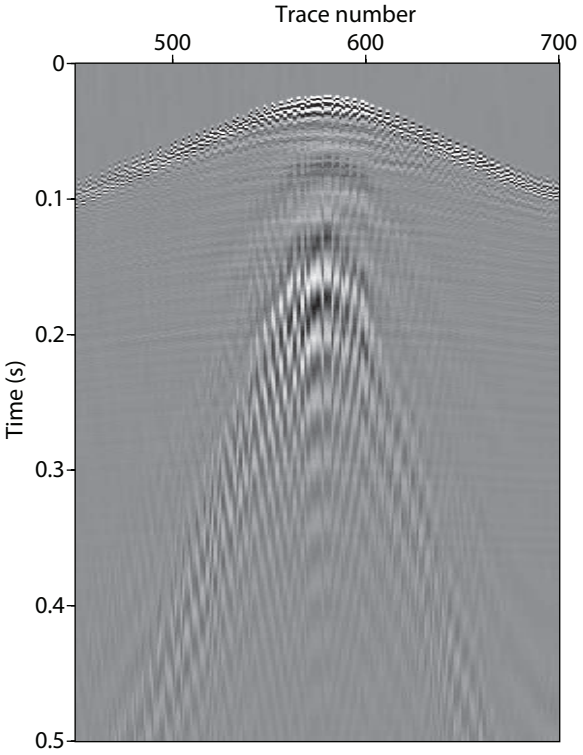

Figure 5.10: *Part of a common-receiver gather of the pressure recording, showing jittering and discontinuities resulting from combining three shot lines.*

The regularized data are then obtained by transforming the data back to the time domain using the uniform inverse spatial Fourier transform given by

$$P(x,\omega) = \frac{\Delta k_x}{2\pi} \sum_{m=-M}^{M} \tilde{P}(m\Delta k_x, \omega) e^{-jm\Delta k_x x}. \tag{5.5}$$

Δk_x has to be small enough to avoid aliasing. We have chosen a value equal to half the inverse of the maximum offset in the data. For Δx, we selected a constant spatial interval of 0.5 m which is larger than the aimed interval of 0.3 m but it was found adequate for the acquired data. The low frequency interface waves, dominant in all components, are removed from the data using an fk-filter before transforming the data back to the time domain. Figure 5.13 shows the four regularized components for one common-receiver gather. As expected, the P-wave reflections are mainly present in the pressure and vertical component whereas the converted modes can be identified in the horizontal inline component. Part of the data, enclosed in the black frames in figure 5.13, is enlarged in figure 5.14 where the converted modes are compared to the P-wave reflections. Low apparent velocity and horizontal polarization are distinctive features of PS-waves.

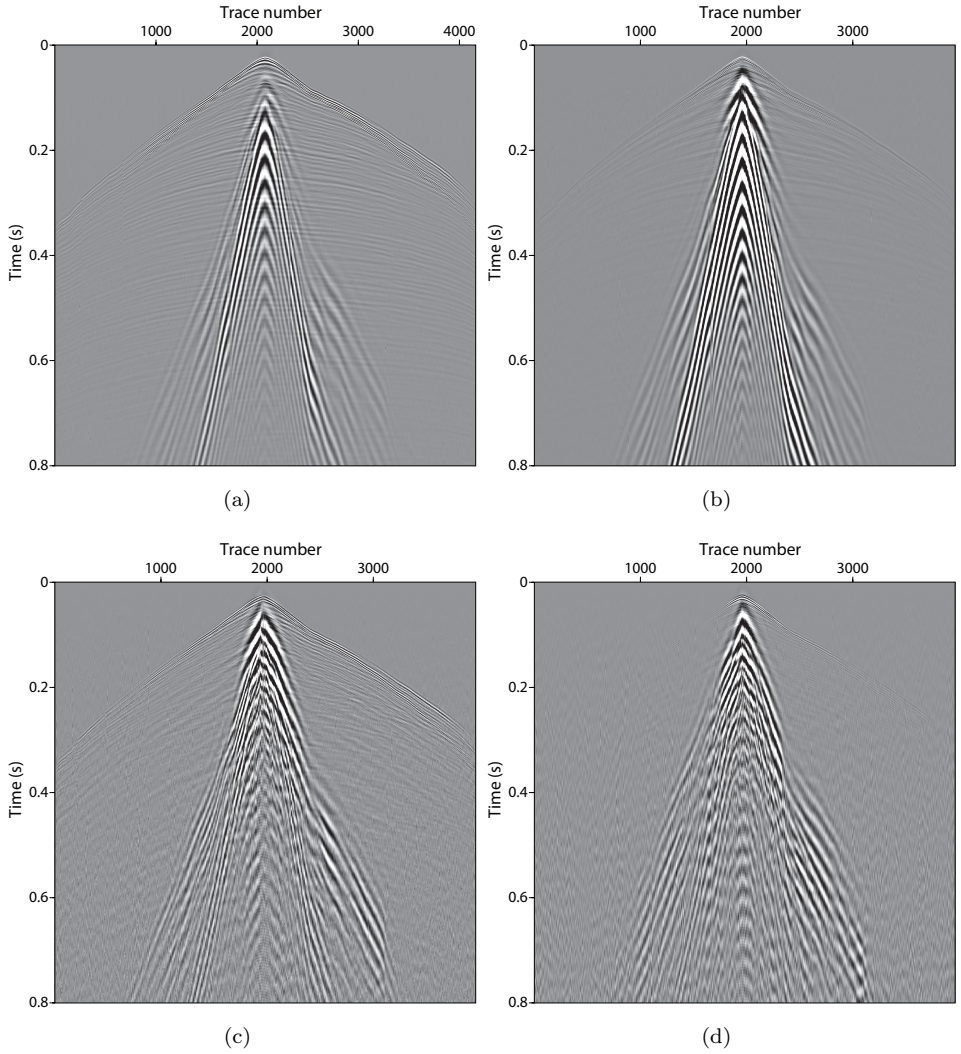

Figure 5.11: *The combined common-receiver gathers after applying the crosscorrelation step. a) Pressure, b) vertical component (Vz), c) horizontal inline component (Vx) and d) horizontal crossline component (Vy).*

The different steps of the proposed methodology are summarized in figure 5.15 for a small number of traces from the vertical component data. It can be noticed that we indeed succeeded to achieve a dense and regular spatial sampling without deteriorating the continuity of both the high-frequency first arrivals and the low frequency interface waves.

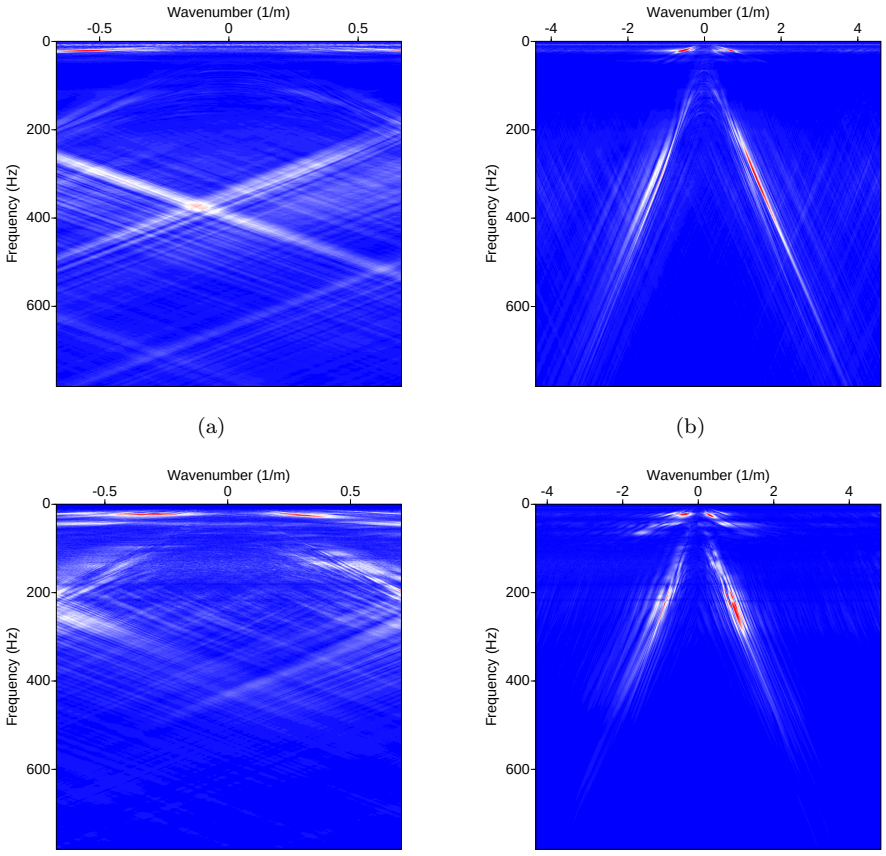

Figure 5.12: *Comparison of the fk-spectrum of the reference line with that of the combined line. a) Reference line of recorded pressure, b) combined line of recorded pressure, c) reference line recorded by the horizontal component and d) combined line recorded by the horizontal component.*

5.4 Conclusions

We developed a novel methodology aimed at acquiring seismic data recorded on the seabed and suitable for converted-wave processing. To avoid spatial aliasing, the primary focus of the method is on achieving spatially dense data by sampling one track multiple times. The shot spacing is then reduced by combining the different shot lines together. Inevitably with this method, the navigation of the sailed lines must be very precise and variation in source and receiver positions must be minimized.

The crosscorrelation step proved to be very effective in reducing the relative error in positioning between a reference shot line and the remaining lines. In the

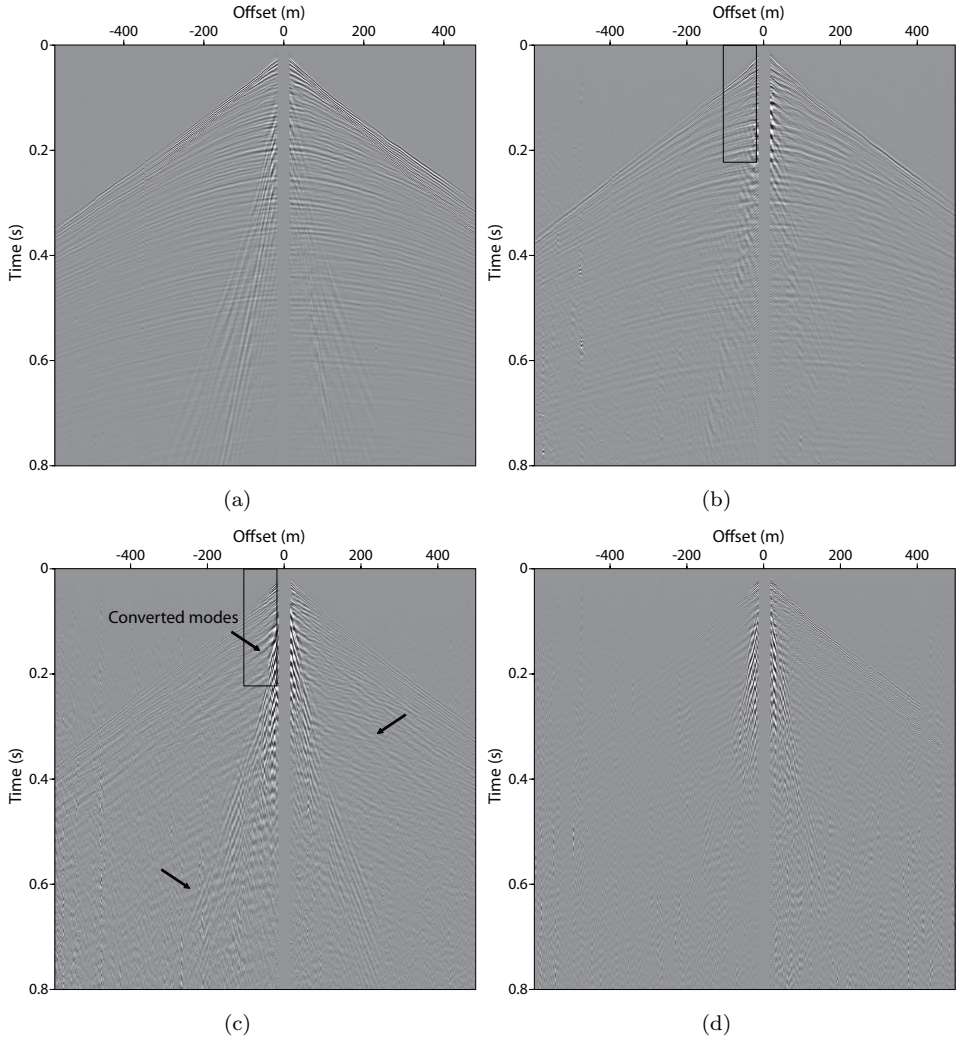

Figure 5.13: *Combined shot lines (see figure 5.11) after regularization and fk-filtering: a) pressure, b) vertical component, c) horizontal inline component (Vx) and d) horizontal crossline component (Vy). The black arrows indicate different converted modes identified in the horizontal inline component. The data captured in the black frame are enlarged in figure 5.14.*

synthetic data example, we showed that the processing step is insensitive to the gap between the shots in the reference line and the magnitude of the error involved, when the direct arrival is strongly present. The method is, however, affected by noise.

The devised methodology was successfully employed in a field experiment con-

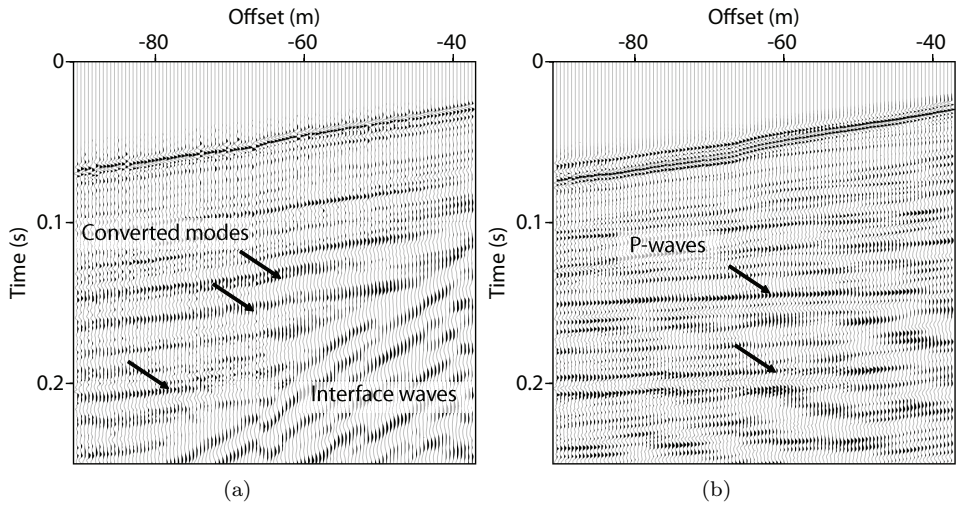

Figure 5.14: *Enlarged part of the horizontal inline component is compared to the vertical component. Black arrows indicate different converted modes in the horizontal component and two prominent P-wave reflections in the vertical component.*

ducted in the Danube River, in Hungary. The source and receiver-position errors of one specific shot line were quantified and corrected for. A special procedure was applied to estimate the underwater receiver positions using the direct arrival. This procedure reduced the error in the direction parallel to the shot lines but the error was not well-constrained for the direction perpendicular to them. Time interpolation and bandpass filtering were needed to enhance the results of the cross-correlation. The applied regularization procedure revealed that the data acquired with the novel methodology indeed resulted in a data set free of visible spatial aliasing.

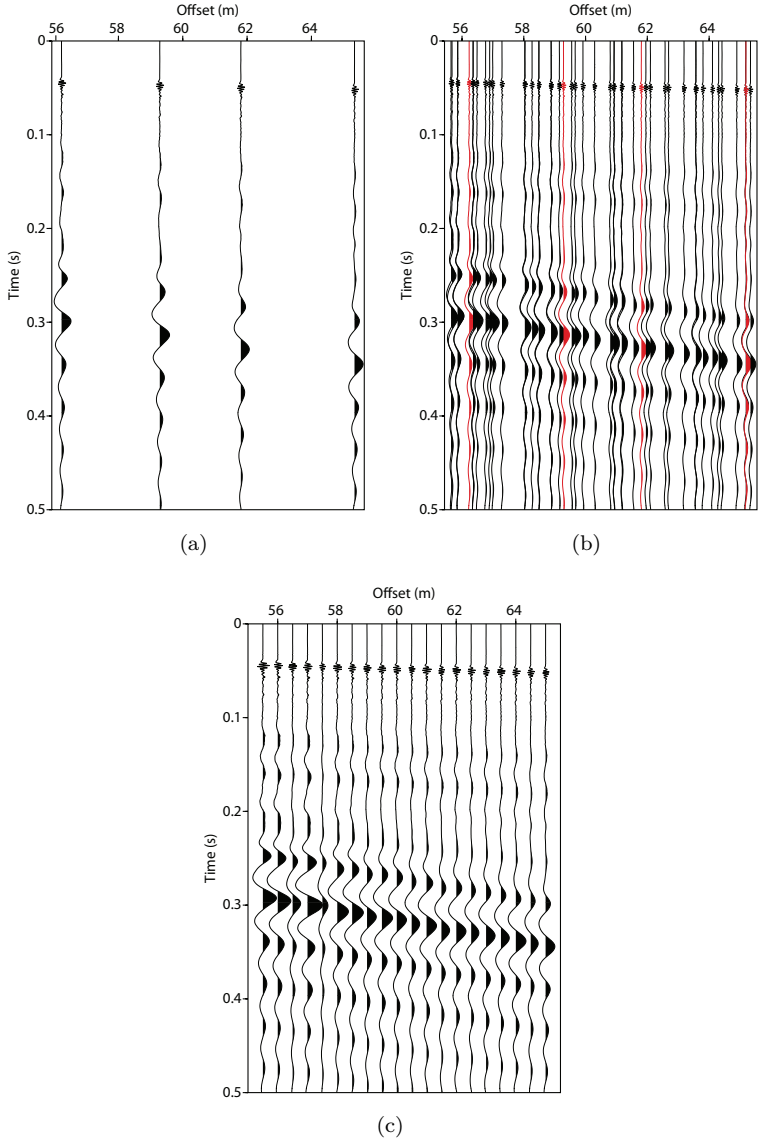

Figure 5.15: *The different steps of the methodology illustrated using a small number of traces from the vertical component: a) reference shot line, b) combined shot line (red traces are from the reference shot line) and c) combined shot line after regularization.*

Chapter 6

Separation of converted waves from shallow-water OBC data using wavefield decomposition

6.1 Introduction

Multicomponent measurements using ocean-bottom cables (OBC) and seismometers (OBS) are important because they allow the recording of the total wavefield and provide, consequently, better constraints to characterize the subsurface. This configuration is standardly applied to monitor hydrocarbon reservoirs and is becoming more common for shallow marine applications (e.g., Jin *et al.*, 2000; Mjelde *et al.*, 2003; Shillington *et al.*, 2008). The OBC and OBS configurations are favorable since pure P-waves as well as converted PS-modes are recorded. However, the presence of these waves in the different components complicates the processing flow of this type of data.

The processing of PS-waves is particularly challenging because it requires the separation of these modes from the pure P-waves and the estimation of both P- and S-wave velocity models. The wavefield can be separated in the Radon domain, based on differences in moveouts between the two type of waves, or using the theoretically-based elastic wave decomposition (Dankbaar, 1985; Wapenaar *et al.*, 1990). The decomposition filters derived from the two-way wave equation are applied to the horizontal and vertical components of the particle velocity and the pressure component, and combined to obtain upgoing and downgoing P- and S-wave potentials. Further processing of the data is facilitated and errors in the velocity model of the subsurface are reduced after applying the decomposition step.

Several successful examples, describing the application of this decomposition method to real data, have been published over the past decade in the literature (e.g., Amundsen & Reitan, 1995; Schalkwijk *et al.*, 2003; Muijs *et al.*, 2007, 2004). These papers discuss adaptive procedures aiming at estimating the medium parameters at the decomposition level and finding calibration filters accounting for the differences in sensor responses between the geophone and the hydrophone. The examples covered data sets acquired in relatively deep waters ($> 150\ m$) and required the interpretation of specific events as a criterion to find the calibration filters. This approach cannot be adopted straightforwardly for data recorded in very shallow wa-

ters ($\sim$4 m) as is the case for the example shown in this chapter. Due to the strong interference of the downgoing events, reflected at the water surface, with upgoing reflections (the downgoing and upgoing events can not be separately identified in the records), the adaptive decomposition scheme, as discussed by (Schalkwijk, 2001), is not applicable. Therefore, a different procedure is implemented.

Another difficulty encountered in the processing of PS-wave data is the estimation of S-wave velocities. These waves have an asymmetrical travel path and are non-hyperbolic, which requires taking higher order anisotropic terms in the velocity estimation procedure. Also, the P- to S-wave velocity ratio to match the velocities is unknown, which contributes to the uncertainties of the velocity computations. Ideally, pure SS-reflections are desired to infer S-wave velocity models. The absence of these pure modes in OBC data recorded in deep waters motivated several authors to develop methods to obtain this information. Grechka & Tsvankin (2002) combined PP and PS data to reconstruct SS-reflections whereas Gaiser & Vasconcelos (2009) used seismic interferometry to retrieve pseudo SS-waves.

For shallow marine environments, Allouche *et al.* (2011) have shown that S-wave reflections are excited when the source is located close to the water bottom (chapters 3 and 4 of this thesis). These modes converted at the water/sediment interface can be separated in the linear and parabolic Radon domain as shown in Chapter 3. Their evanescent character in water results in a kinematic behaviour of that of pure S-waves. These modes can therefore be used to estimate the S-wave velocity models of the shallow subsurface instead of PS-waves.

In this chapter, the processing of the multicomponent data acquired in the Danube River is discussed. The decomposition method is applied to two parts of the data, separately. The data are filtered in the horizontal slowness-frequency (p, ω) domain to a "low frequency" part representing mainly the S-wave reflections converted at the water bottom and PS-refractions and a "high frequency" part consisting of P-waves and PS-modes converted in the subsurface. This approach was chosen because of the different characteristics of the wavefield in the high and low frequency regimes. Two data sets, representing the upgoing S-wave potentials, result from this procedure. These can be used subsequently to infer S-wave velocity models.

6.2 Field acquisition and preprocessing

The data set processed in this chapter, was acquired in the Danube River downstream Budapest, Hungary. The acquisition and the preprocessing of these data, discussed extensively in Chapter 5, resulted in four densely-sampled receiver gathers, corresponding to the three components of the particle velocity and the pressure.

Since the receivers cable was released into the water and not placed by equipment, the orientation of the geophones is not exactly known. To correct for this, the horizontal components are rotated by minimising the energy in the crossline direction (perpendicular to the orientation of the cable). Since the subsurface can be laterally varying, only the direct arrival or the Scholte waves can be used for the minimisation procedure (Gaiser, 2007). In this case, we use the direct arrival to

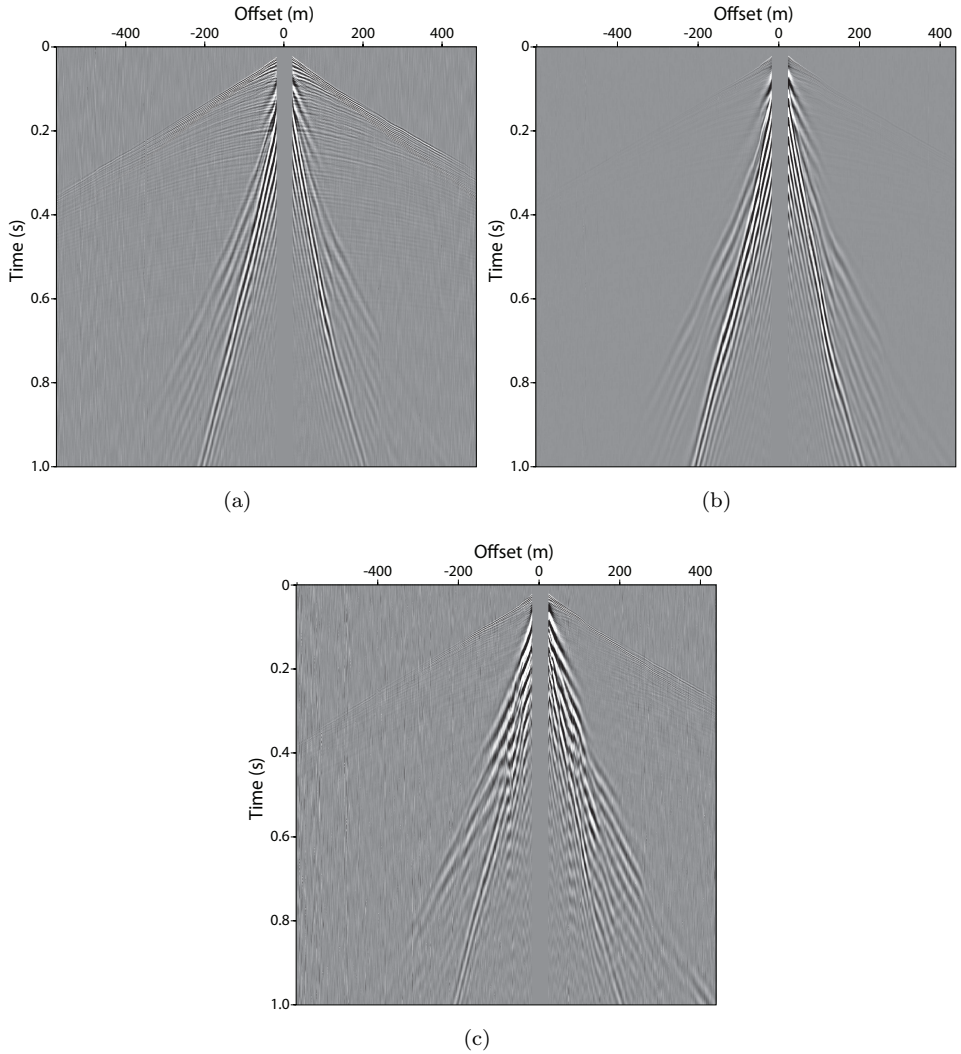

Figure 6.1: *The common-receiver gathers used for the decomposition: a) the pressure component, b) the vertical component and c) the rotated radial component.*

rotate the common-receiver gathers. The obtained rotated horizontal component is shown in figure 6.1 together with the vertical and pressure components. Only these three gathers are processed in this chapter.

6.3 Data analysis in the linear Radon domain and the horizontal slowness-frequency domain

The shallow water depth, in the survey area, complicates the interpretation of the recorded wavefield. As explained in Chapters 2 and 3, when the source is located close to the water bottom, the Scholte wave and also the non-geometric PS-wave are generated. These waves have a lower dominant frequency content and large amplitudes. Moreover, they travel at lower apparent speeds than the P-waves and PS-modes converted at reflectors in the subsurface. The interpretation of the events is facilitated by transforming the components displayed in figure 6.1 to the linear Radon (τ, p) domain. The results are shown in figures 6.2(a), 6.3(a) and 6.4(a).

Theoretically, the P-waves and the geometrically-converted waves are confined to a specific horizontal slowness range determined by the inverse of the sound speed in the water. For the presented data, this range is easily identified and is well visible in the recorded pressure as well as the radial component. The vertical component, however, is strongly dominated by the Scholte waves, visible at large horizontal slowness values, as can be observed in figure 6.3(a). The interaction of the generated pressure field with the water bottom may have different characteristics dependent on whether it occurs in the near-field or the far-field. For a band-limited source, this effect is dependent on the frequency and the height of the source with respect to the water bottom. For the Danube survey, the source was towed at a depth of 2 m and the water level in the river varied between 3 and 4 m. The near-field condition holds therefore for a range of frequencies. This can be demonstrated by transforming the data (figures 6.2(a), 6.3(a) and 6.4(a)) to the horizontal slowness-

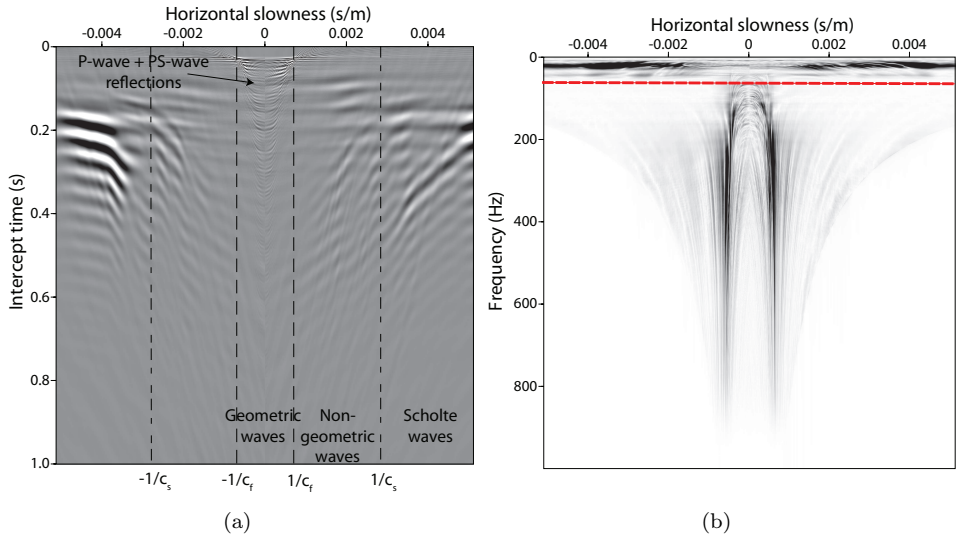

Figure 6.2: *Pressure component mapped in the (τ, p) domain (a) and in the (p, ω) domain (b).*

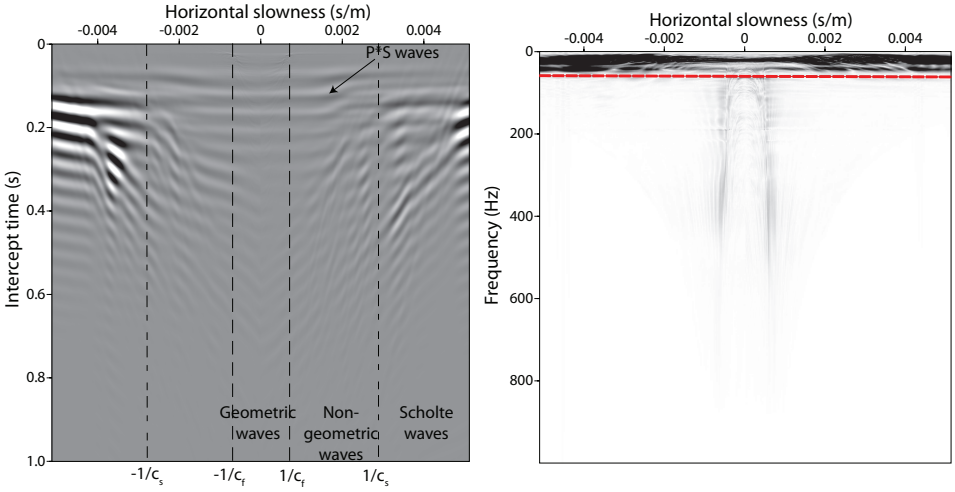

Figure 6.3: *The vertical component mapped in the* (τ, p) *domain (a) and in the* (p, ω) *domain (b).*

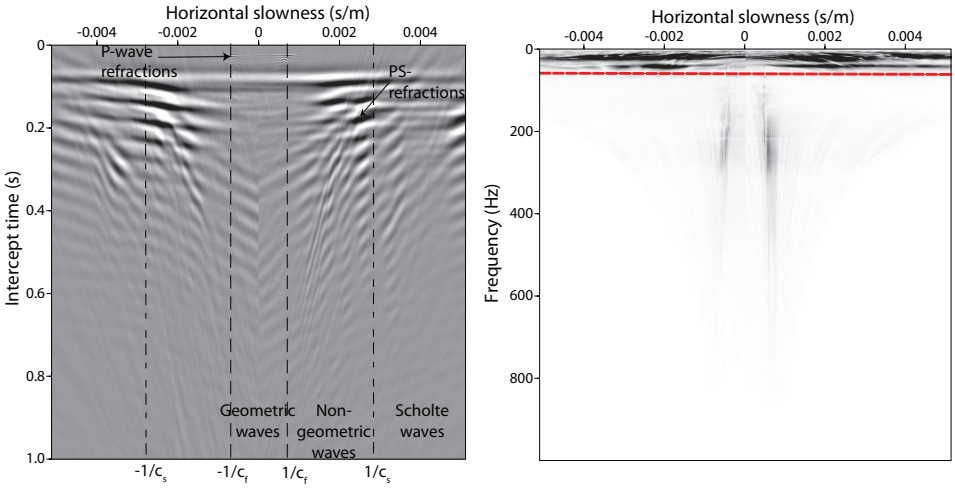

Figure 6.4: *The radial component mapped in the* (τ, p) *domain (a) and in the* (p, ω) *domain (b).*

frequency (p, ω) domain as shown in figures 6.2(b), 6.3(b) and 6.4(b). The (p, ω) domain is convenient to determine the frequency range for which the near-field effects are dominant. It is also the domain in which we apply the elastic wave decomposition.

Some remarks can be made on the (p,ω)-transformed common-receiver gathers. The pressure component has a wider range of frequencies and appears to be less sensitive to the Scholte waves than the other components. Mainly the vertical component is dominated by this strong interface energy. Refractions are also strongly present in this data set. This is also observed in the time domain records. Furthermore, it can be noticed that a considerable amount of energy is mapped at horizontal slowness values enclosed between the interface waves and the refractions, suggesting the presence of non-geometric S-waves in the three common-receiver gathers. Moreover, for the radial component, reflections at frequencies between 100 and 150 Hz seem to be weak.

Due to these general differences in the appearances of the components, which complicate the application of the elastic wave decomposition, the data are separated in two parts, as indicated by the dotted lines in figures 6.2(b), 6.3(b) and 6.4(b). The decomposition step is performed on each part separately, allowing the formulation of different criteria to find the calibration filters and enhance the results of the decomposition.

6.4 P/S wavefield decomposition filters

The elastic decomposition operators were derived in the wavenumber-frequency (k,ω) domain in section 2.7. However, it is more convenient to express the decomposition equation in the (p,ω) domain because the operators become then frequency independent. Consequently, the decomposition equation can be written as

$$\check{\vec{D}}^{\pm}(z_1) = -\check{\mathbf{N}}_1^{\pm}(z_1)\check{\vec{T}}_z(z_1) + \check{\mathbf{N}}_2^{\pm}\check{\vec{v}}(z_1), \tag{6.1}$$

where $\check{\vec{T}}_z(z_1)$ and $\check{\vec{v}}(z_1)$ are the (p,ω) transformed stresses and particle velocity measurements and $\check{D}^{\pm}(z_1)$ are the downgoing and upgoing wavefields representing the P- and S-wave potentials just below the water bottom, denoted by $\check{\Phi}^{\pm}$ and $\check{\Psi}^{\pm}$, respectively.

For the OBC configuration, the shear stresses vanish and the normal stress is equal to minus the acoustic pressure $\check{P}$ such that

$$-\check{\vec{T}}_z(z_1) = \begin{pmatrix} 0 \\ \check{P}(z_1) \end{pmatrix}. \tag{6.2}$$

The decomposition matrices are given by

$$\check{\mathbf{N}}_1^{\pm}(z_1) = \frac{1}{2}\begin{pmatrix} \pm\frac{p}{q_p(z_1)} & 1 \\ -1 & \pm\frac{p}{q_s(z_1)} \end{pmatrix}, \tag{6.3}$$

and

$$\check{\mathbf{N}}_2^{\pm}(z_1) = \frac{\rho(z_1)c_s^2(z_1)}{2}\begin{pmatrix} 2p & \pm\frac{c_s^{-2}(z_1)-2p^2}{q_p(z_1)} \\ \mp\frac{c_s^{-2}(z_1)-2p^2}{q_s(z_1)} & 2p \end{pmatrix}, \tag{6.4}$$

where $q_p = (c_p^{-2} - p^2)^{1/2}$ and $q_s = (c_s^{-2} - p^2)^{1/2}$ are the vertical slownesses of the P- and S-wave just below the water bottom. The elastic parameters ρ, c_p and c_s at the level of decomposition are necessary for the implementation of the decomposition.

The equations above describe the elastic decomposition on the receiver side and should then, according to the theory, be applied to a common-shot gather. Since such a type of gather is not available, the common-receiver gathers, discussed above, are used for the decomposition. This means that we implicitly assume that the medium is laterally invariant (Schalkwijk, 2001). This assumption can be considered plausible given the observed symmetry in events at positive and negative offsets.

Furthermore, a line source was assumed for the derivation of the operators. This is not the case for the field data and therefore we have to correct for the amplitudes. This can be done by multiplying the data by the square root of time to account for the geometric spreading in 3D (Schalkwijk, 2001; Muijs *et al.*, 2007).

6.4.1 Medium parameters at the water bottom

Wavefield decomposition requires the knowledge of the seismic parameters at the water bottom. These parameters can be estimated from the data by applying the decomposition in an adaptive scheme as it was discussed by Schalkwijk *et al.* (2003) and Muijs *et al.* (2007). In this procedure, a filter is estimated by imposing a specific criterion which is valid in a selected time window. The filter is subsequently inverted to obtain the density and the P- and S-wave velocities.

The medium parameters of the water bottom can also be estimated from the Scholte wave for example. The dispersion curves of these waves, strongly present in these data, can be inverted to obtain the required elastic parameters. Kruiver *et al.* (2010) used this technique to infer density and P- and S-wave velocity profiles from the presented common-receiver gathers. For the upper layer of sediments, we found the following values: $c_p = 1650$ m/s, $c_s = 400$ m/s and $\rho = 1500$ kg/m^3. These results are used here to compute the decomposition operators.

6.4.2 Sensor calibration

Variations in instrument response between the hydrophone and the geophone can affect the results of the decomposition. Each sensor has its specific transfer function that modifies the measured wavefield while converting it to voltage. The transfer function is dependent on the sensitivity factor K, the damping factor H and the resonance frequency f_0. The sensor specifications of the OBC are known and are used to account for the response differences in the data.

The corresponding transfer function R varies with angular frequency ω and can be computed using (Pieuchot, 1984)

$$R(\omega) = \omega^2 K/(\omega^2 - 2jH\omega\omega_0 - \omega_0^2), \tag{6.5}$$

where $\omega_0 = 2\pi f_0$. For the cable deployed in the survey, $K = 20.9$ V/(m/s) for the geophone and $K = 4.58$ V/bar for the hydrophone. Furthermore, the resonance frequency f_0 is 10 Hz and the damping H is 0.7 for both the geophone and the hydrophone.

6.5 High-frequency upgoing S-waves

The objective of applying the decomposition step is to separate the S-waves from the P-waves and assess the presence of converted energy in the shallow marine environment. Therefore, our emphasis is placed on obtaining the upgoing S-wave potential Ψ^-. This potential is a weighted summation of the pressure and the vertical and horizontal components of the particle velocity as given by Eq. 6.1.

The decomposition filters, given in Eqs. 6.3 and 6.4, are applied to the high frequency part of the data, filtered as indicated by the red dashed lines in figures 6.2(a), 6.3(a) and 6.4(a). The separate contribution of each component to the upgoing S-wave potential is transformed to the (x,t) domain and shown in figure 6.5. A straightforward combination of these components to obtain Ψ^- did not give satisfactory results. This is due to the coupling effect of the geophone compared to that of the hydrophone. To improve the results of the decomposition, a filter accounting for this effect can be estimated from the data.

In the procedure adopted by Schalkwijk (2001), a criterion based on minimising user-defined downgoing waves in the upgoing wave component was formulated, in order to determine the calibration filters. However, such an approach is not applicable for this data set, acquired in a very shallow water, because an interpretation of upgoing and downgoing waves is very difficult. Alternatively, we can define a different criterion to estimate the coupling filter.

For the high-frequency data discussed in this section, we assume that the PS-converted energy, in the pressure and the vertical recordings, can be neglected at near-offsets. This can be explained by the small conversion coefficients of plane waves for small angles of incidence. This is especially the case for shallow unconsolidated sediments (Allouche *et al.*, 2008). Based on this assumption, we state that no upgoing S-wave energy is present in the sum of the hydrophone and the vertical component after applying the decomposition filters at small offsets. This is then used as a criterion to determine the coupling filter. Assuming that the hydrophone has a perfect coupling, we write for the upgoing S-wave potential from Eqs 6.3 and 6.4

$$\check{\Psi}^- = -\frac{p}{2q_s}\check{P} + F_c(\omega)\rho(z)c_s^2\left[p\check{v}_z - \frac{c_s(z)^{-2}-2p^2}{2q_s}\check{v}_x\right], \tag{6.6}$$

where F_c denotes the filter describing the geophone coupling.

A least-squares optimization procedure is formulated based on this criterion to obtain F_c. The least-squares error is defined as

$$\epsilon = \sum_k \sum_l \frac{1}{2}\left|F_c(\omega_k)\rho(z)c_s^2 p_l\check{v}_z - \frac{p_l}{2q_s}\check{P}\right|^2. \tag{6.7}$$

This coupling filter is estimated in the (τ,p) domain for the selected data windows shown in figure 6.6. The upper two windows correspond to the pressure and the vertical velocity components and are used as an input for the minimisation step. The data resulting from applying the filter and the residual energy after subtraction are displayed in the lower windows. The amplitude and the phase of the estimated coupling filter are displayed in figure 6.7. The components recorded by the geophone are convolved with the estimated filter before the summation. The obtained

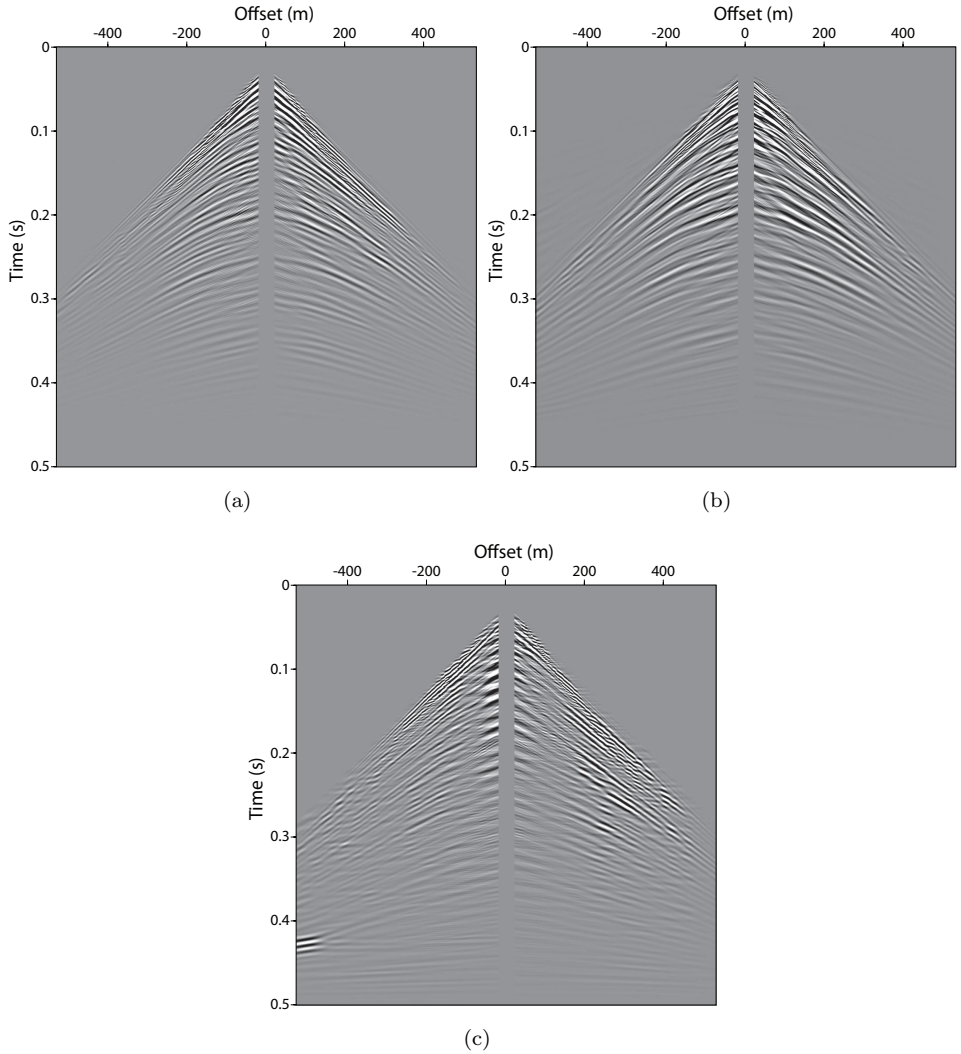

Figure 6.5: *The filtered contributions of the pressure component (a), the vertical component (b) and the horizontal component (c) in the* (x, t) *domain. These contributions are added together to obtain the high-frequency upgoing S-wave potential.*

downgoing S-wave component is compared to the (p, ω)-filtered radial component in figure 6.8. Some minor differences can be noticed between the two records. The decomposed result show slight improvements in the appearance of converted waves. However, there is also a leakage of P-wave energy to the upgoing S-wave potential (see the arrows in figure 6.8), suggesting that the medium parameters used for the decomposition are inaccurate. This can be explained by the fact that the Scholte

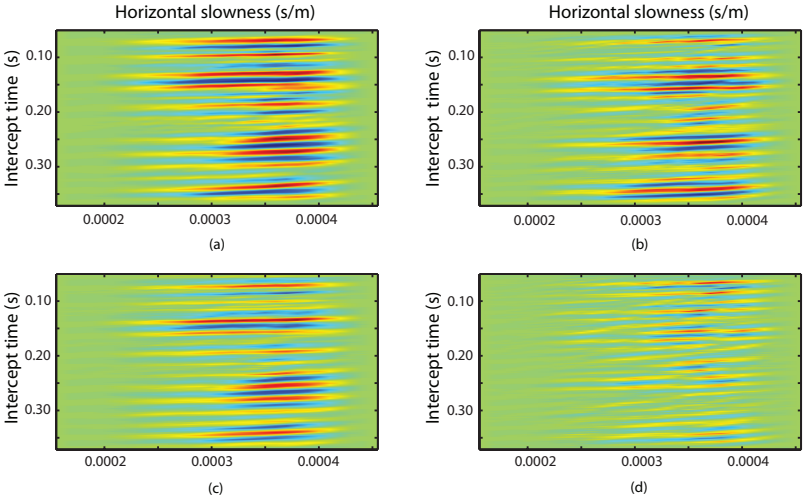

Figure 6.6: *Estimation of the coupling filter F_c for the high-frequency regime. Data windows extracted from (a) the pressure component and (b) the vertical component. (c) The vertical component after applying the coupling filter and (d) the residual energy after subtracting the filtered vertical component from the pressure.*

waves, inverted to estimate these values, have a frequency content which is much lower than that of the reflections considered here. As it can be observed in the data, the Scholte waves are not dispersive and they are limited to the frequencies ranging between 10 and 50 Hz. Inaccuracies in the estimated medium parameters can also be caused by strong seismic attenuation typically encountered in unconsolidated sediments (Eggenberger *et al.*, 2010).

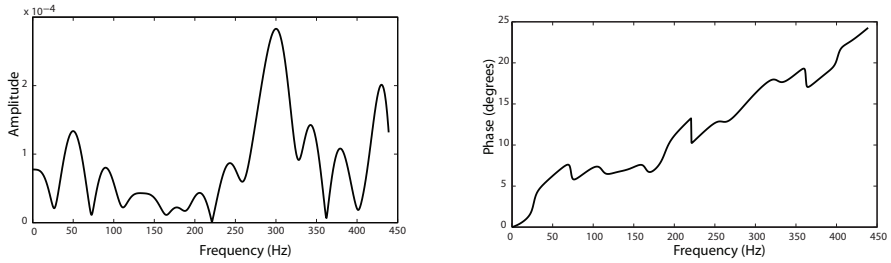

Figure 6.7: *The amplitude (a) and the phase (b) of the estimated coupling filter F_c used to correct the high-frequency part of the data.*

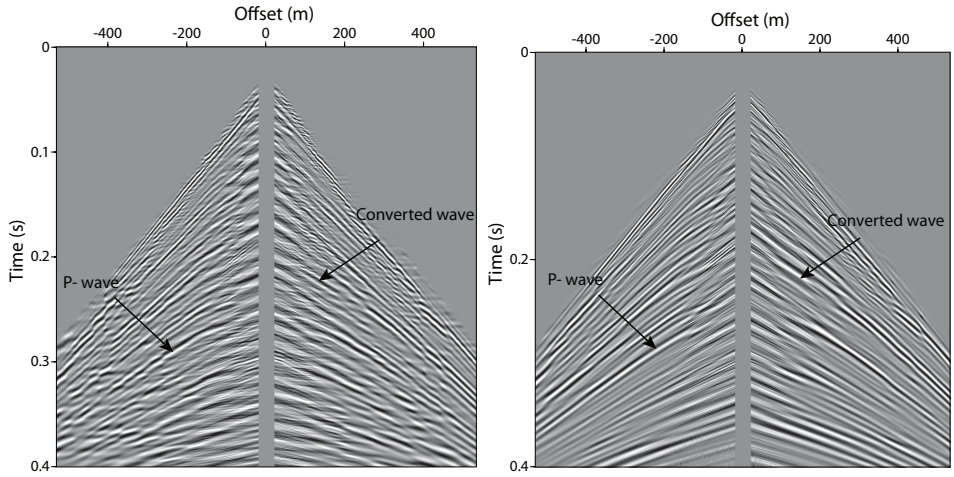

(a) (b)

Figure 6.8: *Comparison between the horizontal component, before applying the decomposition and coupling filters, and the upgoing S-wave potential. AGC with a time window of 0.2 s was applied to the data to improve the visibility of the reflections.*

6.6 Low-frequency upgoing S-waves

Elastic decomposition is also performed on the low-frequency part of the data. The separate contribution of each component to the upgoing S-wave potential is transformed to the (x,t) domain and shown in figure 6.9. The data are dominated by arrivals with low apparent velocity. While the vertical velocity and pressure components look similar, the horizontal component shows some discontinuities at small offsets.

Also for this part of the data, an enhancement of the decomposition results necessitates a correction of the coupling effect. However, a different minimisation criterion needs to be formulated since PS-converted energy can be observed at near-offsets as was shown in the Ghent data set, discussed in Chapter 4. The non-geometric PS-waves were observed even in the hydrophone component (see figure 4.6).

In this case, we make use of the presence of Scholte waves to estimate a filter which accounts for the coupling difference between the geophone and the hydrophone. Multicomponent recording of these interface waves is useful for the characterization of the subsurface. The ratio between the pressure and the vertical component of the particle velocity is known as the impedance I and is defined in the (p,ω) domain as (van Dalen, 2011)

$$I = \left.\frac{\tilde{P}}{\tilde{v}_z}\right|_{p=p_{sch}} = -\left.\frac{\rho_f}{q_f}\right|_{p=p_{sch}}, \tag{6.8}$$

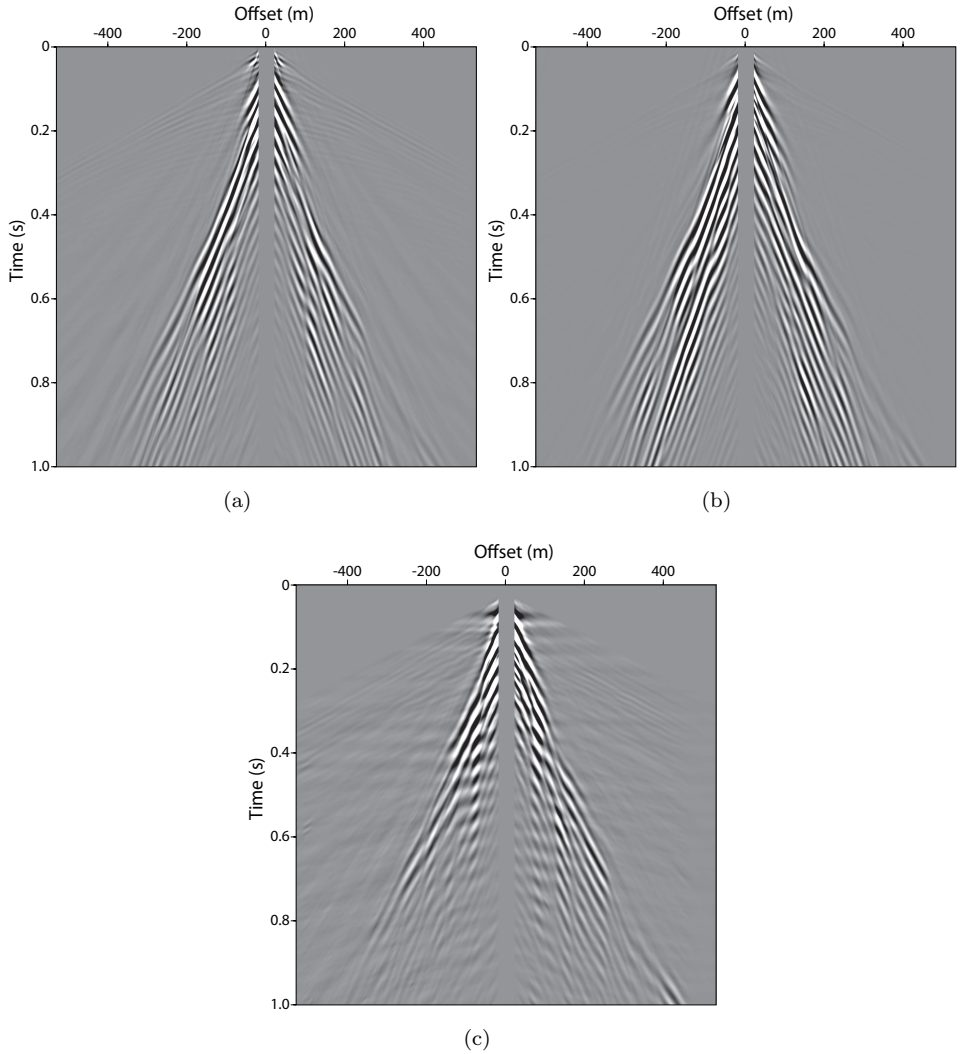

Figure 6.9: *The filtered contributions of the pressure component (a), the vertical component (b) and the horizontal component (c) in the (x,t) domain. These contributions are added together to obtain the low-frequency upgoing S-wave potential.*

where ρ_f is the density of the water and the vertical slowness $q_f = \sqrt{\frac{1}{c_f^2} - p^2}$. For $p = p_{sch} > 1/c_f$, the vertical slowness becomes $q_f = -j\sqrt{p_{sch}^2 - \frac{1}{c_f^2}}$ with p_{sch} being the slowness corresponding to the Scholte waves.

When the coupling of the geophone is not perfect with respect to the hy-

drophone, we can rewrite Eq. 6.8 into

$$\tilde{P}\Big|_{p=p_{sch}} = \frac{-j\rho_f}{\sqrt{p_{sch}^2 - \frac{1}{c_f^2}}} F_c(\omega)\tilde{v}_z\Bigg|_{p=p_{sch}} . \tag{6.9}$$

Estimating the Scholte wave velocity from the S-wave velocity, the filter $F_c(\omega)$ can be found by a least-squares minimisation procedure similar to the one applied in the high-frequency regime. The least-squares error is defined as

$$\epsilon = \sum_k \sum_l \frac{1}{2} \left| \tilde{P} + \frac{j\rho_f}{\sqrt{p_l^2 - \frac{1}{c_f^2}}} F_c(\omega_k)\tilde{v}_z \right|^2 . \tag{6.10}$$

The Scholte waves are separated from the data in the (p, ω) domain. These waves were identified by their large horizontal slowness and low frequency content. After multiplying the vertical component by the factor given in Eq. 6.8, we assume that the difference between the components is due to the coupling effect. The Scholte waves recorded by the hydrophone and the geophone are displayed in figure 6.10. It can be noticed that the Scholte waves are not very dispersive in this case. Subsequently, a filter is estimated by minimising the difference between the two records. The parts of the data used for the minimisation are displayed in figure 6.11 and the estimated filter in figure 6.12. The phase behaviour of this calibration filter shows a negative linear shift and is different than that obtained for the high-frequency part of the data. This difference in phase behaviour is not entirely understood. It should be noted that we assume that the coupling filter is the same for the horizontal and vertical components. This is probably not the case (Bagaini & Muyzert, 2004).

The estimated filter is convolved with the horizontal and vertical component and summed to obtain the downgoing S-wave potential for the low frequencies. The result is displayed in figure 6.13. The decomposed gather is dominated by the PS-refractions with the linear moveout and the PS-reflections converted at the water bottom. The latter are only visible at small offsets and are more easy to identify in the (τ, p) domain where they can also be filtered from the refractions (see figure 6.4(a)) and subsequently, analysed to obtain an S-wave velocity model of the shallow subsurface.

6.7 Conclusions

Elastic wave decomposition, aiming at separating the converted modes from the P-waves, was applied to the Danube data. However, the shallow depth of the water, encountered in the survey area, required an adaptation of the standard decomposition schemes. The decomposition relies on accurate knowledge of the water-bottom elastic parameters and on a perfect calibration of the sensors. The medium parameters are known from the inversion of the Scholte waves dispersion curves but the coupling filters need to be determined from the data.

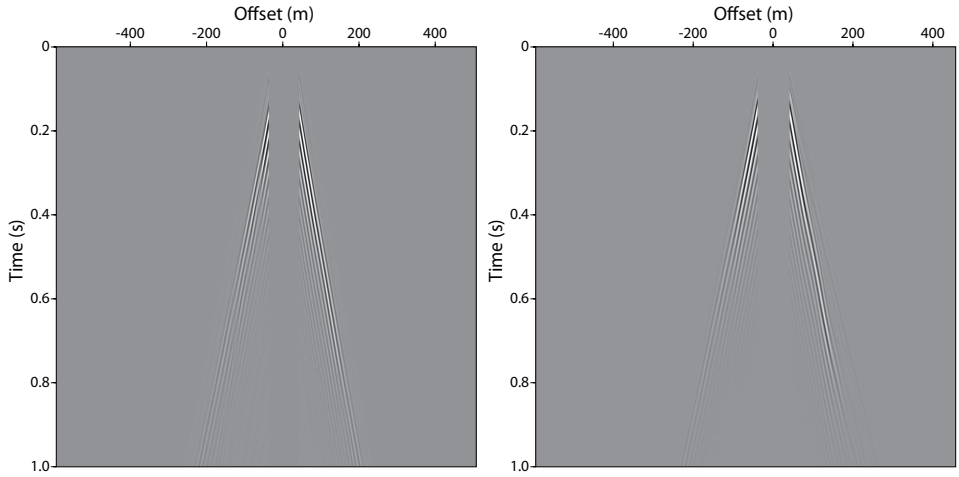

Figure 6.10: *The Scholte waves filtered from the pressure component (a) and the vertical component (b).*

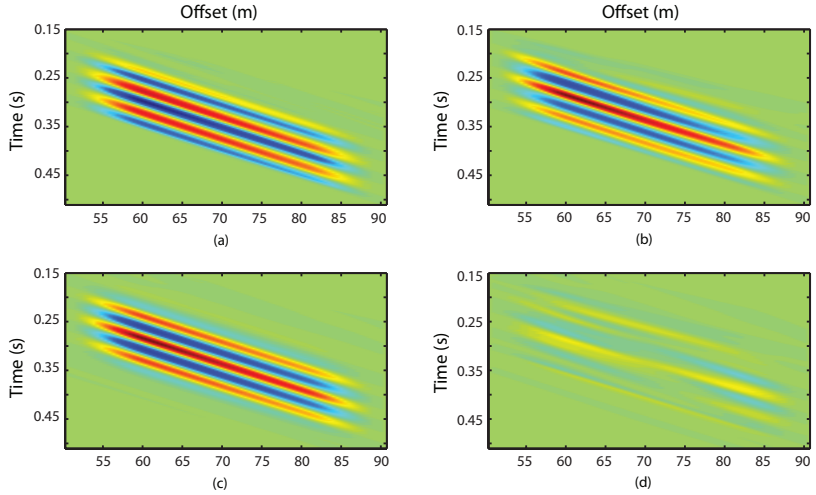

Figure 6.11: *Estimation of the coupling filter F_c for the low frequency regime. Data windows extracted from (a) the pressure component and (b) the vertical component. (c) The vertical component after applying the coupling filter and (d) the residual energy after subtracting the filtered vertical component from the pressure.*

The multicomponent OBC data were analysed in the (τ, p) and the (p, ω) domains. Based on this analysis, the data were separated in a high-frequency regime, consisting of P-wave reflections and PS-converted modes, and a low fre-

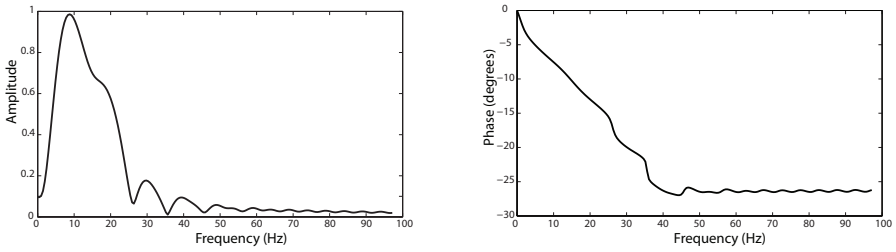

(a) (b)

Figure 6.12: *The amplitude (a) and the phase (b) of the estimated coupling filter F_c used to correct the low-frequency part of the data.*

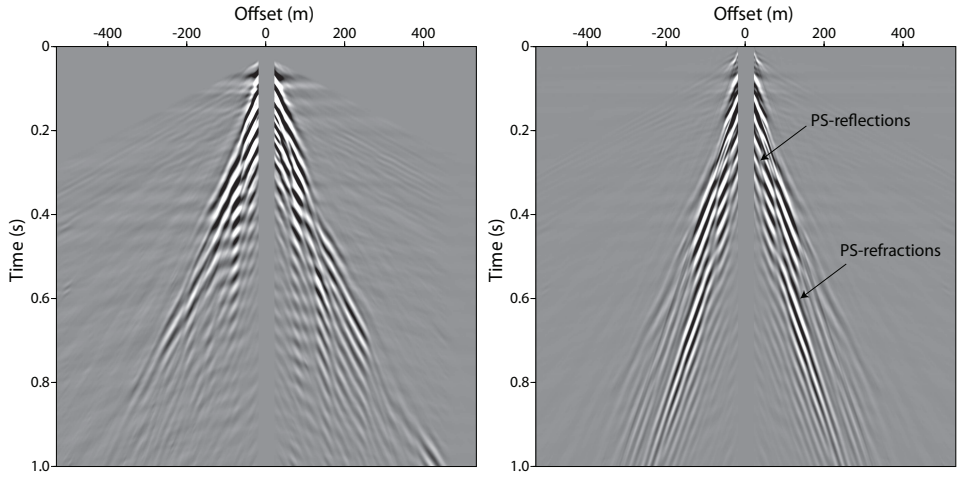

(a) (b)

Figure 6.13: *Comparison between the horizontal component, before applying the decomposition and coupling filters, and the obtained upgoing S-wave potential.*

quency regime including the non-geometric PS-waves and PS-refracted modes.

For the high-frequency regime, imperfections in the geophone coupling were corrected for by minimising the contribution of the pressure and vertical components to the upgoing S-wave potential at near-offsets. This implies that these two components contain no converted wave energy at these offsets, an assumption which is only valid for plane waves. The decomposed result shows an improvement in the visibility of some converted modes mainly at later arrival times. The presence of P-wave energy after the decomposition step is attributed to inaccuracies in the estimated medium parameters. This is because the Scholte waves used to estimate these parameters has a frequency range which is not overlapping that of the data.

Elastic wave decomposition was also applied to the low frequency part of

the data. The three components were dominated by events with low apparent moveout. The Scholte wave is filtered and used to estimate the coupling filter. The decomposed result consists of waves converted at the water bottom with their non-geometric part and PS-refractions.

Velocity analysis and other standard processing steps can be performed to the two data sets. The information obtained from these data sets is considered complementary. The low frequency part, representing waves converted at the water bottom, can be treated as pure S-waves (once the refractions are removed) and used to obtain an S-wave image of the very shallow part of the sediments. The processing of high-frequency data, consisting mainly of waves converted at the reflectors, can provide a PS-wave image of the deeper part of the subsurface.

Chapter 7
Conclusions and outlook

7.1 Conclusions

The modelling and field data, presented in this thesis, demonstrate the great potential of PS-waves to map the shallow marine subsurface and infer its seismic properties. Various modes have been observed: P-waves converted at the water bottom as well as at reflectors. Despite the high c_p/c_s ratios, typically encountered in marine sediments, conversion at the water-sediment interface is considered important mainly when the source is located close to the bottom, which is generally the case for shallow water depths. Geometric and non-geometric PS-waves are excited in this setting; as was extensively discussed in Chapter 3 and Chapter 4. The non-geometric PS-waves have distinctive properties:

- This particular mode of conversion is generated only when the S-wave velocity, c_s, is lower than the sound speed in the fluid c_f. For the rayparameter range $[1/c_f, 1/c_s]$, the incident P-wave is evanescent in the fluid but converts to a propagating S-mode in the sediments, giving rise to the P*S-wave.

- Due to their evanescent character in the fluid, the P*S modes can only be observed when the dominant wavelength of the emitted signal exceeds the source height. This effect is instantaneous; therefore, kinematically, they appear to be excited at the interface.

- Since the P-waves are confined to the rayparameter range $[-1/c_p, 1/c_p]$, the P*S modes can be separated in the Radon domain and processed as pure S-waves excited by a shear source placed on the water bottom.

- In the solid, P*S-wave appears at a specific angle measured from the projection point of the source on the interface, where it diverges from the head waves. This angle of appearance is dependent on the ratio between the S-wave velocity and the sound speed of the fluid. This ratio is higher for unconsolidated sediments resulting in a broader region of appearance.

Optimum recordings of converted modes are not simply achieved by adapting the conventional seismic method for P-waves. Several acquisition aspects, related particularly to the spatial sampling, remain challenging in practice:

- Dense spatial sampling on the source side, although partly addressed in Chapter 5, it is still difficult to achieve in the field. The method adopted worked well for the Danube data but if strong lateral variations exist, this method will fail ultimately.
- The requirements for the positioning errors are less tolerant as we aim at recording high frequency PS-waves. These errors can be minimised to the order of 5-10 cm by the use of Differential position sensors (DPS) for example.
- Determining the underwater positions of the receivers was one of the problems that needed to be solved in the preprocessing of the Danube data. We used the direct wave to estimate the relative distance between the shots and the receiver. However, more accurate positioning measurements can be obtained using sound pulses sent by pingers.
- In Chapter 4, it was shown that the P*S-waves have a narrow optimum offset window and are observed at small offsets. Consequently, the distance between source and receiver is required to be as short as possible in practice, in order to record this specific mode of conversion.
- The coupling of the geophones placed on the water bottom was not ideal in the field data presented in this thesis. Mainly the horizontal components showed low-quality recorded data that affected the results of the decomposition. Generally, the coupling can be improved by burying the receivers in the sediments using underwater robots.

The data (pre-)processing steps discussed in Chapter 4 and 5 were only applied to one common-receiver gather. In principle, the same procedure can be repeated for the other common-receiver gathers and standard techniques can be applied subsequently to obtain three images of the shallow subsurface: a PP-, a PS- and an SS-image. However, the following issues may complicate the processing.

- The presence of the Scholte waves in the data is an indication of the near-field interaction between the incident wavefield and the water bottom and hence an indication of the excitation of the non-geometric PS-waves. Similar to the ground roll in the land case, these waves have strong amplitude and low velocity and are interfering with reflections, particularly at small offsets. Separation of these waves from the non-geometric modes can be problematic. Since both waves have similar frequency content, filtering is only possible when spatial aliasing is avoided.
- The elastic decomposition is a convenient method to separate P-waves from converted modes. But to obtain satisfactory results, the medium parameters must be determined accurately. The inversion of the dispersion curves of the

Scholte waves is not an appropriate method when the frequency content of these waves and that of the decomposed data are not overlapping. In the case of the Danube data, the Scholte waves were not dispersive and had therefore a narrow frequency range.

- For shallow water depths, it is difficult to interpret upgoing and downgoing waves. Therefore a user-defined criterion based on such an interpretation can not be applied to estimate calibration filters. The methods, adopted in Chapter 6 to correct for variation in hydrophone and geophone responses, assume that the coupling effects in the horizontal and vertical direction is similar. This is probably not the case in practice.

7.2 Outlook

There are some research opportunities that still need to be explored to fully benefit from the converted modes.

- The data in this thesis were collected using a static OBC position and the processing steps were only applied to one common-receiver gather. The same acquisition and processing steps can be repeated for other receiver positions and combined to obtain a PP-, PS- and SS-image of the subsurface.

- In the real data example of Ghent, it was shown that the non-geometric waves are converted to P-waves and recorded in the pressure component. This may imply that these waves can be recorded with the conventional P-wave configuration composed of an air gun and a hydrophone streamer by just making sure that they are located close to the interface. The conversion of the P*S reflections to the P-mode at the water bottom should be studied as well. If this conversion is considerable, this configuration can be potentially much more efficient in collecting S-wave information than with OBC's.

- As mentioned above, the non-geometric PS-modes and the Scholte waves are both generated when conversion of the incident wavefield occurs in the near-field. Combining the information from both types of waves is obviously possible. A joint inversion may give better constraints to infer c_s velocity profiles.

Bibliography

Aki, K., & Richards, P. G. 2002. *Quantitative Seismology, 2nd ed.* University Science Books.

Allouche, N., Drijkoningen, G. G., Versteeg, W., & Simons, D. G. 2008. Studying converted waves in shallow marine environment. *Pages 369–374 of: Proceedings of the 9th European Conference on Underwater Acoustics (ECUA).*

Allouche, N., Drijkoningen, G. G., & van der Neut, J. 2010. Methodology for dense spatial sampling of multicomponent recording of converted waves in shallow marine environments. *Geophysics*, **75**(6), WB29–WB37.

Allouche, N., Drijkoningen, G. G., Versteeg, W., & Ghose, R. 2011. Converted waves in a shallow marine environment: experimental and modeling studies. *Geophysics*, **76**(1), T1–T11.

Amundsen, L., & Reitan, A. 1995. Decomposition of multicomponent sea-floor data into upgoing and downgoing P- and S-waves. *Geophysics*, **60**(2), 563–572.

Ayres, A., & Theilen, F. 1999. Relationship between P- and S-wave velocities and geological properties of near-surface sediments of the continental slope of the Barents Sea. *Geophysical Prospecting*, **31**, 431–441.

Bagaini, C., & Muyzert, E. 2004. Calibration of cross-line components for sea-bed 4C acquisition systems. *Geophysical Prospecting*, **52**, 341–349.

Brekhovskikh, L. M. 1960. *Waves in layered media*. New York, Academic Press.

Caiti, A., Stoll, R., & Akal, T. 1994. Estimation of shear wave velocity in shallow marine sediments. *IEEE Journal of Oceanic Engineering*, **19**, 58–73.

Chapman, C. 2004. *Fundamentals of seismic wave propagation.* Cambridge University Press.

Chmela, B. 2003. Innovative non-conventional techniques for focused reservoir imaging. *First Break*, **21**, 44–46.

Daley, P. F., & Hron, F. 1983a. High frequency approximation to the nongeometrical S* arrival. *Bulletin of the Seismological Society of America*, **73**, 109–123.

Daley, P. F., & Hron, F. 1983b. Nongeometric arrivals due to highly concentrated sources adjacent to plane interfaces. *Bulletin of the Seismological Society of America*, **73**, 1655–1671.

Daley, P. F., & Hron, F. 1988. A non-geometrical SH-arrival. *Geophysical Prospecting*, **36**, 430–445.

Dankbaar, J. W. M. 1985. Separation of p- and s-waves. *Geophysical Prospecting*, **33**, 970–986.

de Hoop, A. T. 1960. A modification of Caginard's method for solving seismic pulse problems. *Applied Scientific Research*, **B 8**, 349–356.

de Hoop, A. T., & van der Hijden, J. H. M. T. 1983. Generation of acoustic waves by impulsive line source in a fluid/solid configuration with a plane boundary. *Journal of the Acoustic Society of America*, **74**, 333–342.

de Hoop, A. T., & van der Hijden, J. H. M. T. 1984. Generation of acoustic waves by impulsive point source in a fluid/solid configuration with a plane boundary. *Journal of the Acoustic Society of America*, **75**, 1709–1715.

Deans, D. R. 1983. *The Radon transform and some of its Applications*. John Wiley and Sons New York.

Domenico, S. N. 1984. Rock lithology and porosity determination from shear and compressional wave velocity. *Geophysics*, **49**, 1188–1195.

Donati, M. S., & Stewart, R.R. 1996. P- and S-wave separation at a liquid-solid interface. *Journal of Seismic Exploration*, **5**, 113–127.

Dong, H., Allouche, N., Drijkoningen, G. G., & Versteeg, W. 2010. Estimation of shear-wave velocity in shallow marine environment. *In: Proceedings of the 10th European Conference on Underwater Acoustics (ECUA)*.

Drijkoningen, G. G., & Chapman, C. H. 1988. Tunneling rays using the Cagniard-de Hoop method. *Bulletin of the Seismological Society of America*, **78**, 898–907.

Duijndam, A. J. W., Schonewille, M. A., & Hindriks, C. O. H. 1999. Reconstruction of band-limited signals, irregularly sampled along one spatial direction. *Geophysics*, **64**, 524–538.

Eggenberger, K., Muijs, R., Robertsson, J., van Manen, D.J., & Holliger, K. 2010. Estimation of inelastic seismic material properties of a surficial sea-bed from multi-component marine seismic data. *Near Surface Geophysics*, **8**, 459–465.

Engelmark, F. 2001. Using 4-C to characterize lithologies and fluids in clastic reservoirs. *The Leading Edge*, **20**(9), 1053–1055.

Ewing, J., Carter, J. A., Sutton, G. H., & Barstow, N. 1992. Shallow water sediment properties derived from high-frequency shear and interface waves. *Journal of Geophysical Research*, **97**, 4739–4762.

Fokkema, J. T., & van den Berg, P. M. 1993. *Seismic applications of acoustic reciprocity*. Elsevier Science Pub. Co., Inc.

Fuchs, K., & Müller, G. 1971. Computation of synthetic seismograms with the reflectivity method and comparison with observations. *Geophysical Journal of the Royal Astronomical Society*, **23**, 417–433.

Gaiser, J. E. 2007. Detector coupling corrections for vector infidelity of multicomponent obc data. *Geophysics*, **72**(3), V67–V77.

Gaiser, J.E., & Vasconcelos, I. 2009. Elastic interferometry for ocean bottom cable data: Theory and examples. *Geophysical Prospecting*, **58**, 347–360.

Gehrmann, T., Gimpel, P., & Theilen, F. 1984. Marine shear wave profiling. *Pages 592–594 of: 54th Annual International Meeting, SEG, Expanded Abstracts*.

Ghose, R., & Goudswaard, J. 2004. Integrating S-wave seismic-reflection data and cone-penetration-test data using a multiangle multiscale approach. *Geophysics*, **69**, 440–459.

Ghose, R., Brouwer, J., & Nijhof, V. 1996. A portable S-wave vibrator for high-resolution imaging of the shallow subsurface. *Page M037 of: 58th Annual International Meeting, European Association of Geosciences and Engineers Abstracts*.

Granli, J. R., Arnsten, B., Sollid, A., & Hilde, E. 1999. Imaging through gas-filled sediments using marine shear-wave data. *Geophysics*, **64**, 668–677.

Grechka, V., & Tsvankin, I. 2002. PP + PS = SS. *Geophysics*, **67**(6), 1961–1971.

Gregory, A. R. 1976. Fluid saturation effects on dynamic elastic properties of sedimentary rocks. *Geophysics*, **41**, 895–921.

Gutowski, P. R., Hron, F., Wagner, D. E., & Treitel, S. 1984. S*. *Bulletin of the Seismological Society of America*, **74**, 61–78.

Hale, Dave. 2009. A method for estimating apparent displacement vectors from time-lapse seismic images. *Geophysics*, **74**(5), V99–V107.

Hamilton, E. L. 1976. Shear-wave velocity versus depth in marine sediments - A review. *Geophysics*, **41**, 985–996.

Hamilton, E. L. 1979. V_p/V_s and Poisson's ratios in marine sediments and rocks. *Journal of the Acoustical Society of America*, **66**, 1093–1101.

Hamilton, E. L., & Bachman, R.T. 1982. Sound velocity and related properties of marine sediments. *Journal of the Acoustical Society of America*, **72**, 1891–1904.

He, Tao, Spence, George D., Wood, Warren T., Riedel, Michael, & Hyndman, Roy D. 2009. Imaging a hydrate-related cold vent offshore Vancouver Island from deep-towed multichannel seismic data. *Geophysics*, **74**(2), B23–B36.

Hong, T. L., & Helmberger, D. V. 1977. Generalized ray theory for dipping structure. *Bulletin of the Seismological Society of America*, **67**, 995–1008.

Hron, F., & Mikhailenko, B. G. 1980. Discovery of a new nongeometrical S* arrival generated at a free interface. *Pages 293–297 of: Proceedings of the 17th assembly of the ESC.*

Hron, F., & Mikhailenko, B. G. 1981. Numerical modeling of nongeometrical effects by the Alekseev-Mikhailenko method. *Bulletin of the Seismological Society of America*, **71**, 1011–1029.

Imai, T., & Tonouchi, K. 1982. Correlation of N-value with S-wave velocity. *Pages 67–72 of: Proceedings of the 2nd European Symposium on Penetration Testing.*

Jin, S., Cambois, G., & Vuillermoz, C. 2000. Shear-wave velocity and density estimation from ps-wave AVO analysis: Application to an OBS dataset from the North Sea. *Geophysics*, **65**(5), 1446–1454.

Kabir, M. M. N., & Verschuur, D. J. 1995. Restoration of missing offsets by parabolic Radon transform. *Geophysical Prospecting*, **43**, 347–368.

Kennett, B. L. N. 1980. Seismic waves in a stratified half space-II. Theoretical seismograms. *Geophysical Journal of the Royal Astronomical Society*, **61**, 1–10.

Kruiver, P., Deák, A., & Allouche, N. 2010. Extraction of geotechnical properties from Scholte waves in underwater environments. *In: EAGE extended abstract.*

Kugler, S., Bohlen, T., Forbriger, T., Bussat, S., & Klein, G. 2007. Scholte-wave tomography for shallow-water marine sediments. *Geophysical Journal International*, **168**, 551–570.

Lucas, A. L. 1974. A high resolution marine seismic survey. *Geophysical Prospecting*, **21**, 667–682.

Marsset, B., Missiaen, T., Roeck, Y. H. De, Noble, M., Versteeg, W., & Henriet, J. P. 1998. Very high resolution 3D marine seismic data processing for geotechnical applications. *Geophysical Prospecting*, **46**, 105–120.

Mjelde, R., Raum, T., Digranes, P., Shimamura, H., Shiobara, H., & Kodaira, S. 2003. Vp/Vs ratio along the Vøring Margin, NE Atlantic, derived from OBS data: implications on lithology and stress field. *Tectonophysics*, **369**, 175–197.

Muijs, R., Robertsson, J. O. A., & Holliger, K. 2004. Data-driven adaptive decomposition of multicomponent seabed recordings. *Geophysics*, **69**(5), 1329–1337.

Muijs, R., Robertsson, J. O. A., & Holliger, K. 2007. Data-driven adaptive decomposition of multicomponent seabed seismic recordings: Application to shallow-water data from the north sea. *Geophysics*, **72**(6), V133–V142.

Müller, C., Milkereit, B., Bohlen, T., & Theilen, F. 2002. Towards high-resolution 3D marine seismic surveying using Boomer sources. *Geophysical Prospecting*, **50**, 517–526.

Park, C. B., Miller, R. D., Xia, J., Ivanov, J., Sonnichsen, G. V., Hunter, J. A., Good, R. L., Burns, R. A., & Christian, H. 2005. Underwater MASW to evaluate stiffness of water-bottom sediments. *The Leading Edge*, **24**, 724–728.

Pieuchot, M. 1984. *Seismic instrumentation (handbook of geophysical exploration)*. Geophysical Press, Amsterdam.

Pinson, L. J. W., Henstock, T. J., Dix, J. K., & Bull, J. M. 2008. Estimating quality factor and mean grain size of sediments from high-resolution marine seismic data. *Geophysics*, **73**, G19–G28.

Pulliam, J., Austin, J. A., Luhurbudi, E. C., Saustrup, S., & Stoffa, P. L. 1996. An ultrahigh resolution 3-D survey of the shallow subsurface on the continental shelf of New Jersey. *The Leading Edge*, **15**, 839–845.

Riedel, M., & Theilen, F. 2001. AVO investigations of shallow marine sediments. *Geophysical Prospecting*, **49**, 198–212.

Ritzwoller, M. H., & Levshin, A. L. 2002. Estimating shallow shear wave velocities with marine multi-component seismic data. *Geophysics*, **67**, 1991–2004.

Roth, M., & Holliger, K. 2000. The non-geometric PS wave in high-resolution seismic data: observations and modelling studies. *Geophysical journal international*, **140**, F5–F11.

Schalkwijk, K. M. 2001. *Decomposition of multicomponent ocean-bottom data into P- and S-waves*. Delft University of Technology (Ph.D. thesis).

Schalkwijk, K. M., Wapenaar, C. P. A., & Verschuur, D. J. 2003. Adaptive decomposition of multicomponent ocean-bottom seismic data into downgoing and upgoing P- and S-waves. *Geophysics*, **68**, 1091–1102.

Schmidt, H. 1988. *SAFARI User's Guide*. SACLANT Undersea Research Centre, La Spezia, Italy.

Schmidt, H., & Tango, G. 1986. Efficient global matrix approach to the computation of synthetic seismograms. *Geophysical Journal of the Royal Astronomical Society*, **84**, 57–67.

Schuster, G. T., & Zhou, M. 2006. A theoretical overview of model-based and correlation-based redatuming methods. *Geophysics*, **71**, SI103–SI110.

Sheriff, R. E., & Geldart, L.P. 1995. *Exploration seismology, 2nd ed.* Cambridge University Press.

Shillington, D. J., Minshull, T. A., Peirce, C., & O'Sullivan, J. M. 2008. P- and s-wave velocities of consolidated sediments from a seafloor seismic survey in the north celtic sea basin, offshore ireland. *Geophysical Prospecting*, **56**(2), 197–211.

Simons, D.G., & Snellen, M. 2009. A bayesian approach to seafloor classification using multi-beam echo-sounder backscatter data. *Applied acoustics*, **70**(10), 1258–1268.

Simons, D.G., Snellen, M., & Ainslie, M.A. 2007. A multivariate correlation analysis of high- frequency bottom backscattering strength measurements with geotechnical parameters. *IEEE Journal of Oceanic Engineering*, **32**(2), 640 – 650.

Stewart, R. R., Gaiser, J. E., Brown, R. J., & Lawton, D. C. 2003. Converted-wave seismic exploration: Applications. *Geophysics*, **68**, 40–57.

Taner, M. Turhan, Koehler, F., & Alhilali, K. A. 1974. Estimation and correction of near-surface time anomalies. *Geophysics*, **39**(4), 441–463.

Taylor, G. G. 1989. The point of P-S mode converted reflection: An exact determination. *Geophysics*, **54**, 1060–1063.

Theilen, F. R., & Pecher, I. A. 1991. Assessment of shear strength of the sea bottom from shear wave velocity measurements on box cores and in-situ. *Pages 67–74 of: Shear waves in marine sediments, Kluwer Academic Publishers.*

Tygel, M., & Hubral, P. 1987. *Transient waves in layered media.* Elsevier Science Publ. Co.

van Dalen, K. N. 2011. *Multi-component characterization of porous media.* Delft University of Technology (Ph.D. thesis).

Wapenaar, C.P.A., & Berkhout, A.J. 1989. *Elastic wave field extrapolation: Redatuming of single- and multi-component seismic data.* Elsevier Science Publ. Co.

Wapenaar, C.P.A., Herrmann, P., Verschuur, D.J., & Berkhout, A.J. 1990. Decomposition of multicomponent seismic data into primary P- and S-wave responses. *Geophysical Prospecting*, **38**, 633–662.

Westerdahl, H., Sparrevik, P., Madshus, C., Amundsen, L., & Fjellanger, J. P. 2004. Development and testing of a prototype seabed coupled shear wave vibrator. *Pages 929–932 of: 74th annual international meeting, SEG, expanded abstracts.*

White, J.E. 1965. *Seismic waves radiation, transmission and attenuation.* McGraw-Hill, Inc., New York.

Woodhouse, J.H. 1974. Surface waves in laterally varying layered structure. *Geophysical Journal of the Royal Astronomical Society*, **37**, 461–490.

Zoeppritz, K. 1919. *Über reflexion und durchgang seismischer Wellen durch Unstetigkersflächen.* Nachrichten von der Königlichen Gesellschaft der Wissenschaften zu Göttingen, Mathematisch-physikalische Klasse.

Samenvatting

Geconverteerde golven in ondiepe mariene milieus: modellering en veldexperimenten

Steeds meer menselijke activiteiten vinden plaats op de bodem van ondiepe zee, zoals het bouwen van platformen en windmolenparken, het leggen van pijpleidingen en het baggeren van zand. Om de risico's die deze activiteiten met zich meebrengen te verminderen is een goede kennis van de bodemeigenschappen essentieel. De ondergrond in ondiepe mariene milieus kan veel energiebronnen bevatten, zoals gashydraten en olie- en gasvelden, die zich vaak op een diepte van enkele honderden tot duizenden meters bevinden. Een betrouwbare schatting van de eigenschappen van de ondiepe ondergrond kan het seismische beeld op grote dieptes aanzienlijk verbeteren. Seismische drukgolven (P-golven) die zijn geconverteerd naar schuifgolven (S-golven) kunnen worden ingezet om deze eigenschappen te bepalen. De acquisitie en dataverwerking van geconverteerde golven in ondiepe mariene milieus is uitdagend. Dit komt vooral door de grote verhouding van voortplantingssnelheid van de P- en S-golf in de sedimenten. In dit proefschrift wordt de acquisitie en dataverwerking van geconverteerde golven behandeld aan de hand van veldexperimenten en synthetische modellen.

Vele modi van conversies bestaan. Echter, niet al deze zijn detecteerbaar and daarom geschikt voor de karakterisatie van de ondergrond. Vooral voor ondiepe niet-geconsolideerde sedimenten is de PS-conversie op de waterbodem alleen van belang wanneer dit in het nabije golfveld gebeurt. Dit is het geval wanneer de seismische bron wordt geplaatst op een afstand van de waterbodem die kleiner is dan een golflengte. Indien de S-golf snelheid in de ondergrond lager is dan de geluidssnelheid van het water wordt een S-golf gegenereerd die qua aankomsttijd afkomstig lijkt te zijn uit het projectiepunt van de bron op de waterbodem. Deze bijzondere geconverteerde golf, aangeduid als de niet-geometrische PS-golf, ontstaat alleen voor een beperkt bereik in horizontale slowness (reciproke snelheid), die afhankelijk is van de verhouding tussen de S-golf snelheid en de geluidssnelheid van het water. Alleen als deze verhouding kleiner is dan 1 ontstaat deze golf. Hoe kleiner de verhouding, des te groter is het bereik in horizontale slowness waarbinnen deze golven kunnen worden waargenomen. De niet-geometrische PS-golven kunnen daardoor in het Radon domein worden geïdentificeerd en gescheiden van andere aankomsten. Het resultaat kan worden geïnterpreteerd en verwerkt alsof pure S-golven op een efficiënte manier zijn gegenereerd, zonder gebruik te maken van een seismische bron op de waterbodem.

Deze niet-geometrische PS-golven zijn voor het eerst waargenomen met behulp van multi-component ontvangers tijdens een veldexperiment in een kanaal in Gent. Hun aanwezigheid is gevalideerd door middel van modelleringsstudies. In dit veldexperiment zijn verschillende soorten seismische bronnen gebruikt, waaronder een "air gun", een "water gun" en een sparker. Echter zijn de niet-geometrische geconverteerde golven alleen waargenomen in de air-gun data. Door de resultaten van de modellering te vergelijken met de veldmeting is gebleken dat ook geometrische

S-golven, die zowel op de waterbodem als op de reflector zijn geconverteerd, te zien waren in de data. Geconverteerde PS-golven kunnen worden gescheiden van P-golven met behulp van verschillende dataverwerkingstechnieken. De meeste van deze technieken vereisen een adequate ruimtelijke bemonstering. Door de lage S-golf snelheid hebben PS-golven een korte golflengte waardoor een goede bemonstering niet gemakkelijk te verwezenlijken is, zoals is gebleken uit de data uit Gent.

In het Donau veldexperiment is een nieuwe methode toegepast om aan de eisen van ruimtelijke bemonstering te voldoen. De methode houdt in dat meerdere seismische lijnen worden geschoten, die met behulp van een nieuwe dataverwerkingsstap worden samengevoegd. Deze dataverwerkingsstap is essentieel omdat de positioneringsfouten tijdens een meting aanzienlijk groot kunnen zijn. Een bepaalde schotlijn wordt als referentielijn gebruikt. De relatieve variaties in bron- en ontvangerposities van de andere schoten worden vervolgens met kruiscorrelatie geschat en gecorrigeerd t.o.v. van de referentielijn. Het eindresultaat bestaat uit vier fijn bemonsterde zogenaamde "common-receiver gathers", corresponderend met de deeltjessnelheid in drie orthogonale richtingen en de druk.

Elastische golfveld decompositie is vervolgens toegepast op deze data om de P- en de S-golven van elkaar te scheiden. Een goede schatting van de elastische parameters van de bovenste aardlaag en een goede koppeling van de gebruikte sensoren zijn essentieel voor deze dataverwerkingsmethode. De koppelingsfilters worden geschat uit de data. Doordat het ondiepe water in het onderzoeksgebied een aanzienlijk effect heeft op het gemeten golfveld is het noodzakelijk om de data te splitsen in hoge en lage frequenties. Terwijl de hoge frequenties van het golfveld bestaan uit P-golf reflecties en geometrische PS-conversies, worden de lage frequenties gedomineerd door niet-geometrische PS-golven en PS-refracties. Twee verschillende methoden worden toegepast om te corrigeren voor de onvolkomenheden van de sensorkoppeling. De common receiver gathers met gescheiden S-golfvelden laten uiteindelijk een kleine verbetering van de zichtbaarheid van de geconverteerde golven zien. De laagfrequente niet-geometrische PS-golven kunnen verwerkt worden als pure-S-golven om een beeld van het zeer ondiepe deel van de ondergrond te verkrijgen. Uit de hoogfrequente data, bestaande uit golven die geconverteerd zijn op de reflectie punten, kan een aanvullend PS-golf beeld vervaardigd worden van diepere lagen van de ondergrond.

Summary

Converted waves in shallow marine environments: modelling and field experiments

The shallow marine subsurface is explored for various engineering purposes e.g. constructing installations and platforms, laying pipelines and dredging for sand. Knowledge of the soil properties is essential to minimize the risks involved with these offshore activities. Energy resources in the form of gas hydrates and hydrocarbon reservoirs are often found a few hundred meters to a few kilometers below the seafloor. Accurate estimates of the sediments properties at shallow depths may considerably improve the image at the target depth. Seismic waves converted from compressional (P-) to shear (S-) mode can be useful to retrieve these properties. The acquisition and processing of converted-wave data in shallow marine environments remains challenging. This is due to the high velocity ratio between the P- and the S-wave in the sediments. In this thesis, the acquisition and processing of converted waves is addressed through field experiments and synthetic modelling.

Many modes of conversions exists, however, not all of them are detectable and therefore suitable for the characterization of the subsurface. Particularly for shallow unconsolidated sediments, the PS-conversion at the water bottom is considerable only when it occurs in the near-field. This is the case when the seismic source is placed at a height less than a wavelength from the water-sediment interface. An S-wave that travels kinematically as if it originates from the projection point of the source on the interface is excited when the wave speed in the solid is less than the sound speed in the water. This particular mode of conversion, referred to as the non-geometric PS-wave, has a specific region of existence in terms of horizontal slownesses, depending on the ratio of the S-wave velocity and the sound speed in the water. Only for ratios smaller than 1, this wave appears. Lower ratios result in wider region of appearance. Due to this property, the non-geometric P-S wave can be identified and filtered from other events in the Radon domain. The result can be treated as pure S-waves that can efficiently be recorded without actually having to place the source on the interface.

The non-geometric PS-waves were observed in a multicomponent data set acquired in a shallow-water canal in Ghent and their presence was validated through modelling studies. In this field experiment, different types of seismic sources were used including an air gun, a water gun and a sparker. However, the non-geometric converted modes were only observable in the air-gun data. Comparing field data to modelling results showed the presence of other modes converted geometrically at the water bottom and at reflectors in the subsurface. The PS-modes can be separated from pure P-waves using processing techniques. However, most of these techniques require an adequate spatial sampling. Due to the low velocity of PS-waves and consequently their short wavelength, a dense spatial sampling can not be easily achieved as it was for the Ghent data.

In the field experiment conducted in the Danube River, a new methodology was adopted to fulfill the spatial sampling requirement. This is done by shooting

one track multiple times and merging the shot lines in an effective manner in a separate processing step. This processing step is essential because positioning errors introduced during the field measurement can become significant in the combined line. For this processing step, a particular shot line is used as a reference line and relative variations in source and receiver positions in the other shot lines are corrected for using crosscorrelation. The result consists of four densely-sampled receiver gathers, corresponding to the three components of the particle velocity and the pressure.

Elastic wave decomposition, aiming at separating the converted modes from the P-waves, is subsequently applied to these receivers gathers. The decomposition relies on accurate knowledge of the water-bottom elastic parameters and on a perfect calibration of the sensors. The medium parameters are estimated from the inversion of the Scholte waves dispersion curves and the coupling filters are determined from the data. The shallow depth of the water, encountered in the survey area, necessitated the separation of the data in high-frequency regime, consisting of P-wave reflections and PS-converted modes, and a low frequency regime including the non-geometric PS-waves and PS-refracted modes. Two different approaches dependent on the frequency range are adopted to correct for imperfections in the geophone coupling. The decomposed result shows an improvement in the visibility of the converted modes. The low frequency part, representing waves converted at the water bottom, can be treated as pure S-waves and used to obtain an S-wave image of the very shallow part of the sediments. The processing of high-frequency data, consisting mainly of waves converted at the reflectors, can provide a PS-wave image of the deeper part of the subsurface.

Acknowledgements

The last words of this thesis are dedicated to the people who have contributed to its completion.

First, I would like to thank my supervisor Guy Drijkoningen for his guidance and support throughout the PhD-project. He gave me the opportunity to pursue my own research path without forgetting to share his own experience with me. Many thanks to my promotors Kees Wapenaar and Dick Simons for their efforts in correcting and improving the thesis. Also, I would like to acknowledge the committee members for their questions and comments. I learned a lot from Jan Thorbecke over the last years. His help was absolutely indispensable and his immense modesty is admirable. Many thanks to Wim Mulder for allowing me to use his codes and helping me with the numerical modelling at the beginning of the project. Guus Lohlefink made sure that I stayed connected to Marken and Ranajit Ghose and Evert Slob have been very generous in answering my questions about geophysics and life. Many Thanks to them.

A great deal of my PhD work relies on two field data sets. Therefore, I owe a lot of gratitude to all the people who were involved in these field experiments. For the Ghent data, I would like to thank Wim Versteeg, Aletta Filippidou and everyone who was there to assist them. The Danube field data is the result of a fruitful cooperation between Delft University of Technology (TUD), Eötvös Loránd University (ELTE), Ghent University, the Royal Netherlands Institute for Sea Research (NIOZ) and Deltares. Particularly, I am thankful to Alber Hemstede for turning the stressful and demanding fieldworks into an enjoyable experience. In his presence, I never had to worry about a missing cable, a crashing computer or the Hungarian police checking our boat. The help provided by Gábor Bada and Prof. Horváth (ELTE) was very much appreciated. A special thanks to the crew from the NIOZ, including Lorendz Boom, Bob Koster, Leon Wuis and Jack Schilling, who succeeded to fit their huge equipment in our small pontoon in the Danube River. Many thanks to Hami Zoltán and Tamás Tóth (Geomega) and Mike van de Werf (Deltares). Much of the physical work during the fieldwork and the processing afterwards was done by the students Koen Duijnmayer (TUD), Atilla Deák and Istvan Kuda (ELTE). Thank you for all your hard work.

I have so many good memories from the coffee and apple breaks, the DOGS drinks and trips, and the conferences thanks to my friends and colleagues at the department: Adriaan, Aletta, Ali, Alimzhan, Andrea, Araz, Bobby, Bouko, Carlos, Claudio, Christiaan, Danijela, Daria, Dennis, Deyan, Dessislava, Duddy, Dylan, Elmer, Ilja, Jan, Joost, Jürg, Geertje, Gerrit, Gerwin, Guus, Karel, Maria, Marit, Martijn, Marwan, Mattia, Menne, Mohsen, Niels, Nizare, Tristan, Ralph, Panos, Pantelis, Patrick, Petar, Rik, Thomas, Wiebke, Wieske, Wouter and Xiaoxi. Particularly, I would like to thank Joost for his inspiring ideas and thoughts and for the enjoyable walks through the hidden green paths in the surroundings. Jürg has been a great friend to me and helped me solve numerous problems with Matlab and Latex. My heartfelt gratitude is expressed to Wieske for her involvement and sociability. I also thank Deyan for sharing with me his passions in science fiction,

chocolate and movies. Karel's ability to explain the most dreadful looking equations in the least amount of words, is impressive. Thank you for all your help. At last but surely not least I would like to thank my close neighbor Elmer for his patience all these years.

My family has been of great support to me over the years. I dedicate this work to my parents who worked very hard to build a new life in The Netherlands and paved the way for me, my brothers and sister. I am grateful to the support of Bouchra, Atef, Wael, Mohamed and Hajer and my dear friends Alma, Maartje and Hella. Enfin, je remercie toute ma famille en Tunisie et en France pour son soutien et ses encouragements.

Curriculum Vitae

2011:	Postdoctoral researcher, Department of Air transport and Operations, Delft Univeristy of Technology, The Netherlands.
2010:	Research intern, Schlumberger Cambridge research center, Cambridge, UK.
2006 - 2011:	PhD in Applied Geophysics and Petrophysics, Department of Geotechnology, Delft University of Technology, The Netherlands.
2003 - 2006:	MSc in Geophysics, Utrecht University, The Netherlands.
2000 - 2003:	BSc in Earth Sciences, Utrecht University, The Netherlands.

Journal papers and conference proceedings

- Allouche N., G.G. Drijkoningen, W. Versteeg and R. Ghose, 2011, Converted waves in shallow marine environment: experimental and modeling studies: Geophysics.

- Allouche N. and G.G. Drijkoningen, 2010, Methodology for dense spatial sampling of multicomponent recording of converted waves in shallow marine environments: Geophysics.

- van der Neut J. , N. Allouche and C. P.W. Wapenaar, 2010, Elastic decomposition with downhole geophones and hydrophones: 80th Annual International Meeting, SEG, Expanded Abstracts.

- Allouche N. and G.G. Drijkoningen, 2010, Characteristics and potential use of non-geometric PS-waves in shallow marine environments: Annual International meeting, EAGE, extended abstract.

- Allouche N. and G.G. Drijkoningen, 2009, Characteristics of the non-geometric PS-converted wave in a fluid-solid configuration: Frontiers in shallow subsurface technology.
- Dong H., N. Allouche, G.G. Drijkoningen and W. Versteeg, 2010, Estimation of shear-wave velocity in shallow marine environment: Proceedings of the 10th European Conference on Underwater Acoustics (ECUA).
- Kruiver P. P., A. Deák, and N. Allouche, 2009, Extraction of shear wave velocities from Scholte waves in underwater environments: Frontiers in shallow subsurface technology.
- Allouche N., G.G. Drijkoningen and J. van der Neut, 2009, Positioning-error correction for densely sampled high-resolution seismic data recorded with water-bottom cable: 79th Annual International Meeting, SEG, Expanded Abstracts.
- Allouche N., G.G. Drijkoningen, R. Ghose, J. Thorbecke and W. Versteeg, 2008, Acquiring shear-wave information in shallow water environment from field data near Ghent, Belgium: 78th Annual International Meeting, SEG, Expanded Abstracts.
- Allouche N., G.G. Drijkoningen, W. Versteeg and D.G. Simons, 2008, Studying converted waves at shallow marine environment: Proceedings of the 9th European Conference on Underwater Acoustics (ECUA).